115

FRACTURE AND FATIGUE ANALYSIS OF AN AGITATOR SHAFT WITH A CIRCUMFERENTIAL NOTCH

119023

A Thesis Submitted to the
Graduate School of Natural and Applied Sciences of
Dokuz Eylül University
In Partial Fulfillment of the Requirements for
The Degree of Master of Science in Mechanical Engineering,
Machine Theory and Dynamics Program

T.C. YÜKSEKÖĞRETİM KURULU
DOKÜMANTASYON MERKEZİ

by
Celalettin KARAAĞAÇ

July, 2002
İZMİR

Ms. Sc. THESIS EXAMINATION RESULT FORM

We certify that we have read this thesis, entitled **"FRACTURE AND FATIGUE ANALYSIS OF AN AGITATOR SHAFT WITH A CIRCUMFERENTIAL NOTCH"** completed by **CELALETTİN KARAAĞAÇ** under supervision of **Asst. Prof. M. EVREN TOYGAR** and that in our opinion it is fully adequate, in scope and in quality, as a thesis for the degree of Master of Science.

M. Evren Toygar

Asst. Prof. M. Evren TOYGAR

Supervisor

Prof. Dr. Onur SAYMAN

Committee Member

Prof. Dr. Tevfik AKSOY

Committee Member

Approved by the

Graduate School of Natural and Applied Sciences

Prof. Dr. Cahit HELVACI

Director

ACKNOWLEDGEMENTS

I would like to thank my advisor Asst. Prof. M. Evren TOYGAR who contributed greatly to the setting up the extent and success of this study, for her support in providing necessary literature and valuable suggestions and guidance, which leaded me to study hard, and investigation effectively.

I am also grateful to all my colleagues for their significant contributions in arranging the devices to obtain power and vibration graphs.

Finally, my special thanks go to my wife for her vast support for encouraging me, and great patience along the study.

Celalettin KARAAĞAÇ

İzmir, 2002

ABSTRACT

In this study, the failure (fracture) of an agitator shaft with a circumferential notch was selected as investigation topic. However, this study is intended for introducing fracture mechanics from an application viewpoint. It essentially focuses on both stress and fatigue analyses.

Many mechanical systems subject to loading require modeling before their analyses can be executed. The important thing at this point is to be able to create an appropriate model; in addition consistent assumptions should be made. In this connection, several computer programs introduced provide much benefit to model the systems. In this study, Ansys 5.4 FEM program, to analyze the stresses at the notch tip, and TKSolver program, to perform calculations and to plot S-N diagrams for fatigue analysis were used.

In general, the study gives an engineering perspective on how a real event can be analyzed by evaluating findings and data taken from the equipment. Before stress analysis, brief information on the agitator is given. In addition, the shaft material is introduced and how an *fcc* (face-centered cubic) crystal fracture is explained.

With the macroscopic examination of the fracture surface, the signs left by crack propagation are dealt in detail to interpret how the shaft is leaded to fracture. In the proceeding chapters, by setting up an agitator model, data taken from the agitator during operation and specification sheets are processed to make more realistic approximations for bending and tork forces, since they will be base for stress analysis, in which K_I is evaluated. For stress analysis, ten crack models with various crack lengths are created by using Ansys 5.4 FEM program. Again, mathematical procedure to show how to do fatigue analysis and related S-N diagrams drawn by using TKSolver program are presented.

ÖZET

Bu çalışmada, çevresel çentikli bir karıştırıcı şaftının kırılması araştırma konusu olarak seçilmiştir. Ancak, kırılma mekaniği daha çok uygulama açısından göz önüne alınmış olup gerilme ve yorulma analizi üzerine yoğunlaşılmıştır.

Bir çok mekanik sistemi analizden önce modellemek gerekir. Tutarlı kabullerle uygun bir model oluşturmak önemlidir. Bu bağlamda, mevcut pek çok bilgisayar programı modellemede çok büyük kolaylıklar sağlar. Bu çalışmada, çatlak ucu gerilme analizi için Ansys 5.4, yorulma analizi hesaplarının yapılması ve S-N diyagramlarının çizimi için TKSolver programı kullanılmıştır.

Genel olarak çalışma, bulguların ve ekipmandan alınan verilerin değerlendirerek gerçek bir olayın nasıl analiz edilebileceğini ortaya koyar. Gerilme analizi öncesi, karıştırıcı hakkında verilen bilgiye ek olarak, şaft malzemesi tanıtılmış ve *ymk* (yüzey-merkezli kübik) kristalin nasıl kırılabileceği açıklanmıştır.

Şaftın kırılma yüzeyinin detaylı makroskopik incelenmesiyle, çatlak ilerlemesinin bıraktığı izlerden kırılmanın nasıl olduğu yorumlanır. İleriki bölümlerde, çalışma esnasında ekipmandan ve spesifikasyonlardan alınan bilgiler, K_I'in değerlendirileceği gerilme analizine temel olacak eğilme ve tork kuvvetlerinin gerçekçi bir şekilde bulunmasında kullanılır. Gerilme analizi için, Ansys 5.4 sonlu eleman programı ile değişik çatlak boylarında on adet çatlak modeli oluşturulmuştur. Yine, TKSolver programı kullanılarak, yorulma analizine ilişkin hesap yöntemi ve S-N diyagramlarının çizimlerinin nasıl yapılacağı verilmektedir.

T.C. YÜKSEKÖĞRETİM KURULU
DOKÜMANTASYON MERKEZİ

CONTENTS

Chapter Three

STRESS ANALYSIS

Chapter Four

FATIGUE ANALYSIS

T.C. YÜKSEKÖĞRETİM KURULU
DOKÜMANTASYON MERKEZİ

Chapter Five
CONCLUSIONS

REFERENCES

APPENDICES

LIST OF TABLES

LIST OF FIGURES

T.C. YÜKSEKÖĞRETİM KURULU
DOKÜMANTASYON MERKEZİ

NOMENCLATURE

Abbreviation	Term
a	Notch or crack length
A	1) Area, 2) ampere
d	Diameter from tip to tip of notch (crack)
D	Shaft diameter
E	Modulus of elasticity
F_i, F_x, F_z	Force
G	Shear modulus
I_x, I_z	Inertia moments
K_I	Stress intensity factor for mode-I
K_{III}	Stress intensity factor for mode-III
K_C	Fracture toughness (plane stress)
K_{IC}	Fracture toughness (plane strain)
ΔK_{th}	Fatigue threshold
L	Length
M	Bending moment
n	Speed (rpm or rps)
N	Cycle
P	Power
r	Radius
R	1) Reaction force, 2) stress ratio
S	Stress
T	Tork
V	1) Shear force, 2) volt
δ_x, δ_z	Deflection (displacement)
σ	Bending stress

T.C. YÜKSEKÖĞRETİM KURULU
DOKÜMANTASYON MERKEZİ

τ	Shear stress
x, y, z	Global coordinates
ω	Angular velocity (rad / s)

Note: The notations not included in the table have been defined in the related chapters.

CHAPTER ONE
INTRODUCTION

1.1 Introduction

Along the years, many unexpected failures of equipments and various machines have occurred throughout the industrial world. A number of these failures have been due to poor design. However, it has been discovered that many failures have been caused by preexisting notches or flaws in materials that initiate cracks that grow and lead to fracture. This discovery has, in a sense, lead to the field of study known as fracture mechanics. The field of fracture mechanics is extremely broad. It includes applications in engineering, studies in applied mechanics (including elasticity and plasticity), and materials science (including fracture processes, fracture criteria, and crack propagation). The successful application of fracture mechanics requires some understanding of the total field.

Thus, as implied above, fracture mechanics is a method of characterizing the fracture behavior of sharply notched members and based on a stress analysis in the vicinity of a notch or crack. Therefore, using fracture mechanics, allowable stress levels and inspection requirements can be quantitatively established to design against the occurrence of fractures in equipments and machinery. In addition, fracture mechanics can be used to analyze the growth of small cracks to critical size by fatigue loading and to evaluate the fitness-for-service, or life extension of existing equipment.

In the petrochemical industry, many types of vessels, which are also called as *drum*, with agitator are being used largely for the purpose of homogeneous mixing of the product being processed at the various steps of the production.

Since a petrochemical plant runs continuously for 24 hours per day, to achieve optimum plant reliability is the main goal of the petrochemical industry. Thus, in case an equipment failure that may occur at an unexpected instant results in production shutdown and its related costs. Such events occur predominantly in rotating equipment, e.g., in large agitators. Therefore, they are responsible for significant loss of plant availability. In fact, an agitator shaft with a notch or scratch can be cracked and leaded to failure easily under the combined stresses created by fluctuating forces during operation.

It is shown that the routine calculations reveal that particular failure, and probably many other similar failures, is not always simple The change in shaft diameters or some uneven sections, which may be made, for example, by a late operator during manufacturing of the shaft may cause stress concentration induced failure. Stress calculations involving stress concentration and fatigue calculations provide a powerful tool with which to arrive at a more complete analysis of failure. The underlying principle is that results of stress, fatigue and fracture calculations should be consistent with the proposed mode of failure.

Similar fracture and fatigue related studies were published (ASTM SPT 918, 1986). In addition, more comprehensive analytic solutions have been presented in the books by Hellan, 1985 and Unger, 2001 for those who want to go deeper into theory.

Furthermore, in recent years, the topics involving fracture and fatigue problems have been investigated and studied by several investigators. For example, the stress intensity factors and stress distribution in solid or hollow cylindrical bars with an axisymmetric internal or edge crack, using the standard transform technique are investigated by Erdol & Erdogan, 1978. The paper concludes that in the cylinder under uniform axial stress containing an internal crack, the stress intensity factor at the inner tip is always greater than that at the outer tip for equal net ligament thickness and in the cylinder with an edge crack which is under a state of thermal stress, the stress intensity factor is a decreasing function of the crack depth, tending to zero as the crack depth approaches the wall thickness. In the study of He & Hutchinson, 2000, the stress intensity factor distributions at the edge of semi-

elliptical surface cracks obtained for cracks aligned perpendicular to the surface of a semi-infinite solid and mixed mode conditions along the crack edge are characterized. Perl & Greenberg, 1998 have investigated the transient mode I stress intensity factors distributions along semi-elliptical crack fronts resulting from thermal shock typical to a firing gun. The solution for a cylindrical pressure vessel of radii ratio $R_o/R_i = 2$ is performed via the finite element (FE) method. In the paper of Vardar & Kalenderoglu, 1989, the effect of notch root radius on fatigue crack initiation and the initiation lives are determined experimentally using notched specimens of varying root radii. Again Vardar, 1982 presents a study in which tests are performed on compact specimens, concluding that crack propagation rates can be correlated successfully using an operational definition of the range ΔJ of the J-integral.

Basically, the study was carried out in three parts: 1) Analysis of the bending force and tork acting on the agitator, 2) Stress analysis of the shaft via Finite Element Method (Ansys 5.4) under given conditions, 3) Fatigue analysis made by using the related stress, k_t and K_I values obtained from the stress analysis. In fact, there is a strong correlation between them. Therefore, it will be very convenient to investigate each of them to arrive at the complete analysis of failure. However, the complete stress analysis involves complex variables and other forms of higher mathematics and may be found in Unger, 2001. Emphasis in this study is on the application and use of fracture mechanics.

T.C. YÜKSEKÖĞRETİM KURULU
DOKÜMANTASYON MERKEZİ

CHAPTER TWO
THE MODELING OF THE PROBLEM AND FORCE ANALYSIS

2.1. Basic Description of the Vessel With Agitator

In general, a typical large vessel with agitator, which consists of 1) Shaft with impeller, 2) Top structure (pedestals) with motor and gearbox, 3) Vessel with fixation to foundation including anchor bolting is shown in Fig. 2.1. The complete drive system is located in the top structure. Normally the shaft is carried and guided by one combined axial/radial (thrust) bearing and one guide bearing. The shaft is driven by a motor/gearbox combination. The top structure must not only be able to carry the corresponding weight of this large drive system but also the *static* and *dynamic* reaction forces and moments resulting from mixing process.

The agitator shaft consists of two parts, upper shaft and lower shaft. The lower shaft is longer than (app. 4 times) the upper shaft. These two parts are tightly connected by means of a rigid coupling to form the complete shaft. Typical view and some dimensions of the shafts are given in the illustrations of both Fig.2.1 and Fig.2.2.

A detailed illustration of the notch model is given in Fig. 2.3. This assumed notch shape and all dimensions given in figure will be taken as basis to model the notch using FEM for stress analysis.

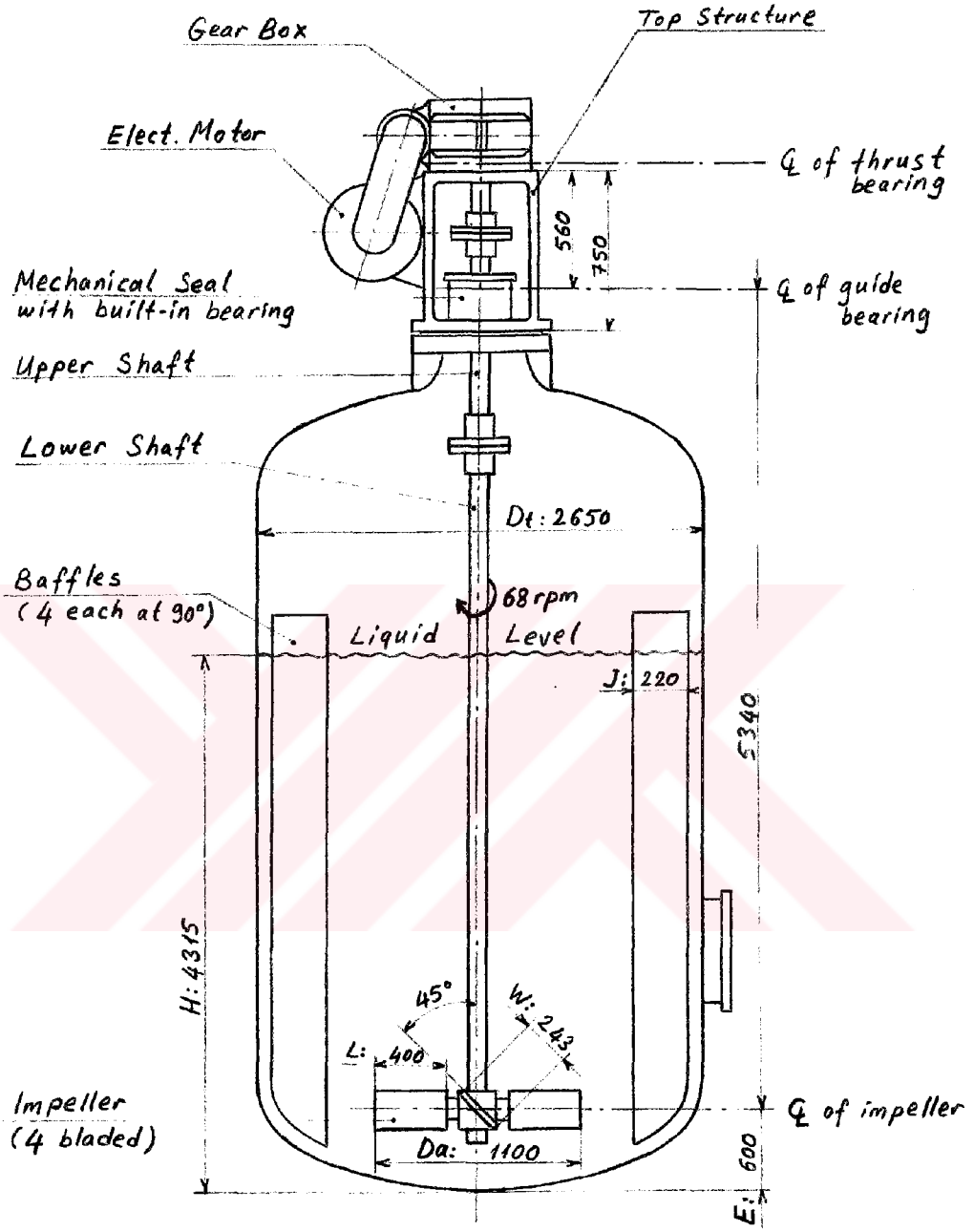

Figure 2.1 General arrangement of the vessel with agitator

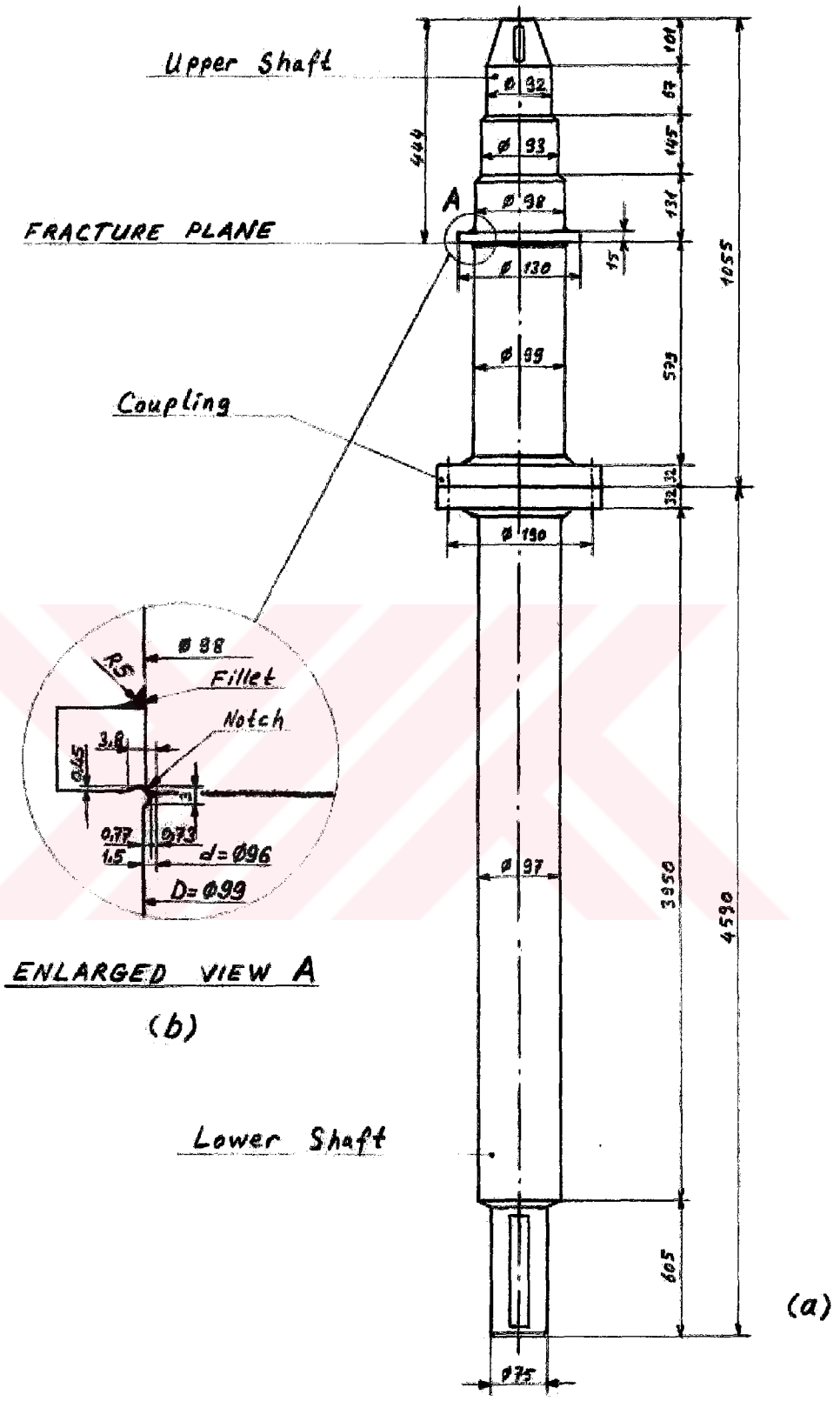

Figure 2.2 The complete agitator shaft.

a) Upper and lower shafts shown in full length, b) Enlarged view of fracture plane on which notch takes place.

T.C. YÜKSEKÖĞRETİM KURULU
DOKÜMANTASYON MERKEZİ

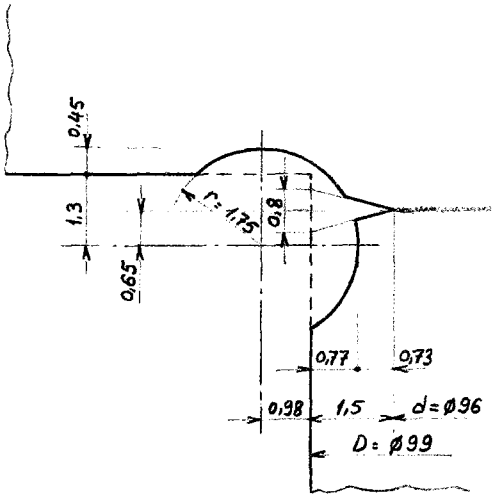

Figure 2.3 Illustration of the notch for modeling

2.1.1 Material of the Agitator Shaft

The agitator shaft was made from a standard AISI type 304 stainless steel that is Austenitic grade. Austenitic stainless steels are the most widely used, and while most are designated in the 300 series. Especially, types 304 and 316 are highly ductile and though grades, and they are utilized for a broad range of equipment and structures. Austenitic grade steels are non-magnetic and non heat-treatable steels that are usually annealed and cold worked. They provide excellent corrosion and heat resistance with good mechanical properties over a wide range of temperatures, respond very well to forming operations, and are readily welded. When fully annealed, they are not magnetic. Austenitic grade steels have γ- austenite structure which can dissolve up to 2 % C in solid solution and has *fcc* (face-centered cubic) crystal lattice.

The Chemical Composition and some Mechanical Properties (acc. to ASTM) of Type 304 SS are given in Table 2.1 and Table 2.2.

Table 2.1 Chemical composition of AISI 304 stainless steel

Element	C	Cr	Ni	Mn	Si	P	S
Weight, %	0.08	18-20	8-10.5	2	1	0.045	0.03

Table 2.2 Mechanical Properties of AISI 304 ss: Annealed

	Unit	
Density (x 1000)	kg /m^3	8
Poison's Ratio	-	0.27 – 0.30
Elastic Modulus	GPa	193 – 200
Shear Modulus	GPa	86
Tensile Strength	MPa	515
Yield Strength	MPa	205
Elongation	%	40
Reduction in Area	%	50
Hardness	Brinell	201

2.1.2 Fracture of Face-Centered Cubic (*fcc*) Metals

Face-centered cubic metals are inherently ductile. The ductility of these metals is related to their essentially low (and relatively temperature insensitive) yield strengths and to the large number of ***slip systems*** for the ***fcc*** crystal structure. Because of their low yield strengths, ***fcc*** metals almost invariably plastically flow at stresses less than those required to fracture them, and this is true at low, as well as at high, temperatures. The availability of slip systems also allows for the relaxation of plastic strain incompatibilities, which often initiate the microcracks. (Courtney, 2000)

Plastic deformation of a single crystal occurs either by ***slip*** or by ***twinning.*** Slip represents a large displacement of one part of the crystal with relation to another, along specific crystallographic planes and in certain crystallographic directions. The crystallographic planes on which slip takes place are called the ***slip*** or ***glide planes*** and the preferred direction of slip is called the ***slip direction***. (Smith, 1969)

Each crystal has one or more slip planes and one or more slip directions. The number of combinations of slip planes and slip directions provided by the crystallography of a crystal structure determines the number of its ***slip systems.*** The number of slip systems is obtained by multiplication of the number of (nonparallel) geometrically distinct slip planes by the number of nonparallel slip directions contained in each of them. For ***fcc*** crystal structure, this multiplication is such that 4 (no. of nonparallel planes) x 3 (no. of nonparallel slip planes) = 12. Thus the ***fcc*** structure has 12 slip systems. Slip planes are usually those planes containing the most atoms. However, it should not be concluded that slip could occur only along slip planes.

In polycrystalline metals there are many crystals, randomly oriented, with a number of slip planes so oriented that overall slip takes place along a preferred direction. The usual method of microplastic deformation in metals is by the sliding of blocks of the crystal grains over one another. This phenomenon is called "*the deformation by slip*" as stated above, and involves three important considerations: a) slip planes; b) resolved shear stress, and c) critical shear stress. In other words the plastic deformation, at crystallographic level, can only take place on 1) preferred planes, 2) preferred directions on that plane and 3) if the resolved shear stress on such a plane exceeds the critical shear stress.

2.2 Macroscopic Examination of the Fracture Surface

Many characteristic marks on fracture surface, though visually identifiable, can better be distinguished with macroscopic examination. In the study of fatigue fractures, macroscopic examination of such features as beach marks, fracture zones, and crack initiation sites yields information relative to the kinds and magnitude of the stresses that caused failure. To examine the unique vestigial marks left on fracture surfaces in the form of fibrous, radial and final fracture zones can supply an appreciation of the relative amounts of ductility and toughness possessed by the shaft metal.

Fig.2.4 shows the fracture surface of the shaft. Fracture occurred where the 99 mm shaft stepped sharply up to 130 mm ring, which was welded onto the shaft to support it during maintenance. According to manufacturing drawing of the shaft, where the fracture occurred there should be a fillet of 5 mm radius. However, instead of fillet, there was a notch with scratches made circumferentially by turning tool, reducing the diameter to 96 mm as illustrated in Fig.2.2.b and Fig.2.3. Naturally, this notch acted as a stress riser to initiate the fracture.

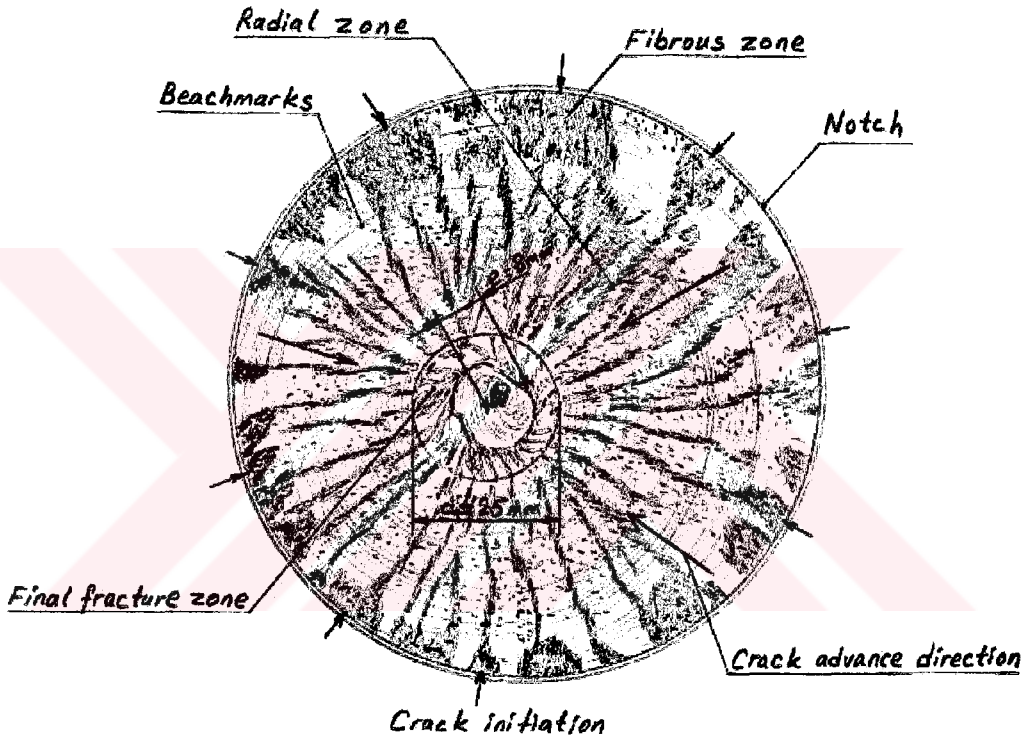

Figure 2.4 Fracture surface

As shown in Fig. 2.4 and from the images in Appendix A, the fracture surface has the typical characteristics of a fatigue failure. Because, in rotary bending, every point on the shaft periphery is subjected to tensile stress at each revolution, and therefore cracks may be initiated at the points on the periphery of the shaft. Thus, many crack

origins can be observed in figures due to shaft rotation with bending and no significant defects are observed at the origins.

At a glance, three different types of zone can be distinguished; 1) Fibrous zone, 2) Radial zone, 3) Final fracture zone.

Fibrous zone, in which the crack initiations take place first, is the slow crack propagation zone. Some sections in the zone have a gritty appearance due to cleavage of crack under tensile stress. Also, some sections flattened by the rubbing of crack surfaces are being seen. This is of the consequence that the crack surfaces are pressed together during the compressive component of the stress cycle, and mutual rubbing occurs. In general this zone shows no evidence of significant plastic deformation.

Radial zone is the fast crack propagation zone. It contains both many radial coarse lines directed to center and concentric circles about center. In early phases of crack initiation, each crack propagates in different planes and eventually some steps occur between neighbor planes. These steps appear macroscopically as lines on the fracture surface. So, radial lines indicate the crack origins.

The portion of the fracture surface associated with growth of the fatigue crack is usually fairly flat and is oriented normal to the applied tensile stress. Rougher surfaces generally indicate more rapid growth, where the rate of growth usually increases as the crack grows. Curved lines concentric about the center, called *beach marks*, are seen and mark the progress (advance) of the crack to the center during cycles. They occur due to a starting and stopping of the crack growth caused by altered stress level.

Final fracture zone has a diameter of about 25 mm. The size of this zone provides information on how big the load applied and whether the K_{IC} or K_C of the material is low or high. That is, the smaller the size is, the lower the load applied or the higher K_{IC} value the material has. As seen clearly in Fig.2.4, it can be said that the size of final fracture zone is small when comparing to that of the shaft. Thus, this indicates

both the nominal loads applied are fairly low and the shaft material is highly ductile and tough. Second thing to take note is there is an offset of 8 mm between the shaft center and zone center. This means if the shaft is subjected to bending accompanied by torsion, the final fracture zone relocates from center to edge of the shaft.

2.3 Forces and Moments Acting on the Agitator

1) Depending on process pressure, temperature and phase condition, *surface pressure* acting on the impeller varies with time. This creates nonsymmetrical tangential forces acting on the shaft. As a result, fluctuating *radial* and *axial* forces and shaft *bending moments* develop. Generally, these excitation forces are process driven and stochastic. Shaft bending vibration acts on the radial (guide) bearing, where the bearing next to the top nozzle experiences the higher force (Fig. 2.5).

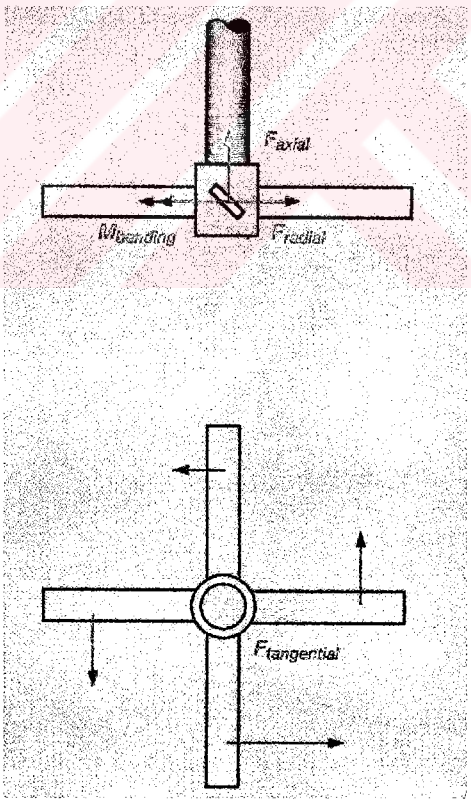

Figure 2.5 Forces acting on the impeller

2) Interactions between impeller and baffles may give rise to a harmonic torque excitation. Tork amplitude, which is superimposed on the shaft mean torque, depends on the baffle positions with respect to the impeller. In most cases, harmonic force frequency is given by shaft speed and / or shaft speed times number of impeller blades. Shaft torque acts on the gearbox hold down bolts and, multiplied by the inverse of the gear ratio, at the motor hold down bolts.

3) The weight of the shaft and impeller combination acting downward along the shaft axis creates static tension stresses on the specific cross sections depending on the shaft length that remains under the related section.

4) Drum interior (operation) pressure acting equally on the contour of the shaft (like hydrostatic pressure).

2.3.1 Calculation of the Forces

Before performing the calculations, following assumptions will be made in advance.

1) Shaft weight will not be taken into consideration, because the axial forces created, due to blade angle of 45°, during operation, carry it.

2) Drum interior (operation) pressure (2 MPa) acts like hydrostatic pressure equally over the shaft and has no effect on the general yielding, because it helps the yield point of the shaft material to increase. The explanation is that uniform compression stresses in all directions, while creating volume change and potentially large strain energies, cause no distortion of the part and thus no shear stress. If the shear stress is zero, there is no distortion and no failure. (Courtney, 2000)

3) Operation temperature (216 °C) is a moderate temperature for the shaft material and at this temperature the properties of the material do not change considerably but ductility and fracture toughness increase at moderately high temperatures up to about 350 °C as a good effect.

4) In calculations only one shaft diameter of 99 mm will be used where necessary for the sake of convenience.

5) The material is assumed to be isotropic and homogeneous.

After these assumptions, as mentioned above, during operation, the unsymmetrical radial and axial forces created by the process condition varying with time cause the agitator shaft to wobble. Consequently, there is a strong interaction between the shaft motion and the top structure. This interaction is reflected to the top structure as vibration. That is, the top structure also wobbles within the very small displacements. Eventually the top structure can be considered like a beam trying to bend under effect of concentrated force acting on its free end. This situation was illustrated in Fig. 2.6.

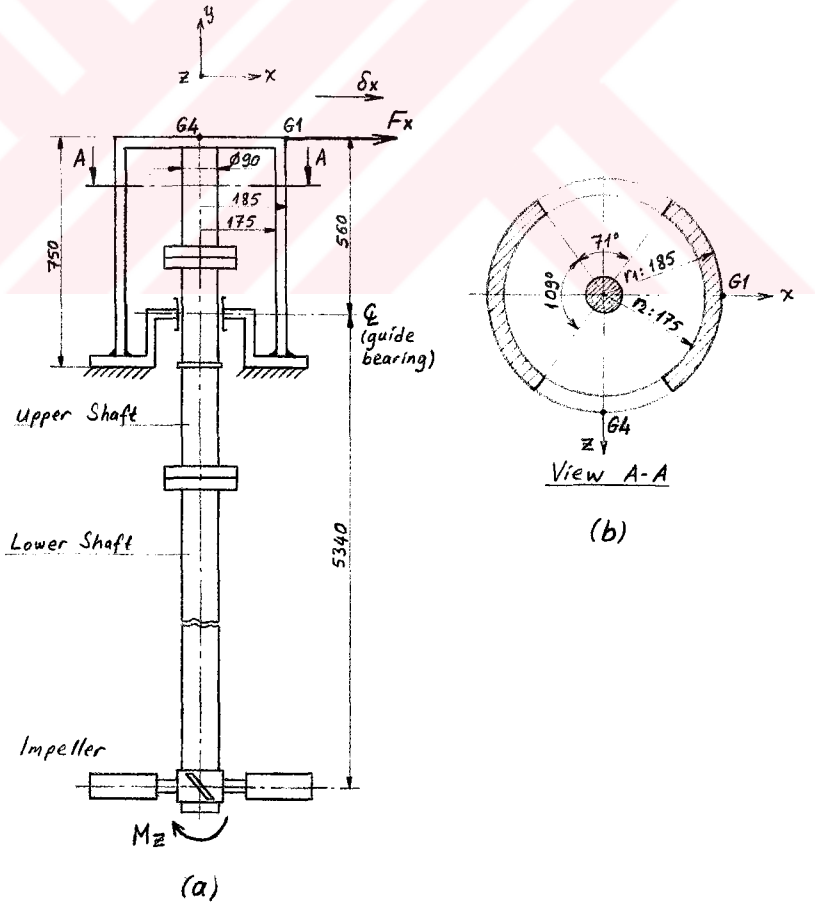

Figure 2.6 Agitator sketch

Thus, to observe vibration at some specific points, for example G1and G4 in the x and z directions respectively, as shown in Fig. 2.6, can provide very useful data. These points are identified and oriented on the top structure and saved in the computer memory before. The reason of taking measurements in both x and z directions is to get more realistic data on how the top structure behaves and to be able to compare the results with each other to get the reasonable mean value of displacements.

To be able to predict the forces acting on the system as much correct as the real ones, about 20 vibration measurements have been taken from the points G1 and G4. Among them the ones taken under the more favorable operating conditions such as full load, without any effects coming from environment were selected for evaluation. The related spectrum, waveform graphs and lists of spectral peaks for the points G1 and G4 are given in Fig. 2.7, Fig. 2.8 and Table 2.3, Table 2.4 respectively.

As seen from the graphs, the respond (vibration) of the top structure has been varying randomly with time and some peaks and valleys of higher (absolute) value are being seen in some cycles. But, although they have the higher values they do not represent the general behavior because they are transient. So, instead of them, to employ the mean value that best describes the behavior is more logical.

By making use of waveform graphs, the mean displacement values can be determined. For this, the peaks and the valleys in each cycle are located on the graphs, as seen in Fig. 2.9 and Fig. 2.10, and the values read for the points G1 and G4 are tabulated as given in Table 2.5 and Table 2.6. After some arithmetic the mean values for the peaks and valleys are obtained. From the results it can be revealed that the point G1 has the highest mean displacement value of 19 μm in the x – direction. Thus, in calculating the forces this value will be taken as basis for the sake of being of the highest value.

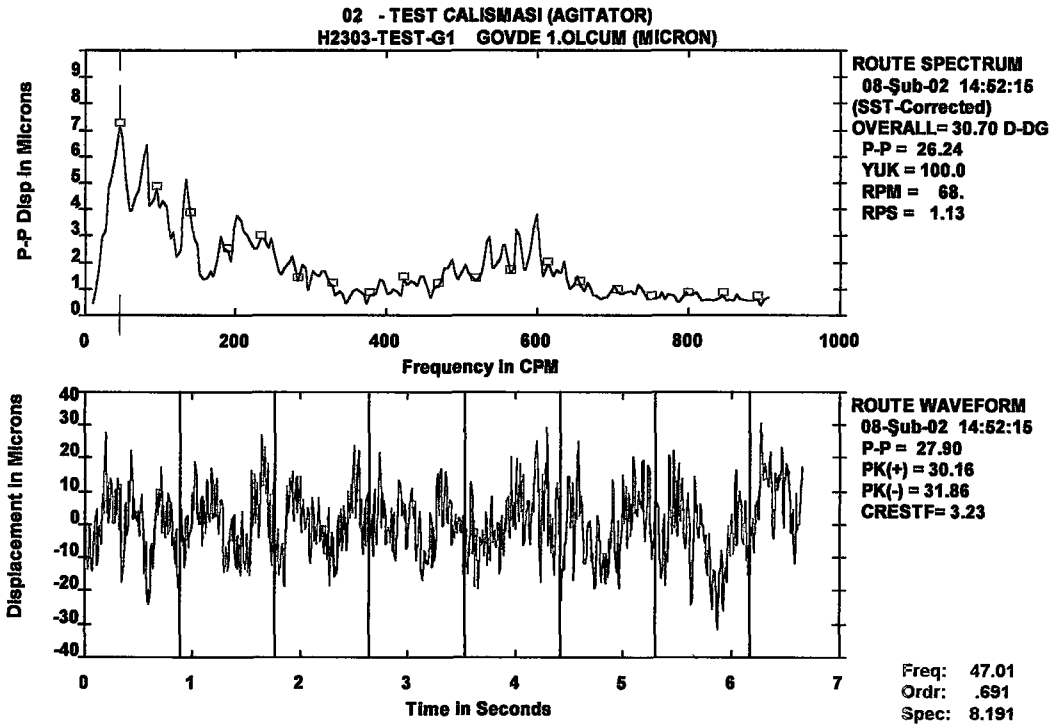

Figure 2.7 Vibration Spectrum and Waveform taken from measuring point G1

Table 2.3 List of spectral peaks of measuring point G1

Equipment: AGITATOR- H2303 Measuring Point: TEST – G1 Date/Time: 08-Feb-02 14:52:15 RPM= 68.00 Units= Microns P-P							
PEAK NO.	FREQUENCY (CPM)	PEAK VALUE	ORDER VALUE	PEAK NO.	FREQUENCY (CPM)	PEAK VALUE	ORDER VALUE
1	47.0	8.1910	.691	13	290.0	2.1557	4.265
2	79.0	7.2863	1.162	14	303.5	1.8833	4.463
3	92.5	5.3722	1.361	15	317.2	1.9743	4.664
4	101.4	4.9631	1.492	16	484.3	2.2996	7.122
5	115.1	3.5640	1.692	17	502.1	2.1212	7.384
6	133.4	5.5640	1.962	18	533.5	3.4120	7.845
7	168.4	1.8554	2.477	19	555.8	3.1100	8.173
8	181.8	3.2750	2.673	20	573.4	3.6992	8.433
9	204.6	4.3221	3.009	21	596.9	4.1752	8.778
10	236.3	3.4198	3.475	22	614.3	2.2423	9.034
11	245.7	3.2387	3.613	23	627.4	1.9687	9.227
12	272.7	2.4918	4.010	24	633.1	2.1579	9.310
SUBSYNCHRONOUS 8.1910 / 18 %		SYNCHRONOUS 4.9889 / 7 %			NONSYNCHRONOUS 16.5670 / 75 %		

T.C. YÜKSEKÖĞRETİM KURULU
DOKÜMANTASYON MERKEZİ

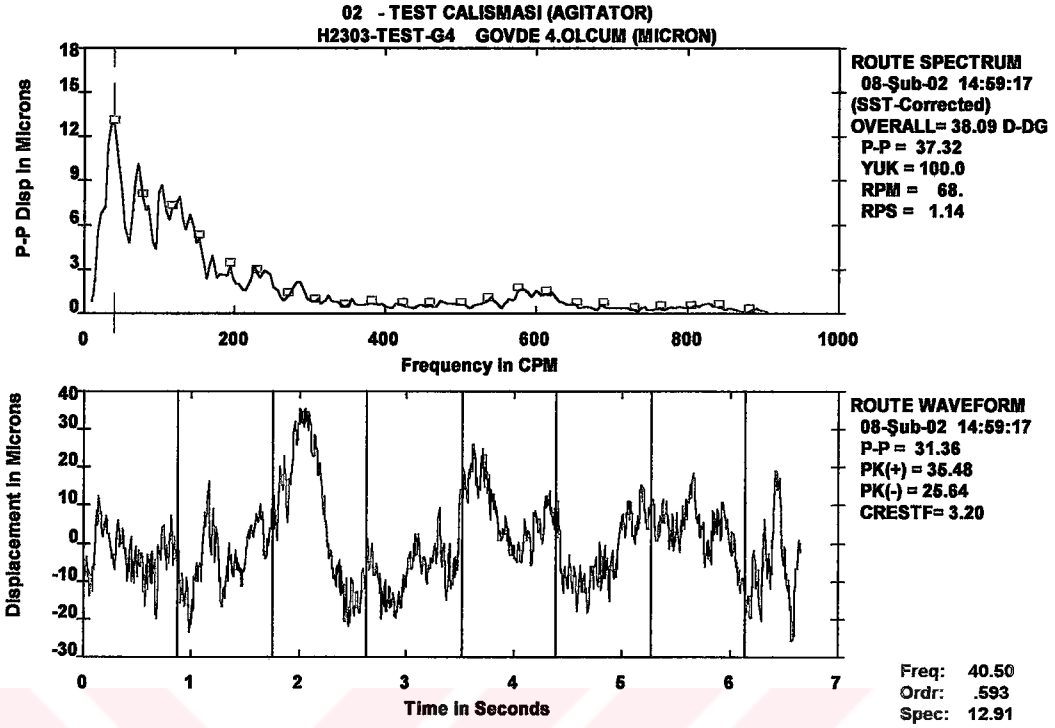

Figure 2.8 Vibration spectrum and Waveform taken from measuring point G4

Table 2.4 List of spectral peaks of measuring point G4

Equipment: AGITATOR- H2303 **Measuring Point: TEST – G4** **Date/Time: 08-Feb-02 14:59:17 RPM= 68.00 Units= Microns P-P**							
PEAK NO.	**FREQUENCY (CPM)**	**PEAK VALUE**	**ORDER VALUE**	**PEAK NO.**	**FREQUENCY (CPM)**	**PEAK VALUE**	**ORDER VALUE**
1	40.5	12.9101	.561	13	226.8	3.5536	3.321
2	70.2	11.2130	1.028	14	240.7	3.3701	3.525
3	83.4	8.3750	1.221	15	285.7	2.4330	4.185
4	101.5	9.9080	1.486	16	309.0	1.1034	4.525
5	119.2	8.3907	1.746	17	325.3	1.2541	4.765
6	124.1	8.8560	1.818	18	354.3	1.0074	5.189
7	141.4	7.5091	2.071	19	541.5	1.2445	7.930
8	151.0	5.8150	2.212	20	564.1	1.1320	8.262
9	169.3	4.3367	2.479	21	582.7	1.9324	8.534
10	182.3	3.1100	2.669	22	600.3	1.7705	8.792
11	192.0	3.4283	2.812	23	613.9	1.5348	8.991
12	204.8	2.3559	2.999	24	619.3	1.6005	9.071
SUBSYNCHRONOUS 15.1286 / 27 %		SYNCHRONOUS 2.8117 / 1 %			NONSYNCHRONOUS 24.8855 / 72 %		

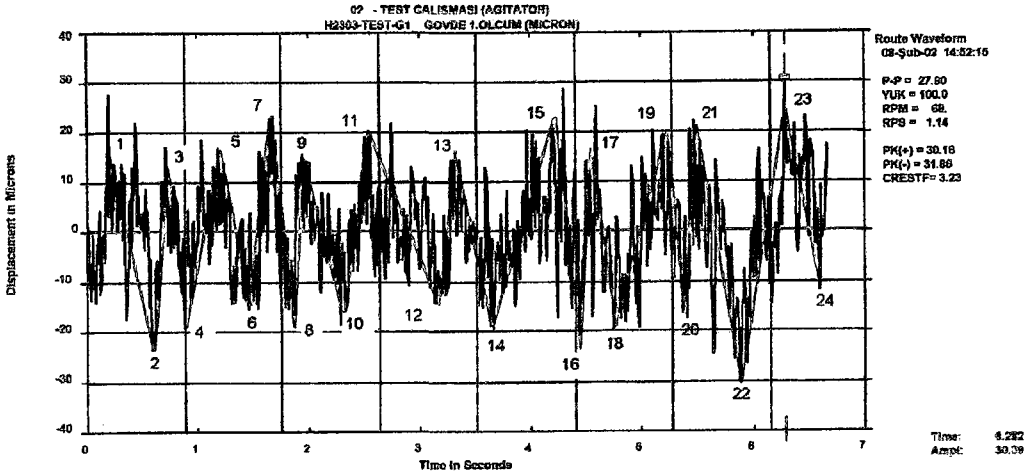

Figure 2.9 Peaks and valleys located on the waveform of point G1

Table 2.5 Mean values of peaks and valleys for point G1

Peak No.	Value (μm)	Mean Value	Valley No.	Value (μm)	Mean Value
1	17		2	23	
3	12		4	19	
5	17		6	15	
7	24		8	19	
9	15		10	17	
11	20	$\frac{228}{12} = 19\,\mu m$	12	15	$\frac{206}{12} = 17.16\,\mu m$
13	17		14	19	
15	23		16	23	
17	17		18	19	
19	20		20	16	
21	21		22	30	
23	25		24	10	

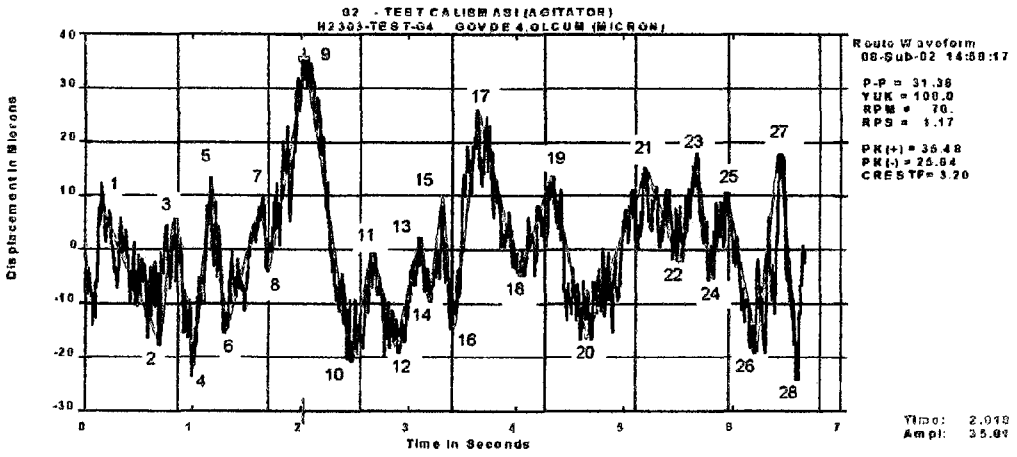

Figure 2.10 Peaks and valleys located on the waveform of point G4

Table 2.6 Mean values of peaks and valleys for point G4

Peak No.	Value (μm)	Mean Value	Valley No.	Value (μm)	Mean Value
1	8		2	17	
3	5		4	21	
5	13		6	15	
7	9		8	4	
9	35		10	20	
11	0		12	18	
13	2	$\frac{183}{14} = 13.07\ \mu m$	14	10	$\frac{188}{14} = 13.42\ \mu m$
15	10		16	14	
17	26		18	5	
19	13		20	13	
21	15		22	2	
23	18		24	5	
25	11		26	19	
27	18		28	25	

Again, referring to Fig. 2.6, the necessary calculations were performed as presented here below:

2.3.1.1 Inertia Moments of the Cross-Sections

a) Top structure (refer to Fig. 2.6.b)

about *x*-axis

$$I_{x1} = 2\frac{1}{8}(2\alpha - Sin2\alpha)(r_1^4 - r_2^4) \tag{2.1}$$

about *z*-axis

$$I_{z1} = 2\frac{1}{8}(2\alpha + Sin2\alpha)(r_1^4 - r_2^4) \tag{2.2}$$

b) Shaft

$$I_{x2} = I_{z2} = \frac{\pi d^4}{64} \tag{2.3}$$

where d = 0.09 m

The calculated values of inertia moments from Eq. 2.1, 2.2, 2.3 are given in Table 2.7

Table 2.7 Inertia moments

Top structure	I_{x1} (m^4)	5.5848e-5
	I_{z1} (m^4)	1.6622e-4
Shaft	I_{x2} (m^4)	3.22e-6
	I_{z2} (m^4)	

2.3.1.2 Calculation of the Bending Forces

In the *x*- direction :

the deflection (displacement) of the top structure:

$$\delta_x = \frac{F_{x1} L_1^3}{3EI_{z1}} \Rightarrow F_{x1} = \frac{3EI_{z1}\delta_x}{L_1^3} \tag{2.4}$$

where: L_1= 0.75 m

δ_x = 19 μm = 1.9e-5 m

E = 200e9 GPa

I_{z1} = 1.6622e-4 m^4

the deflection (displacement) of the shaft:

$$\delta_x = \frac{F_{x2} L_2^3}{3EI_{z2}} \Rightarrow F_{x2} = \frac{3EI_{z2}\delta_x}{L_2^3} \tag{2.5}$$

where : L_2 = 0.56 m

δ_x = 19 μm = 1.9e-5 m

E = 200e9 GPa

I_{z2} = 3.22e-6 m^4

The total force in the *x* – direction:

$$F_x = F_{x1} + F_{x2} \tag{2.6}$$

The total force in the *z* – direction:

$$F_z = F_{z1} + F_{z2} \tag{2.7}$$

The forces F_{z1} and F_{z2} in the z - direction can be found in a similar manner followed above and all forces are given in Table 2.8.

Table 2.8 The forces acting on the top structures

x – direction (N)			z – direction (N)		
F_{x1}	F_{x2}	ΣF_x	F_{z1}	F_{z2}	ΣF_z
4492	209	**4701**	1066	148	**1214**

2.3.1.3 Calculation of the Forces (F_{xl} and F_{zl}) Acting on the Impeller

The shaft was considered as if it were a lever with a fulcrum close to top end and forces acting on each end but in the opposite directions. This situation is shown in Fig. 2.11 below.

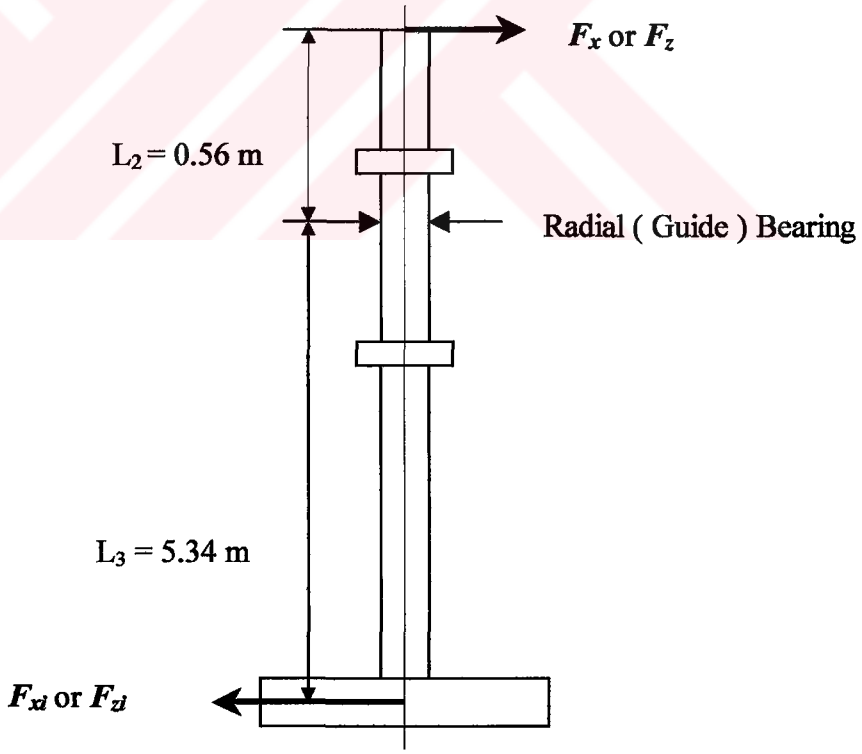

Figure 2.11 Sketch for calculation of the impeller forces

According to situation given in the sketch of Fig. 2.11, equations can be written to obtain the impeller forces F_{xi} and F_{zi} as follows:

$$F_x L_2 = F_{xi} L_3 \quad (2.8)$$

$$F_z L_2 = F_{zi} L_3 \quad (2.9)$$

Solving Eq. 2.8 and 2.9 for F_{xi} and F_{zi}, they are obtained as follow.

F_{xi} = **493 N**

F_{zi} = 127 N

For the stress analysis of the shaft, it is natural and logical to employ the force F_{xi} since it is higher than F_{zi} and creates higher stresses.

2.3.1.4 Calculation of Tork Applied to the Shaft

The Tork value was calculated by applying two different procedures as presented here below:

The First Procedure:

As seen in the graph of Fig. 2.12, which was recorded during operation, the amps drawn by the electrical motor of the agitator have been ranging 7.4 amps to 8.2 amps during operation. Thus, consequently, the tork applied to the shaft also varies between the values calculated as follows.

Power equation of the electrical motor

$$P = V\ A\ \cos\varphi \quad (2.10)$$

where: P: power (watt)

V: 380 volt

A: 7.4 to 8.2 amper

$cos\varphi$: 0.83 (power factor)

P_{min} = 2344 Watt

P_{max} = 2586 Watt

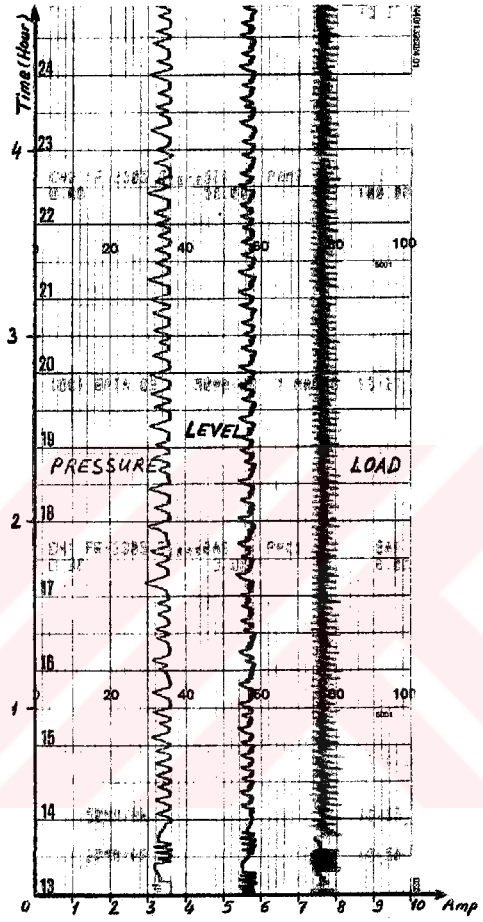

Figure 2.12 The load (Ampere) graph of agitator

Now, after obtaining the max. and min. power of the electrical motor, the max. and min. tork values can be calculated

$$P = \omega \; T = 2 \; \pi \; n \; T \qquad (2.11)$$

where: P: power (watt)

$\omega = 2 \; \pi \; n$: angular velocity (rad / sn)

n: speed (68 / 60 = 1.13 rps)

Solving Eq. 2.11 for T_{min} and T_{max}, they are obtained as follow.

T_{min} = 329 Nm

T_{max} = 364 Nm

The second procedure:

In this procedure, the method presented in (McCabe & Smith, 1967) was utilized as follows :

The power consumption in an agitated vessel is a function of the variables, that is:

$$P = \varphi(n, D_a, g_c, \mu, g, \rho) \tag{2.12}$$

where : n : speed

D_a : impeller diameter

g_c : Newton's law conversion factor

μ : viscosity

g : acceleration of gravity

ρ : density

From Eq. 2.12, the ***Power Number (N_p)*** from which the power will be calculated can be written like this:

$$N_p = \frac{P * g_c}{n^3 * D_a^5 * \rho} = \varphi\left(\frac{n * D_a^2 * \rho}{\mu}, \frac{n^2 * D_a}{g}\right) \tag{2.13}$$

by taking account of the shape factors Eq. 2.13 can be rewritten

$$N_p = \frac{Pg_c}{n^3 D_a^5 \rho} = \varphi\left(\frac{nD_a^2\rho}{\mu}, \frac{n^2 D_a}{g}, S_1, S_2, ..., S_n\right) \tag{2.14}$$

where: $S_1 = \frac{D_t}{D_a}, S_2 = \frac{E}{D_a}, S_3 = \frac{L}{D_a}, S_4 = \frac{W}{D_a}, S_5 = \frac{J}{D_a}, S_6 = \frac{H}{D_a}$

for the shape factors refer to Fig. 2.1

$\frac{nD_a^2\rho}{\mu} = N_{\mathrm{Re}}$: Reynolds Number

$\frac{n^2 D_a}{g} = N_{Fr}$: Froude Number

Eq. 2.14, now, can be stated as follows

$$N_p = \varphi(N_{\mathrm{Re}}, N_{Fr}, S_1, S_2, ..., S_n) \tag{2.15}$$

However, in baffled tanks at Reynolds numbers larger than about 10000, the power function is independent of Reynolds number and viscosity is not a factor. Changes in N_{Fr} have no effect. In this range, the flow is fully turbulent. For this reason Eq. 2.15 can be rewritten as independent of N_{Re} and N_{Fr}.

$$N_p = \varphi(S_1, S_2, ..., S_n) \tag{2.16}$$

From Eq. 2.16, power P can be extracted as follows

$$P = \frac{N_p n^3 D_a^5 \rho}{g_c} \tag{2.17}$$

Now, using Eq.2.17, the power is calculated as below:

Some necessary data taken from the specification sheet of vessel:

Convertions

D_a = 1100 mm

μ = 0.5 cp at 216 °C

ρ = 984 kg / m³ at 216 °C

g = 9.81 m / sn²

n = 68 rpm = 1.13 rps

D_a = 3.6 ft

μ = 3.36e-4 lb / ft.sec

ρ = 61.43 lb / ft³

$g = g_c$ = 32.17 ft / sec²

$$N_{Re} = \frac{nD_a^2\rho}{\mu} \qquad N_{Re} = 2.67e6 > 10000 \text{ (flow is fully turbulent)}$$

Because the flow is fully turbulent, power number is only function of shape factors. From the graphs given in (Chem. Eng. Handbook, 1973):

N_p = 3.4325 found for impeller with ***four flat blades***

When the blades make a 45° angle with the impeller shaft, N_p is 0.4 times the value when the blades are parallel with the shaft, that is:

$$N_{p\,45°} = 0.4\, N_{p\,90°}$$

$$N_{p\,45°} = 1.373$$

For a six-bladed impeller, N_p increases directly with S_4, but for a four-bladed impeller N_p increases with $S_4^{1.25}$, that is:

$$S_4 = \frac{W}{D_a} = \frac{243}{1100}$$

$$S_4 = 0.22$$

$$S_4^{1.25} = (0.22)^{1.25} = 0.15$$

for this value, from the graph given in (Chem. Eng. Handbook, 1973), N_p found as

$N_p = 1.143$

Substituting all values obtained in Eq. 2.17

$P = 1904.24$ ft³.lb / sec

$P = 2.548 = 2548$ Watt obtained.

From the equation giving the relation between Power and Tork

$$P = \omega T = 2 \pi n T \qquad (2.18)$$

where: P : Watt , T : Nm , ω : rad / s , n : rps
Solving Eq. 2.18 for T, it is obtained

$$\boldsymbol{T = 359 \text{ Nm}}$$

It can be seen that, the results obtained from both first procedure and second procedure coincides with each other.

T.C. YÜKSEKÖĞRETİM KURULU
DOKÜMANTASYON MERKEZİ

CHAPTER THREE
STRESS ANALYSIS

3.1 Stress Analysis

At this step, the stress analysis will be carried out in two different ways: 1) analytic, and 2) by a computer program called ANSYS. Having been obtained, the results will be compared with each other.

After obtaining the Bending Force and Tork, it can be in progress to analyze the bending stresses due to impeller force F_i and the shear stresses due to Tork T applied to the shaft.

3.1.1 Analytic Solution

In the first way, the illustration was drawn as shown in Fig. 3.1 to represent the agitator shaft. As seen from the illustration the shaft was trimmed with the all items such as dimensions, crack plane, forces and moments, shear and bending moment diagrams necessary for analysis. It was also considered like a vertical cantilever beam fixed at its top end. The interested points A, B, C, D on which the stresses will be evaluated were located on the perimeter of crack plane.

Let the shaft be cut in at the crack plane as seen in Fig. 3.2 and now the equations to find the moments, shear force and reactions at the fixed end can be written as follow:

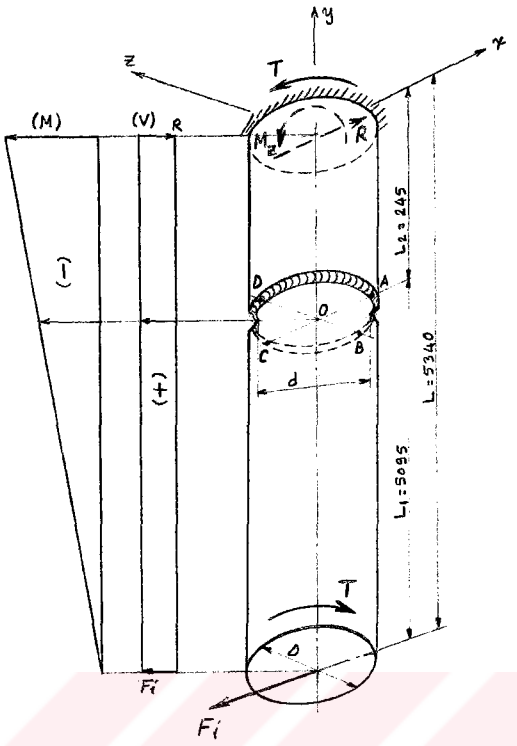

Figure 3.1 The shaft sketch to show the bending moment and shear force at the crack plane

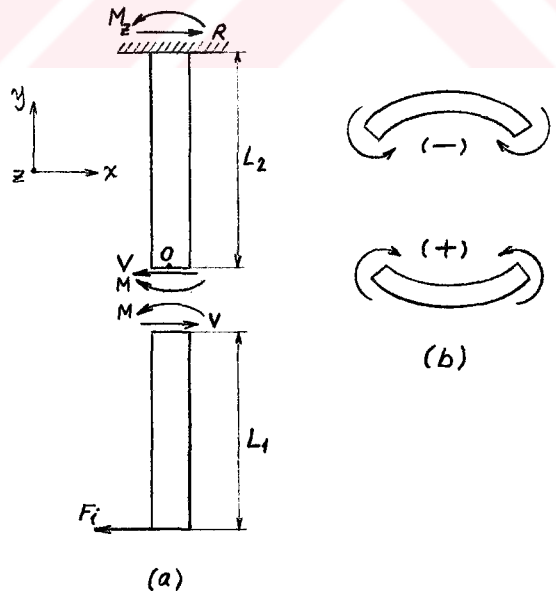

Figure 3.2 The shaft cut in the crack plane. a) Shear force and bending moment, b) The sign convention for bending moment

3.1.1.1 Calculation of Bending Moment *(M)* and Shear Force *(V)*

Referring to Fig. 3.1 and Fig. 3.2

* Reaction force at the fixed end:

$$\Sigma F_x = 0 \qquad R - F_i = 0 \qquad R = F_i = 493 \text{ N}$$

* Reaction moment at the fixed end:

$$\Sigma M_z = 0 \qquad M_z - F_i L = 0 \qquad M_z = 2633 \text{ Nm}$$

* Shear force *(V)* and bending moment *(M)* acting on the crack plane:

$$\Sigma F_x = 0 \qquad R - V = 0 \qquad R = V = F_i = 493 \text{ N}$$

$$\Sigma \text{Mo} = 0 \qquad - M + M_z - R L_2 = 0 \qquad \mathbf{M = 2512 \text{ Nm}}$$

3.1.1.2 Calculation of the Nominal Stresses Acting on the Points A, B, C, D of the Notch (crack)

1) The Tork *T* causes a shear stress at $r = d / 2$, (d = 96 mm = 0.096 m) (Fig. 3.3)

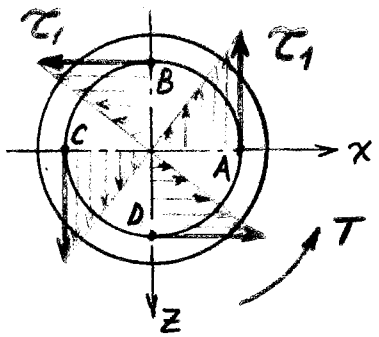

Figure 3.3 The nominal shear stresses created in the fracture plane

T.C. YÜKSEKÖĞRETİM KURULU
DOKÜMANTASYON MERKEZİ

$$\tau_1 = \frac{Tr}{J_y} = \frac{Td/2}{(\pi/32)d^4} = \frac{16T}{\pi d^3} \tag{3.1}$$

$\tau_1 = 2.095$ MPa

2) The transverse impeller force F_i causes both bending stress and transverse shear stress

a) Bending stress (Fig. 3.4)

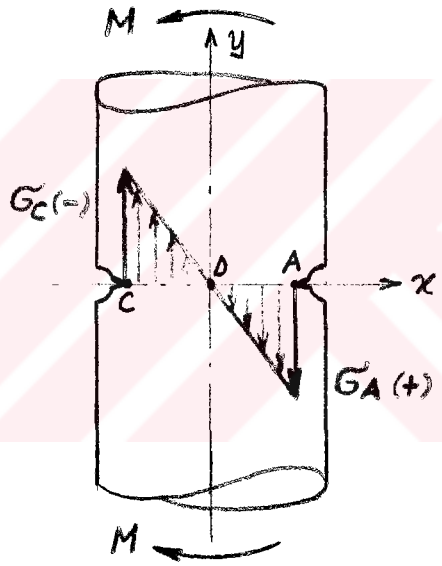

Figure 3.4 The nominal bending stresses created in the fracture plane

$$\sigma_{A,C} = \pm\frac{Mx}{I_z} = \frac{Md/2}{(\pi/64)d^4} = \frac{32M}{\pi d^3} \tag{3.2}$$

$\sigma_A = 28.92$ MPa

$\sigma_C = -28.92$ MPa

b) Transverse shear stress (Fig.4.5)

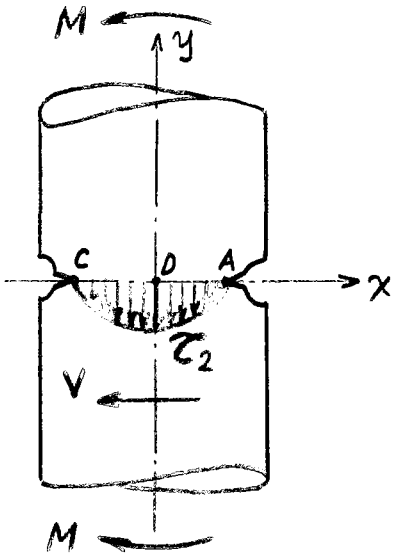

Figure 3.5 Transverse shear stresses due to bending created in the fracture plane

$$\tau_2 = \frac{4V}{3A} = \frac{4V}{3(\pi/4)d^2} = \frac{16F_i}{3\pi d^2} \tag{3.3}$$

$\tau_2 = 0.946$ MPa

3.1.1.3 Combined Stresses at the Points A, B, C, D by Superposition

Point A: $\underline{\sigma_A = 28.92 \text{ MPa}}$ $\tau_A = \tau_1$

$\underline{\tau_A = 2.095 \text{ MPa}}$

Maximum Shear Stress:

$$\tau_{A\max} = \sqrt{\left(\frac{\sigma_{Ay} - \sigma_{Az}}{2}\right)^2 + (\tau_{Ayz})^2}$$ where: $\sigma_{Ay} = \sigma_A$, $\sigma_{Az} = 0$, and $\tau_{Ayz} = \tau_A$

τ_{Amax} = **14.61 MPa**

Principal Stresses:

$$\sigma_{A1} = \frac{\sigma_{Ay} + \sigma_{Az}}{2} + \tau_{A\max} \tag{3.4}$$

σ_{A1} = **29.07 MPa**

σ_{A2} = **0**

$$\sigma_{A3} = \frac{\sigma_{Ay} + \sigma_{Az}}{2} - \tau_{A\max} \tag{3.5}$$

σ_{A3} = **- 0.15 MPa**

Point B: $\sigma_B = 0$ $\tau_B = \tau_1 + \tau_2$

$\tau_B = 3.041$ MPa

Point C: σ_A = -28.92 MPa $\tau_C = \tau_1$

τ_C = 2.095 MPa

τ_{cmax} = **14.61 MPa**

σ_{c1} = **- 29.07 MPa**

Point D: $\sigma_D = 0$ $\tau_D = \tau_1 - \tau_2$

τ_D = 1.149 MPa

It is clear from the results that the largest tensile and combined shear stresses occur on Point A and Point B respectively. While the largest principal stress appears to be σ_{A1} = 29.07 MPa on Point A, the maximum shear stresses appear to be $\tau_{A,Cmax}$ = 14.61 MPa on both Point A and Point C.

3.1.1.4 Calculation of Maximum Stresses Arising from Shape of the Notch by Taking into Consideration of Stress Concentration Factors

As shown above, the formulas for determining stresses are based on the assumption that the distribution of stress on any section of the shaft can be expressed by a mathematical law or equation of relatively simple form. In a shaft subjected to a bending or torsional load the stress is assumed to be distributed uniformly over each cross section, that is, the stress is assumed to increase directly with the distance from the neutral axis.

This assumption may be in error in many cases. The conditions that may cause the stress at a point in a shaft to be radically different from the value calculated from simple formulas include effects such as abrupt changes in section, cracks that exist in the member, notches and scratches, which may be result of fabrication. These conditions that cause the stresses to be grater than those given by the ordinary stress equations are called *discontinuities* or *stress raisers.* These stress raisers cause sudden increases in the stress (stress peaks) at points near them. Often, large stresses due to discontinuities are developed in only a small portion of a member. Hence, these stresses are called *localized stresses* or simply *stress concentrations.*

The amount of stress concentration in any particular geometry is denoted by a geometric stress-concentration factor k_t for normal stresses, or as k_{ts} for shear stresses. The maximum stress at a local stress-raiser is then defined as

$$\sigma_{max} = k_t \sigma_{nom}$$

$$\tau_{max} = k_{ts} \tau_{nom} \qquad (3.6)$$

T.C. YÜKSEKÖĞRETİM KURULU
DOKÜMANTASYON MERKEZİ

where σ_{nom} and τ_{nom} are the nominal stresses calculated for the particular applied loading and net cross section assuming a stress distribution across the section that would obtain for a uniform geometry. Thus, the nominal stresses are calculated using the **net cross section**, which is *reduced by the notch geometry*, i.e., using d of 96 mm instead of D of 99 mm as the diameter from the tip to tip of notches in Fig. 3.3 through Fig. 3.5.

At this point, it should be noted that the values to be calculated for k_t and k_{ts} are only for static loading conditions. Since the shaft is subjected to dynamic loading, somewhat different stress concentration factors should be applied when dynamic loads such as fatigue are present. So k_t and k_{ts} need to be modified by a parameter called notch sensitivity q, which is defined for various materials. This procedure will be discussed later in Fatigue Analysis. However, at this stage, k_t and k_{ts} will be employed to obtain the stresses by accepting as if the loads were static. Because it might be said that all stress analyses are basically fatigue analyses, the differences lying in the number of cycles of applied stress. So the calculated loads may be treated as a single cycle (Osgood).

(Young & Budynas, 2002) provides tables of stress concentration factors for a number of cases representing commonly encountered situations in design. From these tables, the appropriate ones to be employed for each loading case are picked to obtain k_t and k_{ts} and applied as follows:

Torsion (Fig. 3.6)

$$k_{ts} = C_1 + C_2\left(\frac{2h}{D}\right) + C_3\left(\frac{2h}{D}\right)^2 + C_4\left(\frac{2h}{D}\right)^3 \tag{3.7}$$

where: D: shaft diameter, h: notch depth

for $0.25 \le h/r \le 2$, $h/r = 1.5 / 1.75 = 0.875$, r: notch radius

$$C_1 = 1.245 + 0.264\sqrt{h/r} + 0.491 * h/r \Rightarrow C_1 = 1.8935$$
$$C_2 = -3.03 + 3.269\sqrt{h/r} - 3.633 * h/r \Rightarrow C_2 = -3.1172$$
$$C_3 = 7.199 - 11.286\sqrt{h/r} + 8.318 * h/r \Rightarrow C_3 = 3.8795$$
$$C_4 = -4.414 + 7.753\sqrt{h/r} - 5.176 * h/r \Rightarrow C_4 = -1.6725$$

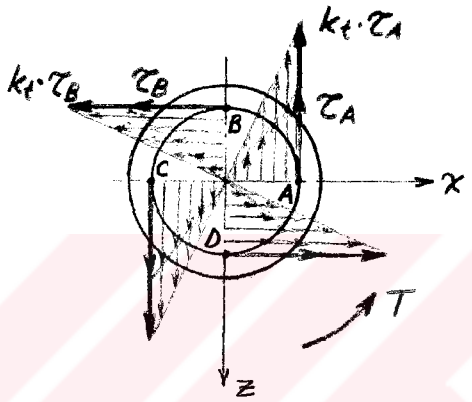

Figure 3.6 Elevated shear stresses due to notch effect in the fracture plane

Substituting C_1, C_2, C_3, C_4 into Eq. 3.7

$k_{ts} = 1.8025$, Thus

$$\tau_{B\max} = k_{ts}\tau_B$$
$$\tau_{B\max} = 5.48 \text{ MPa}$$

Bending (Fig. 3.7)

In a similar way;

$C_1 = 2.9009$, $C_2 = -6.949$, $C_3 = 9.1394$, $C_4 = -4.0921$

$k_t = 2.6986$, Thus

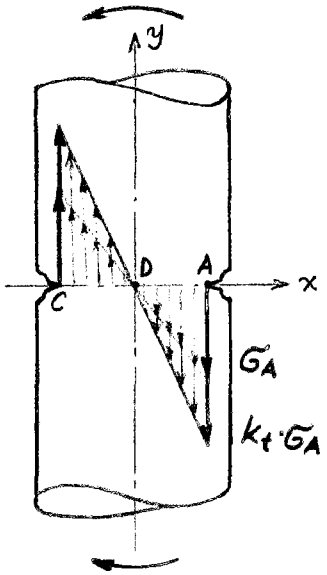

Figure 3.7 Elevated bending stresses due to notch effect in the fracture plane

$$\sigma_{A\max} = k_t \sigma_A$$

$$\sigma_{A\max} = 78 \text{ MPa}$$

Principal stress:

$$\sigma_{1\max} = k_t \sigma_1$$

$$\sigma_{1\max} = 78.448 \text{ MPa}$$

Maximum shear stress:

$$\tau_{A\max 1} = k_t \tau_{A\max}$$

$$\tau_{A\max 1} = 39.426 \text{ MPa}$$

The results reveal that all stresses are well below the yield strength (σ_{ys} or S_{ys} = 205 MPa) of shaft material AISI Type 304 SS. However these results obtained conventionally do not seem reasonable because, in order for a crack can be initiated, a plasticity at the notch tip must be introduced by a stress exceeding the yield

strength. Therefore, it was tried to get new k_t and k_{ts} values by employing ANSYS modeling feature. It is known that ANSYS analysis gives the results including stress concentration effects, thus, it was thought that more realistic stress concentration factors could be obtained provided an appropriate model was created.

For this, first, a model of the shaft having the real notch in the midpoint was created as seen in Fig. 3.8. It has the same in dimensions as the shaft except the length, which is unity (1 m). After creating appropriate notch tip stress concentration elements and mesh generation as seen in Fig. 3.9, the loads for bending and torsion, which were so fixed that they created 10 MPa stresses on the outer ligaments of the model, were applied. Consequently, the following values were obtained.

$k_t = 7.575$

$k_{ts} = 5.9406$

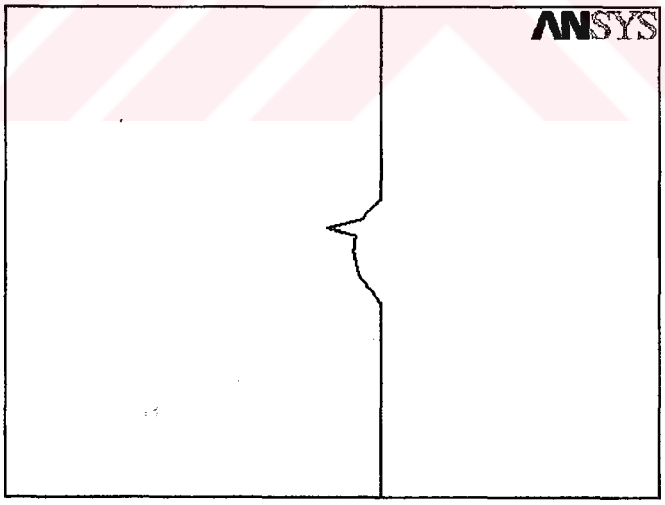

Figure 3.8 The model of the notch to calculate the stress concentration factor

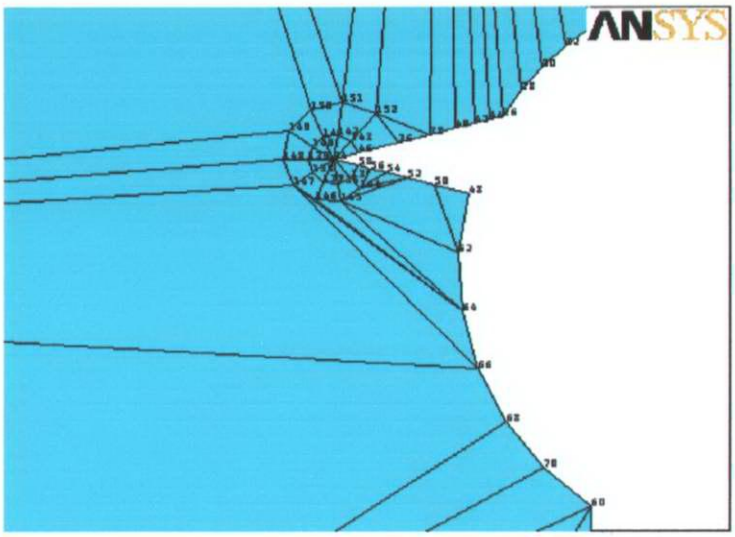

Figure 3.9 Notch tip stress concentration elements and mesh generation.

By making use of these values, the elevated stresses at the notch tip are obtained as follows:

Bending

$\sigma_{Amax} = k_t \sigma_A$ $\sigma_{Amax} = 219$ MPa

First principle stress

$\sigma_{1max} = k_t \sigma_1$ $\sigma_{1max} = 220.2$ MPa

Maximum shear stress

$\tau_{Amax1} = k_t \tau_{Amax}$ $\tau_{Amax1} = 110.67$ MPa

For torsion

$\tau_{Bmax} = k_{ts} \tau_B$ $\tau_{Bmax} = 18$ MPa

In the last case, at point A, the stresses created by bending exceed the yield points of the shaft material (σ_{ys} or S_{ys} = 205 MPa and $\tau_{ys} = 0.5\ \sigma_{ys}$ = 102 MPa) but shear stress created by torsion is still more below the shear strength (τ_{ys}). This means that the torsional stresses do not contribute to general yielding.

3.1.2 Stress Analysis by ANSYS Program

The plane strain linear elastic finite element analysis was performed on the model of shaft. The ANSYS 5.4 finite element program was utilized, and all element meshes were generated using the element type PLANE 83, 8-Node, Axisymmetric-Harmonic Structural Solid.

The reasons to prefer the element type PLANE 83 are that, 1) it is used for two-dimensional modeling of axisymmetric structures with nonaxisymmetric loading such as bending, shear, and torsion, 2) it has compatible displacement shapes and is well suited to model curved boundaries, 3) it provides more accurate results for mixed (quadrilateral-triangular) automatic meshes and can tolerate irregular shapes without as much loss of accuracy, 4) the use of an axisymmetric model greatly reduces the modeling and analysis time compared to that of an equivalent three-dimensional model, avoiding struggling with numerous nodes created inherently in 3D analysis.

Analysis Assumptions

The loads are applied at only one node for convenience. Nodal forces due to the loads are applied on full circumference (360°) basis and calculated for symmetric modes [Torsion (Mode = 0), Bending (Mode = 1)] as follows:

1) The total applied Tork (T) due to a tangential input force ($\boldsymbol{F_Z}$) acting about the global axis is:

$$T = \int_0^{2\pi} \text{(force per unit length) (lever arm) (increment length)}$$

$$T = \int_0^{2\pi} (-F_Z / 2\,\pi\, r_{ap})\,(r_{ap}\, d\theta)$$

$$T = -F_Z\, r_{ap} \quad \text{or}$$

$$F_Z = -T / r_{ap} = -2\,T / d_{ap}$$

where: F_Z: input force (N)

T: tork applied (Nm) = 364 Nm

$d_{ap} = 2$ r_{ap}: lever arm (m) = 2 x 0.085 = 0.19 m

Thus: $\underline{\boldsymbol{F_Z = -3831.579\ N}}$

2) The total applied force ($\boldsymbol{F_{xi}}$) in the global x- direction due to an input radial force (F_X) is:

$$F_{xi} = \int_0^{2\pi} \text{(force per unit length) (directional cosine) (increment length)}$$

$$F_{xi} = \int_0^{2\pi} ((F_X(\cos\theta) / 2\,\pi\, r)\,(\cos\theta))\,(r\,d\theta)$$

$F_{xi} = F_X / 2$ or

$F_X = 2\,F_{xi}$

where: F_X: input radial force (N)

F_{xi}: force applied (N) = - 493 N

Thus: $\underline{\boldsymbol{F_X = -986\ N}}$

After having been converted the forces as required by ANSYS, the shaft was modeled using the real dimensions for conformity to the real shaft as shown in Fig. 3.10, and 3.11.

In order to obtain the more realistic result from analysis, an appropriate mesh generation and stress concentration elements at the notch tip were developed as shown in Fig. 3.9. Necessary constraints and forces computed above were applied separately for both torsion (Mode = 0) and bending (Mode = 1).

Figure 3.10 Shaft model in full length.

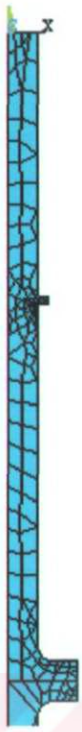

Figure 3.11 Meshed upper shaft

After getting the program to be run, the stress distributions due to bending and torsion at the tip of notch of 1.5 mm in length as seen in Fig. C1 and Fig. C2 in Appendix C were obtained.

Further, the stress analysis was repeated for crack lengths varying from 1.5 to 40 mm. Related ANSYS models and mesh generations of cracks can be shown in Fig. B1 through Fig. B10 in Appendix B. The results obtained for tensile stresses, principal stresses and Von Mises stresses due to bending loading were tabulated in Table 3.1 and only one graph showing variation of tensile stresses versus crack length was plotted as seen in Fig. 3.12.

Again, the shear stresses, principal stresses and Von Mises stresses due to torsional loading were tabulated in Table 3.2 and only one graph showing variation of shear stresses versus crack lengths was plotted as seen in Fig. 3.13.

3.1.3 Stress Intensity Factors

The underlying philosophy of the stress intensity factor approach to fracture is that the mechanical environment in the immediate vicinity of a crack tip has unique distribution, independent of loading conditions or geometric configuration, provided non-linear behavior is of limited extend. Geometry and loading conditions influence this environment through the parameter K, which may be determined by suitable analysis. This single parameter K is related to both the stress level and crack size. The determination of stress intensity factor is a specialist task necessitating the use of a number of analytical and numerical techniques. The important point to note is that it is always possible to determine K_I to a sufficient accuracy for any given geometry or set of loading conditions.

The stress intensity factor, as stated above, is a mathematical calculation relating the applied load and notch (crack) size for a particular geometry. The calculation of K is analogous to the calculation of applied stress. To prevent yielding, the applied stress is kept below the material yield strength. Thus, the applied stress is the "driving force", and the yield strength is the "resistance force". The driving force is a calculated quantity while the resistance force is a measured value. In the same sense, K is a calculated "driving force" and K_C is a measured fracture toughness value and represents the "resistance force" to crack extension. When the particular combination of stress and crack size leads to a critical value of K, called K_C, unstable crack growth fracture occurs.

To establish methods of stress analysis for cracks in elastic solids, it is convenient to define three types of relative movements of two crack surfaces. These displacement modes represent the local deformation ahead of a crack and are called as "the opening mode, Mode-I", "the sliding mode, Mode-II" and "the tearing mode, Mode-III". Hence, the magnitudes of the elastic-stress fields can be described by single-term parameters, K_I, K_{II}, K_{III} that correspond to Modes I, II, III, respectively. Consequently, the applied stress, the crack shape, size and the structural configuration associated with structural components subjected to a given mode of

deformation affect the value of the stress intensity factor but do not alter the stress field distribution.

In all cases, the general form of the stress intensity factor is given by:

$$K = \beta \sigma_{nom} \sqrt{\pi a} \tag{3.8}$$

where β is a parameter that depends on the geometry of the particular member and the crack geometry. Hence, K describes the stress field intensity ahead of a sharp notch (crack) in any structural component as long as the correct geometrical parameter, β can be determined. One key aspect of the stress intensity factor K is that it relates the local stress field ahead of a sharp crack in a structural component to the global (or nominal) stress applied to that structural component away from the crack.

For the analytic solution, the stress intensity factors K_I for Mode-I and K_{III} for Mode-III can be calculated by using the equations given in (Hellan, 1985).

For **Mode-I (Opening Mode)**

K_I is given for radial cracks around cylinders as follows:

$$K_I = \sigma_\infty \sqrt{\pi a} \left(\frac{D}{d} + \frac{1}{2} + \frac{3}{8}\frac{d}{D} - 0.36\frac{d^2}{D^2} + 0.73\frac{d^3}{D^3} \right) \frac{1}{2}\sqrt{\frac{D}{d}} \tag{3.9}$$

where: $\sigma_\infty = \sigma_{nom} = \sigma_A = 29.07$ MPa

$D = 99$ mm $= 0.099$ m

$d = 96$ mm $= 0.096$ m

$a = 1.5$ mm $= 0.0015$ m

After some calculations the value of K_I is

$K_I = 2.2514 \text{ MPa}\sqrt{m}$

For Mode-III (Tearing Mode)

K_{III} is given for radial cracks around cylinders as follows:

$$K_{III} = \tau\sqrt{\pi a}\left(\frac{D^2}{d^2} + \frac{1}{2}\frac{D}{d} + \frac{3}{8} + \frac{5}{16}\frac{d}{D} + \frac{35}{128}\frac{d^2}{D^2} + 0.21\frac{d^3}{D^3}\right)\frac{3}{8}\sqrt{\frac{D}{d}} \qquad (3.10)$$

where: $\tau = \tau_{nom} = \tau_A = 3.041$ MPa

After some calculation the value of K_{III} is

$K_{III} = 0.2151 \text{ MPa}\sqrt{m}$

As shown from the results that the values of K_I and K_{III} are more below the K_{IC} of AISI 304 SS.

With ANSYS solutions, K_I values obtained for various crack lengths have been put in Table 3.1. Also, the data in Table 3.1 are plotted as shown in Fig. 3.12.

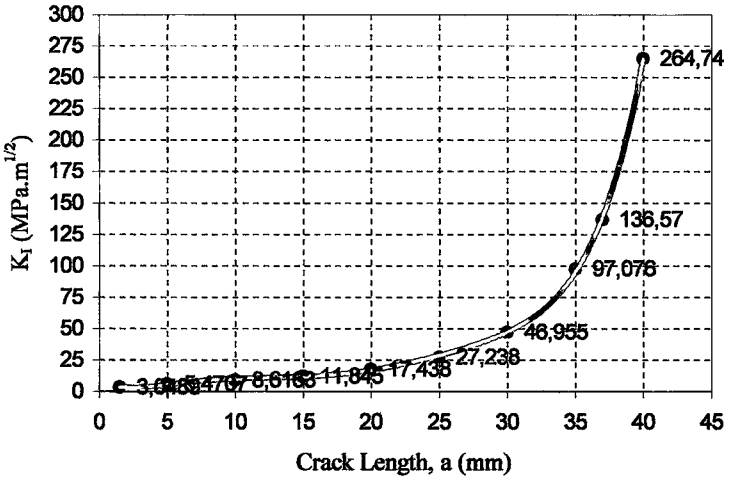

Figure 3.12 The variation of K_I vs. crack lengths.

Table 3.1 Stresses due to bending and corresponding stress intensity factors (K_I)

Crack Lengths a (mm)	Tensile Stresses S_Y (MPa)	Principal Stresses (MPa)			Von Mises SEQV (MPa)	K_I (MPa.m$^{1/2}$)
		S_1	S_2	S_3		
1.5	204	253	101	70	170	3.0489
5	238	246	139	105	127	5.4707
10	262	258	149	106	138	8.6163
15	336	406	171	105	274	11.8450
20	480	514	274	205	284	17.4380
25	522	601	350	254	314	27,2380
30	743	919	500	344	521	46.9550
35	1875	2024	1105	908	1034	97.0760
37	2736	3182	1495	936	2034	136.5700
40	4478	5508	2500	1451	3660	264.7400

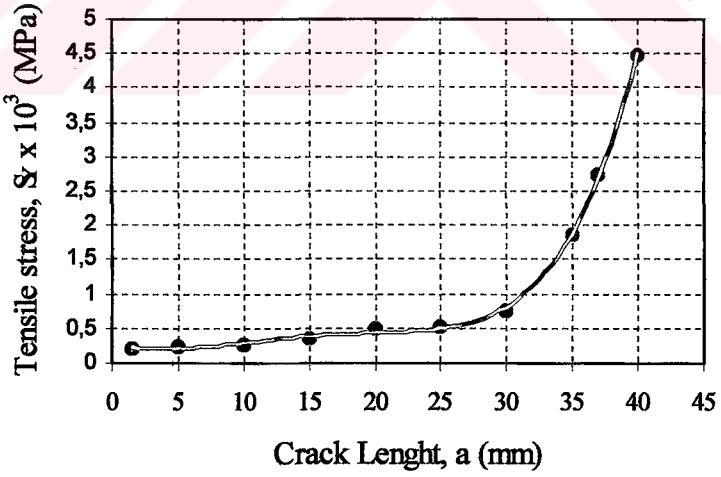

Figure 3.13 The variation of tensile stresses vs. crack lengths.

Table 3.2 Stresses due to torsion and corresponding stress intensity factors (K_{III})

Crack Lengths a (mm)	Shear Stresses S_{YZ} (MPa)	Principal Stresses (MPa)			Von Mises SEQV (MPa)	K_{III} (MPa.m$^{1/2}$)
		S_1	S_2	S_3		
1.5	17	17	0	- 17	30	0
5	14	14	0	- 14	25	0
10	14	21	0	- 21	36	0
15	20	26	0	- 26	45	0
20	22	38	0	- 38	65	0
25	34	49	0	- 49	85	0
30	51	82	0	- 82	142	0
35	116	138	0	- 138	239	0
37	164	204	0	- 204	354	0
40	283	424	0	- 424	734	0

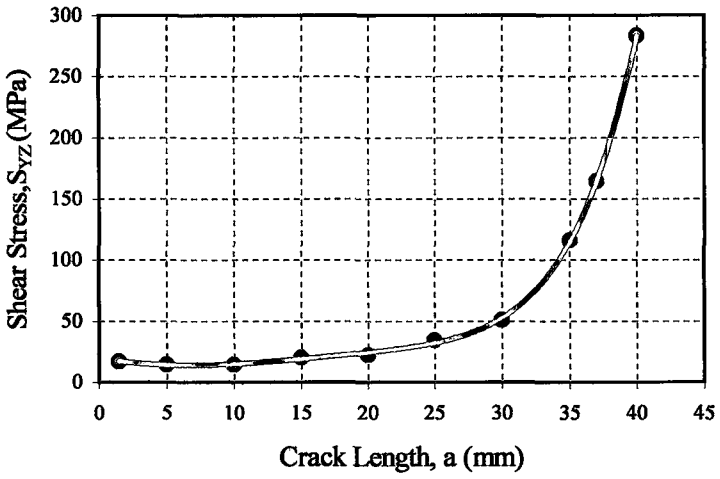

Figure 3.14 The variation of shear stresses vs. crack lengths.

CHAPTER FOUR
FATIGUE ANALYSIS

4.1 Fatigue

The discussions in the preceding chapter described the stress behavior of the shaft subjected to a monotonic load. However, most equipment and components such as shafts are subjected to fluctuating loads whose magnitude is well below the fracture load.

Fatigue damage of components subjected to normally elastic stress fluctuations occurs at regions of stress (strain) raisers where the localized stress exceeds the yield stress of material. After a certain number of load fluctuations, the accumulated damage causes the initiation and subsequent propagation of a crack, or cracks, in the plastically damaged regions. This process can and in many cases does cause the fracture of components. So, the more severe the stress concentration, the shorter the time to initiate a fatigue crack.

According to ASTM E 1150, fatigue is stated as " The process of progressive, localized, permanent structural change occurring in a material, subjected to conditions that produce fluctuating stresses and strains at some point or points and that may culminate in cracks or complete fracture after a sufficient number of fluctuations". Fluctuations may occur both in stress and with time (frequency).

Thus, going further from this statement, one can say that, when failure of a moving machine element occurs, it is usually due to so-called fatigue. Fatigue failure occurs because, at some point, repeated stress in a member exceeds the endurance strength (S_e) of the material. In the case of fluctuating (alternating) loading, where the load is

repeated a large number of times, failure occurs as a brittle fracture without any evidence of yielding.

4.2 Mechanism of Fatigue Failure

Fatigue cracks generally start at a notch that may have been introduced in the manufacturing or fabricating process, providing high stress concentration due to cyclic straining around stress concentration.

In fact, there are three stages of fatigue failure, *fatigue-crack- initiation, fatigue-crack-propagation* and *sudden fracture due to unstable crack growth.* The first stage can be of short duration, the second stage involves most of the life the shaft and the third stage is instantaneous.

The number of cycles required to initiate a fatigue crack is the fatigue-crack-initiation life, N_i. The number of cycles required to propagate a fatigue crack to a critical size is called the fatigue-crack-propagation life, N_p. The total fatigue life, N_t is the sum of the initiation and propagation lives, that is,

$$N_t = N_i + N_p \tag{4.1}$$

The total fatigue life can be shown schematically as seen in Fig. 4.1

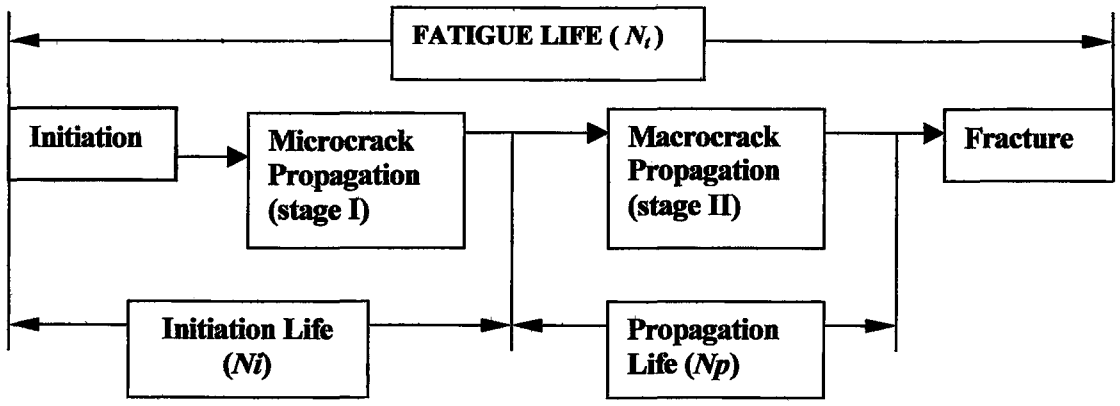

Figure 4.1 The stages of total fatigue life

T.C. YÜKSEKÖĞRETİM KURULU
DOKÜMANTASYON MERKEZİ

However, there is no simple or clear delineation of the boundary between fatigue-crack initiation and propagation. Furthermore, a pre-existing notch (or crack) in a component can reduce or eliminate the fatigue-crack-initiation life and, thus, decrease the total fatigue life of the component.

As stated above, the fatigue life of structural components is determined by the sum of the elapsed cycles required to initiate a fatigue crack and to propagate the crack from subcritical dimensions to the critical size. Consequently, the fatigue life of structural components may be considered to be composed of three continuous stages: 1) fatigue-crack initiation, 2) fatigue-crack propagation and 3) fracture. The fracture stage represents the terminal conditions (i.e., the particular combination of σ, a, and K_{IC}) in the life of structural component. The useful life of cyclically loaded structural components can be determined only when the three stages in the life of the component are evaluated individually and the cyclic behavior in each stage is thoroughly understood.

4.3 Factors Affecting Fatigue Performance

Many parameters affect the fatigue performance of components. They include parameters related to stress (load), geometry and properties of the component, and the external environment. The stress parameters include state of stress, stress range, stress ratio, constant or variable loading, frequency and maximum stress.

The geometry and properties of the component include stress (strain) raisers, size, stress gradient, and metallurgical and mechanical properties of the metal. The external environment parameters include temperature and aggressiveness of the environment.

The primary factor that affects the fatigue behavior of component is the fluctuation in the localized stress or strain. Consequently, the most effective methods for increasing the fatigue life significantly are usually accomplished by decreasing the severity of the stress concentration and the magnitude of the applied nominal stress. In many cases, a decrease in the severity of the stress concentration can be easily accomplished by using transition radii in fillet region.

4.4 Fatigue Loading

Components are subjected to a variety of load (stress) histories. Any loads that vary with time can potentially cause fatigue failure. The character of these loads may vary substantially from one application to another. Hence, variable-amplitude random-sequence load histories like Fig. 2.7 and Fig. 2.8 are very complex functions in which the probability of the same sequence and magnitude of stress ranges recurring during a particular time interval is very small. Such histories lack a describable pattern and cannot be represented by an analytical function.

However, the simplest of these histories is the constant-amplitude cyclic-stress fluctuation. This type of loading usually occurs in machinery parts such as shafts and rods and can be modeled in three different shape as shown in Fig. 4.2, which shows them schematically as sine waves.

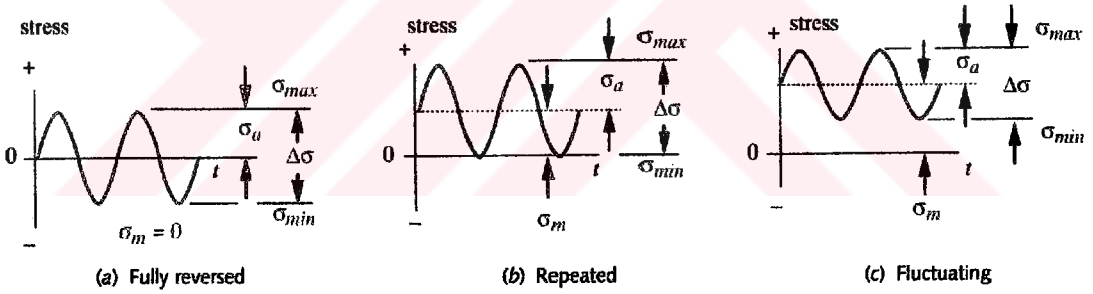

Figure 4.2 Fatigue loading

In this study, the shaft will be assumed experiencing the *fully reversed* case as in Fig.4.2.a for convenience. This assumption is based on the fact that the shaft wobbles equally each side as given in Table 2.4 and 2.5. Thus, constant-amplitude load history can be represented by a constant load (stress) range, $\Delta\sigma$; a mean stress, σ_{mean}; an alternating stress or stress amplitude, σ_a (S_a); and a stress ratio, R.

The **stress range** is the algebraic difference between the maximum stress, σ_{max} and the minimum stress, σ_{min} in the cycle

$$\Delta\sigma = \sigma_{max} - \sigma_{min} \tag{4.2}$$

The **mean stress** is the algebraic mean of σ_{max} and σ_{min} in the cycle

$$\sigma_{mean} = \frac{\sigma_{max} + \sigma_{min}}{2} \tag{4.3}$$

The **alternating stress** or **stress amplitude** is half the stress range in a cycle

$$\sigma_a = S_a = \frac{\Delta\sigma}{2} = \frac{\sigma_{max} - \sigma_{min}}{2} \tag{4.4}$$

The **stress ratio, *R*** represents the relative magnitude of the minimum and maximum stresses in each cycle.

$$R = \frac{\sigma_{min}}{\sigma_{max}} \tag{4.5}$$

When the stress is fully reversed (Fig. 4.2.a), then $R = -1$ and $\sigma_{mean} = 0$. These load patterns may result from bending, torsional, axial or a combination of these types of stresses.

4.5 Fatigue Crack Initiation

Fatigue process is basically a microscopic process. The initiation and progress of fatigue process depends on the microscopic variables: without a clear understanding of which its treatment is extremely difficult. The progressive, localized, permanent structural change, which initiates fatigue failure, is the ''microplasticity '', which, in other words, is the onset of plasticity at microscopic level whilst a material is still nominally elastic (Esin, 1981)

So, the failure usually originates in the formation of a crack at a localized point on the surface imperfections such as notches, scratches. Notches in structural components cause stress intensification in the vicinity of the notch tip. The material element at the tip of a notch in a cyclically loaded structural component is subjected to the maximum stress fluctuations $\Delta\sigma_{max}$. Consequently, this material element is most susceptible to fatigue damage and is, in general, the site of fatigue-crack initiation. For this reason, the notch tip stress or strain is the principal parameter governing the initiation process (Vardar & Kalenderoglu, 1989).

The maximum stress on this material element is given by following equation:

$$\sigma_{max} = k_t \sigma = \frac{2}{\sqrt{\pi}} \frac{K_1}{\sqrt{\rho}} \tag{4.6}$$

and the maximum stress range is:

$$\Delta\sigma_{max} = k_t(\Delta\sigma) = \frac{2}{\sqrt{\pi}} \frac{\Delta K_I}{\sqrt{\rho}} \tag{4.7}$$

where k_t is stress concentration factor for the notch and ρ is the notch tip radius. Although these equations are considered exact only when ρ approaches zero, Wilson and Gabrielse showed, by using finite element analysis of relatively blunt notches in compact-tension specimens, where the notch length a was much larger than ρ, that these relationships are accurate to within 10% for notch radii up to 4.5 mm. (Borsom & Rolfe, 1999).

At this stage, for initial case of 1.5 mm crack length, the notch tip radius can be calculated by using Eq. 4.6. and taking $S_Y = \sigma_{max}$ = 204 MPa, K_I = 3.0489 MPa.m$^{1/2}$ from Table 3.1, thus:

ρ = 2.8e-4 m = **0.28** mm.

Comprehensive understanding of fatigue-crack initiation requires the development of accurate predictions of the localized stress and strain behavior in the vicinity of stress concentrations. Developments in elastic-plastic finite element stress analysis in the vicinity of notches contribute significantly to the development of quantitative predictions of fatigue-crack initiation behavior for structural components.

The effect of a geometrical discontinuity such as notch in a loaded shaft is to intensify the magnitude of the nominal stress in the vicinity of the discontinuity. The localized stresses may cause the metal in that neighborhood to undergo plastic deformation. Because the nominal stresses in the shaft are elastic, an elastic-stress field surrounds the zone of plastically deformed metal in the vicinity of stress concentration. A fatigue crack initiates more readily as the magnitude of the local cyclic-plastic deformation increases. That is, when the material in the vicinity of the notch tip is subject to stress ranges approximately equal to or larger than the yield strength of the material; the plastic deformation causes the material to deform along *slip planes* that coincide with maximum shear stress – about 45° to 60° from the direction of the tensile stress, which results in slip steps on the surfaces of the notch. These slip steps act as new stress raisers that become the nucleation sites for fatigue cracks which initiate along the maximum shear planes and propagate normal to the maximum tensile stress component.

4.6 Fatigue Crack Propagation

Once a microcrack is established, the mechanisms of fracture mechanics become operable. The sharp crack creates stress concentrations same as, may be, as propagate, larger than those of the original notch and a plastic zone develops at the crack tip each time the tensile stress open the crack, blunting its tip and reducing the effective stress concentration. The crack grows a small amount. When the stress cycles to a compressive regime, the crack closes, the yielding momentarily ceases and the crack again becomes sharp but now at its longer dimension. Thus, crack tip moves ahead during each cycle into relatively virgin material in terms of plastic deformation.

This process continues as long as the local stress is cycling from below the tensile yield to above the tensile yield at the crack tip. Thus, *crack growth is due to tensile*

stress and the crack grows along planes normal to the maximum tensile stress. It is for this reason that fatigue failures are considered to be due to tensile stress even though shear stress starts the process in ductile materials as described in sections 2.1.2 and 4.5. Cyclic stress that is compressive will not cause crack growth, as they tend to close the crack. The crack-propagation growth rate is very small, on the order of 2.54e-7 to 2.54e-3 mm per cycle, but this adds up over a large number of cycles.

The log of the rate of crack growth as a function of cycles *da/dN* is calculated and plotted versus the log of the stress intensity factor range ΔK as shown in Fig. 4.3. This fatigue-crack-propagation behavior can be divided into three regions labeled I, II and III. Region I correspond to the crack initiation stage, region II to the crack-growth (crack-propagation) stage and region III to unstable fracture.

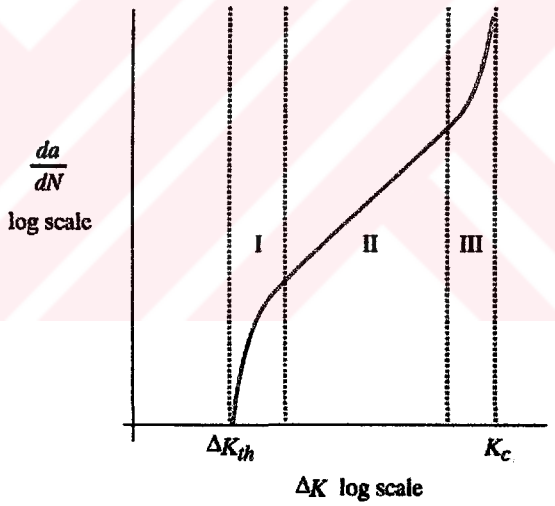

Figure 4.3 Crack grow rate vs. ΔK

The behavior in Region I exhibit a *fatigue-threshold* cyclic stress intensity factor fluctuation, ΔK_{th}, below which cracks do not propagate under cyclic stress fluctuations. The existence of such a threshold was predicted by an elastic-plastic analysis conducted by McClintock. It was shown that the fatigue-crack-propagation threshold could be established in the context of linear elastic fracture mechanics and that a threshold stress intensity factor range, ΔK_{th}, can be determined below which, as stated above, fatigue

cracks do not propagate. Sufficient data are available to show the existence of a fatigue-crack-propagation threshold. Fig. 4.4 presents data published by various investigators on fatigue-crack-propagation values for steels. The graph shows that the value of ΔK_{th} of 18/8 austenitic stainless steel (AISI 304 SS) for $R < 0.1$ is a constant equal to 6 MPa.m$^{1/2}$.

As known, for initial case in which a = 1.5 mm, K_I had been found as 3.0489 MPa · m$^{1/2}$. This means that ΔK = 6.0978 MPa · m$^{1/2}$ and so, crack is more likely to propagate.

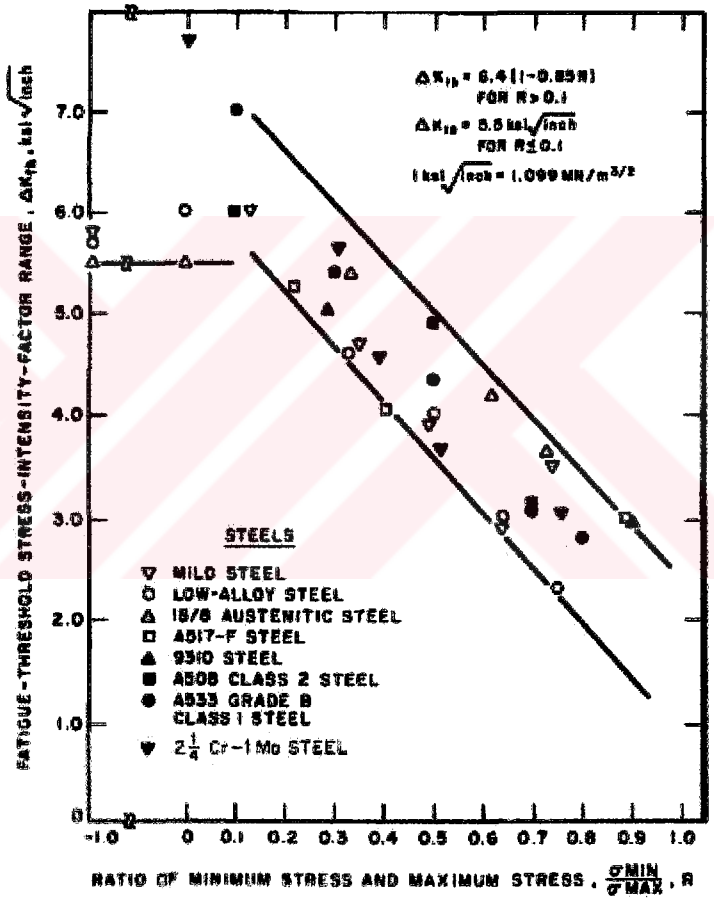

Figure 4.4 Fatigue threshold stress intensity factor range vs. *R*

Region II is of interest in predicting fatigue life and that part of the curve is a straight line on log coordinates. In this region the fatigue-crack-propagation behavior can be represented by following equation, which was defined by Paris.

$$\frac{da}{dN} = A(\Delta K)^m \tag{4.8}$$

where ΔK is the stress intensity factor range and can be calculated for each fluctuating-stress condition from

$$\Delta K = K_{max} - K_{min} = (1-R)K_{max} : \text{ if } K_{min} \langle 0 \text{ then } \quad \Delta K = K_{max} \tag{4.9.a}$$

or

$$\Delta K = \beta\sigma_{max}\sqrt{\pi a} - \beta\sigma_{min}\sqrt{\pi a}$$
$$\Delta K = \beta\sqrt{\pi a}(\sigma_{max} - \sigma_{min}) \tag{4.9.b}$$

A and exponent m are constants and given for austenitic stainless steels, A= 5.60e-12, m = 3.25. Thus, conservative and realistic estimates of fatigue-crack-propagation rates for austenitic steels can be obtained from:

$$\frac{da}{dN} = 5.60e-12(\Delta K_I)^{3.25} \tag{4.10}$$

So, the fatigue-crack-propagation life is found by integrating Eq. 4.10 between a known or assumed initial crack length and a maximum acceptable final crack length based on the particular load, geometry and material parameters for the application.

However, because the fluctuation of the stress intensity factor is the primary fatigue-crack-propagation force, it can be guessed that the rate of fatigue-crack-propagation in the vicinity of a stress riser, such as a notch, would be governed by local stress intensity factor fluctuation. Now, let us calculate the total life, step by step, by assuming an increment of crack growth, Δa up to the critical crack length, a_{cr}. In this case assume that for initial step Δa = 3.5 mm, for intermediate steps Δa = 5 mm, and for last step Δa = 2 mm.

Let's determine the expression for ΔK_I for each crack increments as given below.

$$\Delta K_1 = \beta\Delta\sigma\sqrt{\pi}\sqrt{a} \tag{4.11}$$

Recalling Eq. 3.8 and 3.9, parameter β can be calculated for each crack length and tabulated as in Table 4.1. A graph of the data in Table 4.1 was also plotted to show the variation of parameter β versus crack lengths as shown in Fig. 4.5.

$$\beta = (\frac{D}{d} + \frac{1}{2} + \frac{3d}{8D} - 0.36\frac{d^2}{D^2} + 0.73\frac{d^3}{D^3}) * \frac{1}{2} * \sqrt{\frac{D}{d}}$$

where D is outer diameter of the shaft, d is crack tip diameter.

Table 4.1 Parameter β values vs. crack lengths

Crack Length, a (mm)	D (mm)	d (mm)	β
1.5	99	96	1.1282
5	99	89	1.1543
10	99	79	1.2280
15	99	69	1.3585
20	99	59	1.5726
25	99	49	1.9234
30	99	39	2.5292
35	99	29	3.7055
37	99	25	4.5207

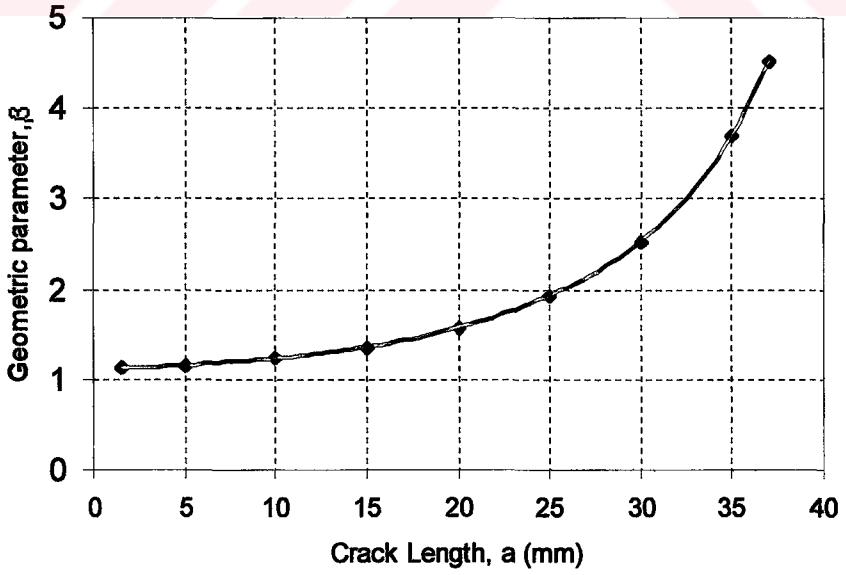

Figure 4.5 The variation of β versus crack lengths.

Again, recalling Eq. 4.2, $\Delta\sigma$ can be calculated for nominal fluctuating stresses.

$\Delta\sigma = \sigma_{max} - \sigma_{min}$ where $\sigma_{max} = 29.07$ MPa, $\sigma_{min} = -29.07$ MPa

$\Delta\sigma = 58.14$ MPa

Substituting β values and $\Delta\sigma$ = 58.14 MPa into Eq. 4.10 and 4.11, N cycle for each increment of crack growth is determined.

$$\frac{da}{dN} = 5.60e-12(\beta\Delta\sigma\sqrt{\pi}\sqrt{a})^{3.25}$$
$$= 5.60e-12(\beta\Delta\sigma\sqrt{\pi})^{3.25} a^{3.25/2} \quad (4.12)$$

Solving Eq. 4.12 for dN gives

$$\int_0^N dN = \left[\frac{1}{5.60e-12}\right]\left[\frac{1}{\beta\Delta\sigma\pi^{1/2}}\right]^{3.25} \int_{a_i}^{a_i+\Delta a} \frac{da}{a^{3.25/2}} \quad (4.13)$$

Taking integral of Eq. 4.13 for initial step results in

N = **1641832** cycles

The results yielded by repeated calculations for other crack increments are shown in Table 4.2, which contains also total fatigue life to propagate a crack from 1.5 to 37 mm. However, it should be noted that, in calculations by using Eq. 4.13, for each crack increment, mean β values given in Table 4.2 have been used to make more realistic prediction.

T.C. YÜKSEKÖĞRETİM KURULU
DOKÜMANTASYON MERKEZİ

Table 4.2 Cycles corresponding crack increments

ai (mm)	Δa (mm)	*ai*+ Δa (mm)	*Mean* β	*N, cycles*	ΣN, *cycles*
1.5	3.5	5	1.1412	1641832	1641832
5	5	10	1.1911	446968	2088800
10	5	15	1.2932	141248	2230048
15	5	20	1.4655	53673	2283721
20	5	25	1.7480	20064	2303785
25	5	30	2.2263	6526	2310311
30	5	35	3.1173	1673	2311984
35	2	37	4.1131	229	**2315330**

Note that, from Table 4.2, the total life to propagate a crack form 1.5 to 37 mm is 2315330 cycles. Since, in normal operation, the agitator runs 24 hours per day. Referring to Fig. 2.7, 2.8 and Table 2.3, 2.4, if the frequencies of the first peaks are assumed as dominant frequencies to which the shaft wobble follow, then, 45 cpm can be taken as a mean frequency at which the shaft wobbles. Thus, 45 cpm x 60 min x 24 h gives 64800 cycles per day and the total life of 2315330 cycles divided by 64800 results in 36 days to fracture the shaft. In addition, it is clear from Table 4.2 that most of the life is taken up in the early stages of crack propagation.

4.7 Fracture

As stated above, the crack continues to grow from 1.5 to 37 mm as long as cyclical tensile stress is present. At the points in the vicinity of final fracture zone, the crack size becomes large enough to raise the stress intensity factor K at crack tip to the level of the material's fracture toughness K_C and sudden failure occurs instantaneously on the next tensile stress-cycle.

4.8 Creating Estimated S-N Diagram

4.8.1 Estimating the Theoretical Endurance Limit, *Se'*

Since the shaft does fail by fatigue, it is logical to base its life on its endurance strength, rather than on its yield or ultimate strength. If published data, which may be obtained from fully reversed bending tests on small, polished specimens are available for the endurance limit of the material, they should be used for estimated S-N diagram. If no data are available, an approximate endurance limit can be crudely estimated from the published ultimate tensile strength of the material.

It should be noted that, the endurance strength (or fatigue strength) S_e falls steadily and linearly (on log-log coordinates) as a function of N until reaching a knee at about 10^6 to 10^7 cycles. This knee defines an endurance limit S_e for the material that is a stress level below which it can be cycled infinitely without failure. The term endurance limit is used only to represent the infinite-life strength for those materials having one.

An approximate endurance limit can be defined as follows for low and intermediate strength steels:

$$Se' \cong 0.5\sigma_{ut} \qquad \text{for} \quad \sigma_{ut} < 1400 \text{ MPa} \tag{4.14}$$

In this case, the theoretical endurance limit for the shaft material AISI 304 having $\sigma_{ut} = 515$ MPa is estimated as follows:

$$\boldsymbol{Se' = 258\ MPa}$$

4.8.2 Correction Factors to the Theoretical Endurance Limit

The theoretical endurance limit obtained from Eq. 4.14 must be modified to account for physical conditions, operating conditions such as environment and temperature, and manner of loading. These and other factors are incorporated into a set of *strength-*

reduction factors that are then multiplied by the theoretical estimate to obtain a corrected endurance limit (fatigue strength) for the application.

Thus, an equation can be written to give corrected endurance limit (fatigue strength) as follows:

$$Se = k_{load} . k_{size} . k_{surf} . k_{temp} . k_{reliab} . Se' \quad (4.15)$$

Let's now look at briefly what the strength-reduction factors are.

1) Loading Effect

Since the most published fatigue data are for rotating bending tests, a strength-reduction *load factor* k_{load} is defined as

$$\text{Bending:} \quad k_{load} = 1 \quad (4.16)$$

2) Size Effect

The rotating bending specimens are small (about 8 mm in diameter). If the shaft is larger than that dimension, a strength-reduction *size factor* k_{size} needs to be applied to account for the fact that larger shafts fail at lower stresses due to the higher probability of a flaw being present in the larger stressed volume. Shigley and Mitchell presented a simple but fairly conservative expression as follows:

$$\text{For} \quad d \leq 8 \text{ mm:} \qquad k_{size} = 1$$

$$\text{For} \quad 8 \text{ mm} \leq d \leq 250 \text{ mm:} \quad k_{size} = 1.189 * d^{-0.097} \quad (4.17)$$

In this case, with $d = 96$ mm (notch tip diameter):

$$k_{size} = 0.7636$$

3) Surface Effect

The rotating bending specimen is polished to a mirror finish to preclude surface imperfections serving as stress risers. It is usually impractical to provide such an expensive finish on a real shaft. Rougher finishes lower the fatigue strength by the introduction of stress concentration and/or altering the physical properties of the surface layer. Thus, a strength-reduction *surface factor* k_{surf} is needed to account for these differences. Shigley and Mischke suggest using an exponential equation of the form as follows to approximate the surface factor with σ_{ut}.

$$k_{surf} \cong A * (\sigma_{ut})^{b} \tag{4.18}$$

The coefficient A and exponent b for various finishes are determined from data shown in Table 4.3.

Table 4.3 A and b values vs. surface finishes

Surface Finish	A (*MPa*)	b
Ground	1.58	- 0.085
Machined or cold-drawn	4.51	- 0.265
Hot-rolled	57.7	- 0.718
As-forged	272	- 0.995

By means of Eq. 4.17 and Table 4.3, for the machined shaft with σ_{ut} = 515 MPa, taking A = 4.51 and b = - 0.265

k_{surf} = 0.862

4) Temperature Effect

The fracture toughness increases at moderately high temperatures up to about 350°C. Several approximate formulas have been proposed to account for the reduction in endurance limit at moderately high temperatures. A strength-reduction *temperature factor* k_{temp}, which was suggested by Shigley and Mitchell is as follows:

$k_{temp} = 1$ for $T \leq 450^{O}C$:

$k_{temp} = 1 - 0.0058^{*} (T - 450)$ for $450^{O}C \leq T \leq 550^{O}C$ (4.19)

For operating temperature of $216^{O}C$,

$k_{temp} = 1$

5) Reliability

Many of the reported strength data are mean values. There is considerable scatter in multiple tests of the same material under the same test conditions. It is reported that the standard deviations of endurance strengths of steels seldom exceed 8 % of their mean values. Thus, the strength-reduction *reliability factor* k_{reliab} for an assumed 8 % standard deviation are presented in Table 4.4.

Table 4.4 Reliability factors

Reliability	k_{reliab}
50	1.000
90	0.897
99	0.814
99.9	0.753
99.99	0.702
99.999	0.659

The data presented in Table 4.4 reveal that if it is hoped to have 99.999 % probability that the shaft meets or exceeds the assumed strength, and then the endurance limit value should be multiplied by 0.659. In calculation, k_{reliab} = 0.659 value against 99.999 % reliability will be used.

The all strength-reduction factors can now be applied to the uncorrected endurance limit value S_e', using Eq. 4.15, the corrected endurance limit S_e is

S_e = 112 MPa

4.8.3 Estimating S-N Diagram

The estimated S-N diagram can now be drawn for the shaft by accepting as if it were unnotched on log-log axes as shown in Fig. 4.6, which was plotted by using a computer program called TKSolver. This is done so to be able to realize the difference between the S-N diagrams for unnotched and notched shafts. The x- axis runs from $N = 1$ to $N = 10^8$ cycles. In general, the diagram shows two distinct regimes called *low-cycle fatigue* (LCF) regime and *high-cycle fatigue* (HCF) regime. There is no sharp dividing line between the two regimes. Various investigators suggest slightly different divisions ranging from 10^2 to 10^4 cycles. In this study, it will be assumed that $N = 10^3$ cycles is a reasonable approximation of the divide between LCF and HCF. Up to 10^3 cycles, the loading is accepted as static. Based on the number of cycles calculated in preceding section 4.6, the shaft is expected to go through its lifetime in HCF regime. So, the bandwidth of interest is the HCF regime from 10^3 to 10^7 cycles and beyond.

The point at 10^3 cycles is estimated by taking advantage of the fact that completely reversed fatigue strength at this life, called S_m is only a little below the ultimate tensile strength, σ_{ut}. The test data indicate that the following estimate of S_m is reasonable:

For bending: $S_m = 0.9\ \sigma_{ut}$ (4.20)

Note that the reduction factors stated above are not applied to S_m. So, to plot the S-N diagram, the necessary S_m value at 10^3 cycles can be obtained from Eq. 4.20 for $\sigma_{ut} = 515$ MPa.

$S_m = 464$ MPa

Since the shaft material is assumed to exhibits a knee at 10^7 cycles, then the corrected S_e is plotted at $N_e = 10^7$ cycles and a straight line is drawn between S_m and S_e. The curve is continued horizontally beyond that point. The equation of the line from S_m to S_e can be written as

$$S_a = B \cdot N^C \qquad 10^3 \leq N \leq 10^7 \qquad (4.21.a)$$

or

$$\log S_a = \log B + C \log N \tag{4.21.b}$$

where S_n is the fatigue strength at any N and B, C are constants defined by the boundary conditions. For the present case, the y axis intercept is $S_a = S_m$ at $N = N_1 = 10^3$ cycles and $S_a = S_e$ at $N = N_2 = 10^7$ cycles.

By substituting the boundary conditions in Eq. 4.21.b and solving simultaneously for B and C:

$$C = \frac{1}{z}\log\left(\frac{S_m}{S_e}\right) \quad \text{where} \qquad z = \log N_1 - \log N_2 \tag{4.21.c}$$

$$\log B = \log S_m - C \log N_1 = \log S_m - 3C$$

Since, N_1 is always 10^3 cycles, and then its $\log_{10}$ is 3. For the shaft material with a knee at $N_2 = 10^7$,

$$z = \log(1000) - \log(1.e7) = 3 - 7 = -4$$

$$C = \frac{1}{z}\log\left(\frac{S_m}{S_e}\right) = -\frac{1}{4}\log\left(\frac{464}{112}\right) = -0.1543$$

$$B = 10^{(\log S_m - 3C)} = 10^{[\log 464 - 3*(-0.1543)]} = 1347.3889$$

Substituting constants B and C in Eq. 4.21.b, the alternating stress level at the crack tip for the number of cycles of total life can now be found. For the obtained total life of 2315330 cycles, it is

$$S_a = 10^{[\log B + C*\log N]}$$

$$= 10^{[\log(1347.3889) + (-0.1543)*\log(2315330)]}$$

S_a = 140 MPa

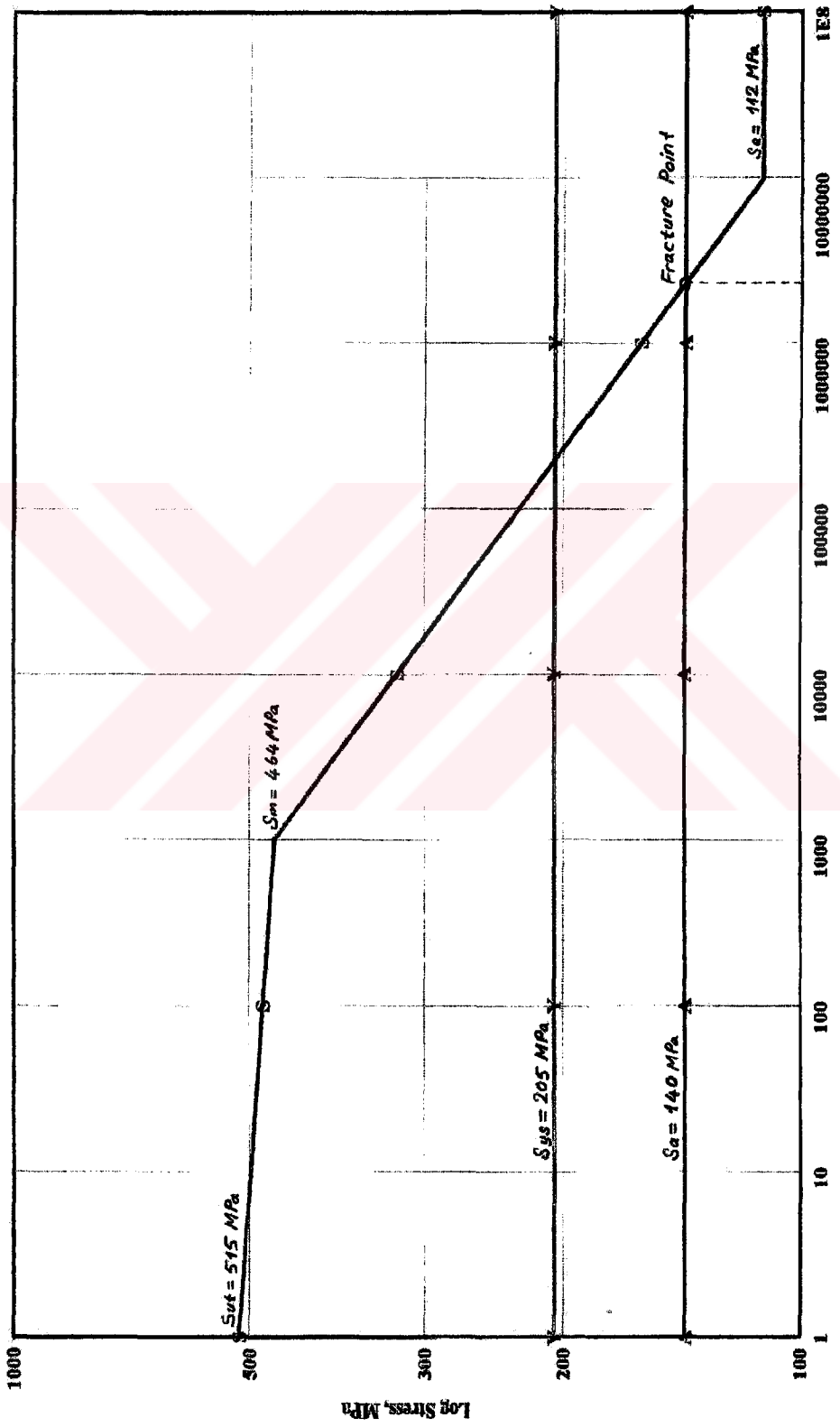

Figure 4.6 S-N diagram for unnotched shaft

As known, the results obtained above have been calculated without accounting the notch effect and the S-N diagram in Fig. 4.6 was drawn according to these results. Now, in view of showing how a notch affects the S-N diagram, the calculations will be performed again accounting fatigue notch factors.

Geometric discontinuities that are unavoidable in design and manufacturing, such as fillets, grooves and scratches, causes the stress to be locally elevated and so, as implied before, are called *stress raisers*, which here termed notches for brevity. Notches require special attention as their presence reduces the resistance of the components to fatigue failure. This is simply a consequence of the locally higher stresses causing fatigue cracks to start at such locations.

Values of the elastic stress concentration factor k_t are used to characterize notches, where $k_t = \sigma / S$ is the ratio of the local notch (point) stress σ to the nominal (average) stress S. Any particular definition of S is arbitrary, as in basing S on net area rather than gross area, and the exact choice made affects the value of k_t. Hence, it is important to be consistent with the definition of S being used when k_t values are given. In the S-N approach, it is conventional to define S in terms of the net area. That is, the area after the notch has been removed. The equality $\sigma = k_t S$ holds at the notch only if there is no yielding. The notch root stress or strain is the principal parameter governing the initiation process. However, the elastic stress at the notch tip, calculated from $\sigma = k_t S$, is usually fictitious since it exceeds the yield strength of the material (Vardar & Kalenderoglu, 1989). For the components where the notch is crack like in shape, fracture mechanics helps to estimate the elastic notch root stress σ through (also see Eq. 4.6 and 4.7)

$$\sigma = \lim_{\rho \to 0} \left\{ 2K / (\pi\rho)^{1/2} \right\} \tag{4.22}$$

with K being the stress intensity factor and ρ the notch root radius.

The *actual reduction factor* at long fatigue lives, specifically at $N = 10^6$ to 10^7 cycles or greater, is called the *fatigue notch factor* and is denoted k_f. If the notch has a large radius ρ at its tip, k_f may essentially equal to k_t. However, for small ρ, the discrepancy

may be quite large, so that k_f is considerably smaller than k_t. More than one physical cause of this behavior may exist. Due to the complexity involved, empirical estimates are generally used to obtain k_f values for use.

The stress at the notch tip decreases rapidly with increasing distance from the notch as illustrated in Fig. 4.7. The slope $d\sigma / dx$ of the stress distribution is called the *stress gradient,* and the magnitude of this quantity is especially large near sharp notches. It is generally agreed that the $k_f < k_t$ effect is associated with this stress gradient.

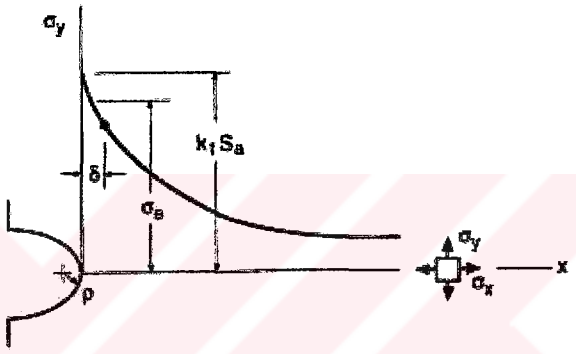

Figure 4.7 Notch tip stresses

One argument based on stress gradient is that the material is not sensitive to the peak stress, but rather to the average stress that acts over a region of small but finite size. In other words, some finite volume of material must be involved for the fatigue damage process to proceed. The size of active region can be characterized by a dimension δ, called the process zone size, as illustrated in Fig. 4.7. Thus, the stress that controls the initiation of fatigue damage is not the highest stress at $x = 0$, but rather the somewhat lower value that is the average out to a distance $x = \delta$. This average stress is then expected to be the same as the unnotched smooth shaft fatigue (endurance) limit S_e.

Thus, the fatigue notch factor k_f is estimated by employing the concept of *notch sensitivity q* defined as

$$q = \frac{k_f - 1}{k_t - 1} \tag{4.23}$$

Eq. 4.22 can be rewritten to solve for k_f.

$$k_f = 1 + q(k_t - 1) \tag{4.24}$$

The procedure is to first determine the theoretical stress concentration k_t for the shaft of particular geometry and loading, then establish the appropriate notch sensitivity for AISI 304 and use them in Eq. 4.23 or 4.24 to find the dynamic stress concentration factor k_f. The notch sensitivity q also is defined from the Kunn-Hardrath formula in terms of Neuber's constant β and the notch radius ρ, both expressed in mm.

$$q = \frac{1}{1 + \sqrt{\frac{\beta}{\rho}}} \tag{4.25}$$

where, for β the following empirical equation may be used for steels over the range indicated:

$$\log \beta = -\frac{\sigma_{ut} - 134MPa}{586} \text{ (mm)} \qquad \sigma_{ut} \leq 1520MPa \tag{4.26}$$

Substituting $k_t = 7.575$, $q = 0.528$ for $\beta = 0.2237$ mm for $\sigma_{ut} = 515$ MPa and $\rho = 0.28$ mm in Eq. 4.24, k_f is

k_f= 4.471

One thing to say, the notch sensitivity is dependent on the notch radius. As notch radius approaches zero, the notch sensitivity of materials decreases and also approaches zero.

Since the starting point for the estimate is the ultimate tensile strength, then the fatigue (endurance) limit for a notched shaft, S_{ef} is obtained by applying Eq. 4.15 along with k_f.

$$S_{ef} = \frac{S_e}{k_f} \tag{4.27}$$

Thus, substituting S_e = 112 MPa, k_f = 4.471 into Eq. 4.26, S_{ef} is

S_{ef} = 25 MPa

Finally, in order to plot the S-N diagram, the strength value at 10^3 cycles is needed. Because, the full value of the fatigue notch factor k_f only applies to the high end of the HCF regime (10^6 – 10^9 cycles). At intermediate and short fatigue lives in ductile materials becomes increasingly important. One consequence of this behavior is that the ratio of the unnotched shaft to notched shaft strength about 10^3 cycles becomes less than k_f, so that it is useful to define a *new fatigue notch factor* k_f' that varies with life as shown in Fig. 4.8. To get k_f', an empirical approach rather than analysis as just described for k_f is generally used. Once k_f for long life has been estimated, k_f' at 10^3 cycles can be estimated using curve given in Fig. 4.9.

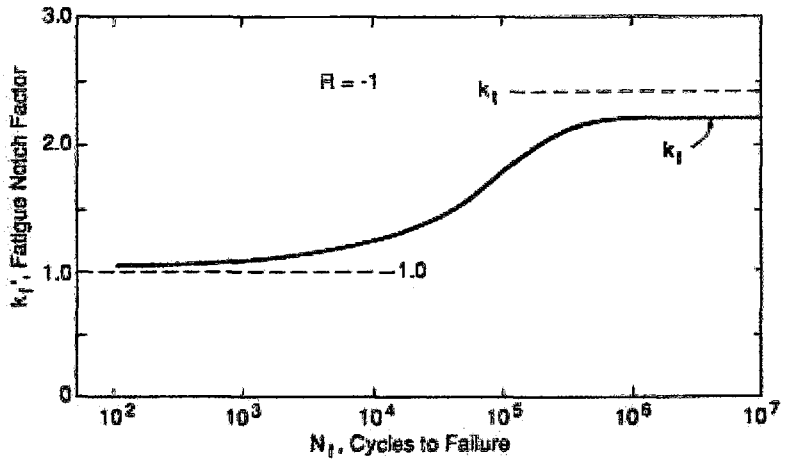

Figure 4.8 Curve showing the variation of fatigue notch factor with time

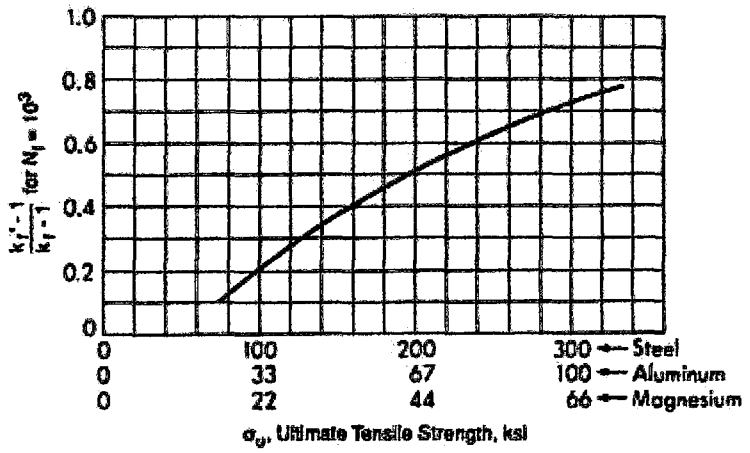

Figure 4.9 Curve for notch sensitivity at 10^3 cycles vs. σ_{ut}

As shown in Fig. 4.9, vertical axis represents a ratio q' called *notch sensitivity at* 10^3 cycles and q' is given as follows:

$$q' = \frac{k_f' - 1}{k_f - 1} \tag{4.28}$$

Eq. 4.27 can be rewritten to give k_f'

$$k_f' = 1 + q'(k_f - 1) \tag{4.29}$$

For σ_{ut} = 515 MPa (75 ksi), from Fig. 4.9, q' = 0.11 obtained, and k_f = 4.471 given.

Substituting them in Eq. 4.29, k_f' is

$$\boldsymbol{k_f' = 1.382}$$

Thus, the strength at 10^3, S_m' is obtained by applying Eq. 4.20 along with k_f'.

$$S_m' = \frac{S_m}{k_f'} \tag{4.30}$$

Substituting S_m = 464 MPa and k_f' = 1.382 in Eq. 4.30, S_m' is

S_m' = 335 MPa

After this step, the S-N diagram for notched shaft on log-log coordinates can be drawn using above calculated strength values of S_m' and S_{ef}. Related S-N diagram is plotted as shown in Fig. 4.10 by employing TKSolver computer program.

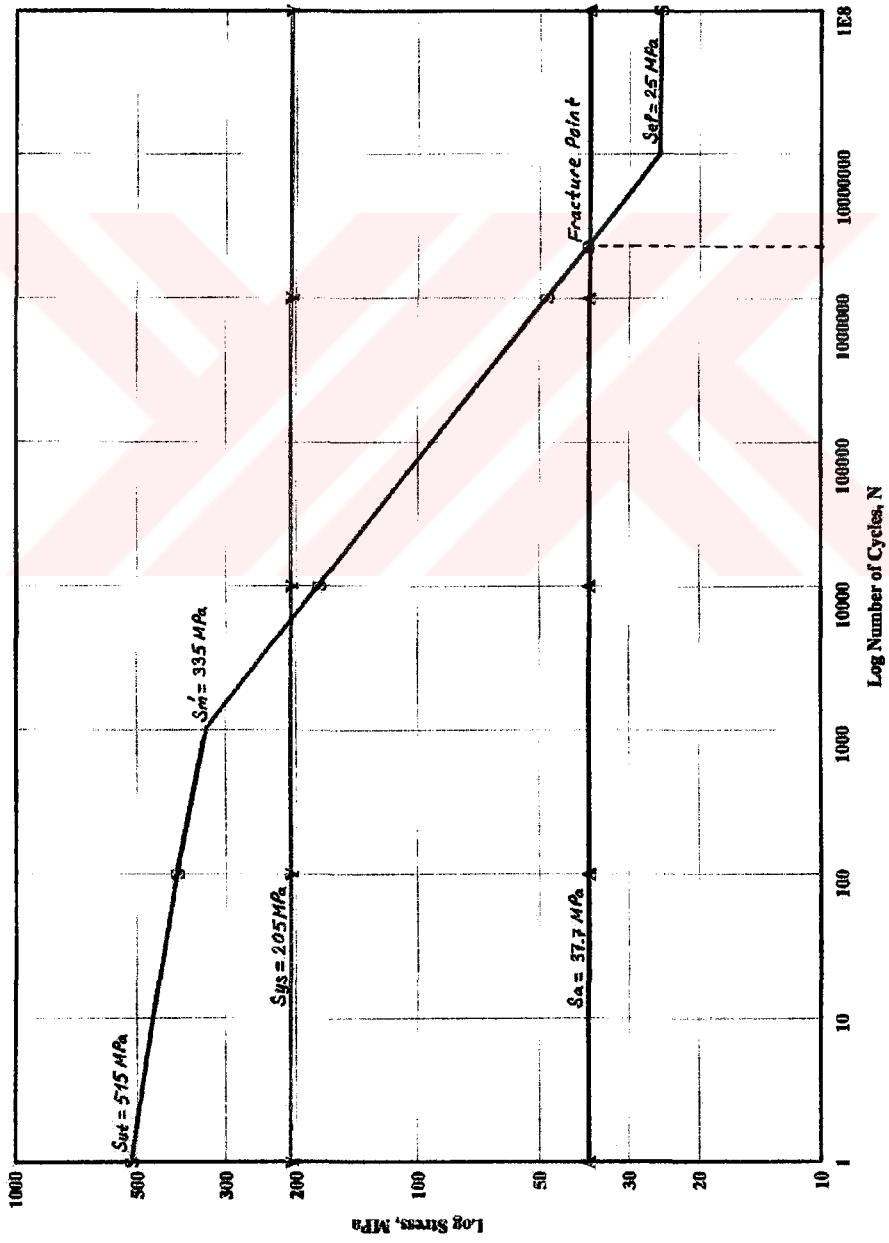

Figure 4.10 S-N diagram for notched shaft

The alternating stress, S_a for the notched shaft at the calculated total fatigue life of 2315330 cycles is obtained by applying Eq. 4.21 a,b,c with S_m' and S_{ef}. Here, in order not to repeat the same calculations, the result will only be given.

S_a = 37.7 MPa

As seen from the results, endurance limit, S_e and relatively alternating stress, S_a at the calculated total life for unnotched shaft decrease rapidly to lower values due to notch severity.

CHAPTER FIVE
CONCLUSIONS

The studies executed in the scope of both stress and fatigue analyses of the agitator shaft have revealed the followings.

1- Stress analyses performed by both analytical and Ansys program show that the tensile stress at the notch tip passes over the yield strength of the shaft material. This indicates that a fatigue crack-initiation is more likely to happen at the notch tip. However the torsional stress is well below the shear strength ($\tau_{ys} = 0.5\sigma_{ys}$) of the shaft material. So, the torsional stress does not contribute to the yielding of the material. The only effect of the tork is to change over the direction of the bending stresses from tension to compression at each cycle.

2- Fatigue failure is a tensile stress phenomenon. The elevated tensile stress due to the notch effect creates resolved shear stress. Slip in the crystals occurs when the resolved shear stress attains a critical value, which is characteristic of the material. Thus, the plastic flow resulting in crack-initiation commences at the notch tip.

3- Since the tensile stress due to shaft bending is a predominant factor affecting the crack-initiation and crack-propagation. The wobble of the shaft, which causes bending should be, if possible, prevented by application of an in-tank bearing at the bottom end of the shaft, which keeps the shaft in its vertical axis.

4- Since the present curves and formulations given in literature are for the particular cases such as o-ring groove, fillet, stepped shaft, ...etc., they are not adequate to obtain those for real cases. To overcome this difficulty, Ansys modeling feature has been used, and the results obtained for k_t and k_{ts} are seen reasonable for calculations.

5- Although the nominal stresses in the shaft are well below the yield strength, the elevated stresses at the notch tip, as stated above, may attain the yield strength due to notch severity. For this reason, the making of the shaft should be done with great care and all unwanted irregularities such as cracks, notches, scratches, cavities, …etc. should never be allowed to occur during manufacturing. Also, as seen from fatigue analysis, presence of a notch shortens the useful life of shaft considerably, relating to lowered endurance limit comparing to that of unnotched shaft.

6- Fracture Toughness, K_{IC} value of shaft material can be estimated from the plot given in Fig. 4.13. If the critical crack length, a_{cr} is assumed to be a value somewhere between 37 and 40 mm, then K_I ranges from 136.57 and 264.74 MPa.m$^{1/2}$. So, a mean K_{IC} value of about 200 – 220 MPa.m$^{1/2}$ can be thought as a reasonable value for shaft material. This value is consistent with that (223 MPa.m$^{1/2}$ for 304 LN) given in (Vardar, 2002).

REFERENCES

Aksoy, T. (1984). Kırılma Mekaniği. İzmir: Dokuz Eylül Ün., MM Fak., Mak. Müh. Böl.

Aksoy, T., & Önel, K. (1990). Malzeme Bilgisi – 1. (3rd ed.). İzmir: Dokuz Eylül Ün., MM Fak., MM/MAK-90 ey 086.

Anderson, T.L. Fracture Mechanics; Fundamentals and Applications. (2nd ed.). CRC Press.

ASM. (1975) Metals Handbook, Failure Analysis and Prevention,10, (8th ed.). American Society for Metals.

ASTM SPT 918. (1986). Case Histories Involving Fatigue & Fracture Mechanics.

Barsom, J.M, & Rolfe, S.T. (1999). Fracture and Fatigue Control in Structures; Application of Fracture Mechanics. (3rd ed.). ASTM, MNL41.

Chemical Engineer's Handbook. (1973). (5th ed.). McGraw-Hill Kogakusha, Ltd.

Courtney, T.H. (2000). Mechanical Behavior of Materials. (2nd ed.). McGraw-Hill Co. Inc.

Ebi, G. (2001, October). Operating deflection shape analysis - a powerful tool to increase plant reliability. Hydrocarbon Processing, 80, 59-63

Erdol, R., Erdogan, F. (1978). A thick-walled cylinder with an axisymmetric internal or edge crack. Journal of Applied Mechanics, 45, 281-286

Esin, A. (1981). Properties of Materials for Mechanical Design. Gaziantep: Metu.

He, M. Y., & Hutchinson, J. W. (2000). Surface crack subject to mixed mode loading. Engineering Fracture Mechanics, 65, 1-14

Hellan, K. (1985). Introduction to Fracture Mechanics. McGraw-Hill Book Co.

Henkel,D., & Pense, A.W. (2002). Structure and Properties of Engineering Materials. (5th ed.). McGraw-Hill Co. Inc.

Lipson,C., & Juvinal, R.C. (1961). Application of stress analysis to design and metallurgy. The University of Michigan, Engineering Summer Conference.

Marin, J. (1966). Mechanical Behavior of Engineering Materials. Prentice-Hall of India (Private) ltd.

McCabe, W. L., & Smith, J. C. (1967). Unit Operations of Chemical Engineering. (2nd ed.). McGraw-Hill Book Co.

Norton, R.L. (1988). Machine Design; An Integrated Approach. Prentice-Hall, Inc.

Osgood, C. C. Fatigue Design. Wiley-Interscience

Perl, M., & Greenberg, Y. (1998). Three-dimensional analysis of thermal shock effect on inner semi-elliptical surface cracks in a cylindrical pressure vessel. International Journal of Fracture, 99, 161-170

Rolfe, S.T., & Barsom, J.M. (1977). Fracture and Fatigue Control in Structures; Application of Fracture Mechanics. Prentice-Hall Inc.

Smith, C.O. (1969). The Science of Engineering Materials. Prentice-Hall, Inc.

Uguz, A. (1996). Kırılma Mekaniğine Giriş. Bursa: Uludağ Ün. Basımevi.

Unger, D. J. (2001). Analytical Fracture Mechanics. Dover Pub. Inc.

Vardar, Ö. (1982). Fatigue crack propagation beyond general yielding. Journal of Engineering Materials and Technology, 104, 192-199

Vardar, Ö. (1988). Fracture Mechanics. BU Publication, No: 453.

Vardar, Ö., & Kalenderoğlu, V. (1989). Effect of notch root radius on fatigue crack initiation. Materials Science and Engineering, A114, L35-L38

Vardar, Ö. (2002, April 02). (Personal e-mail message).

Young, W.C., & Budynas, R.G. (2002). Roark's Formulas for Stress and Strain. (7^{nt} ed.). McGraw-Hill Co. Inc.

APPENDIX A

IMAGES OF THE FRACTURE SURFACE

Figure A1 View of the fracture surface (upper side)

Figure A2 View of the fracture surface (lower side)

Figure A3 Final fracture zone

Figure A4 Fibrous zone and beachmarks

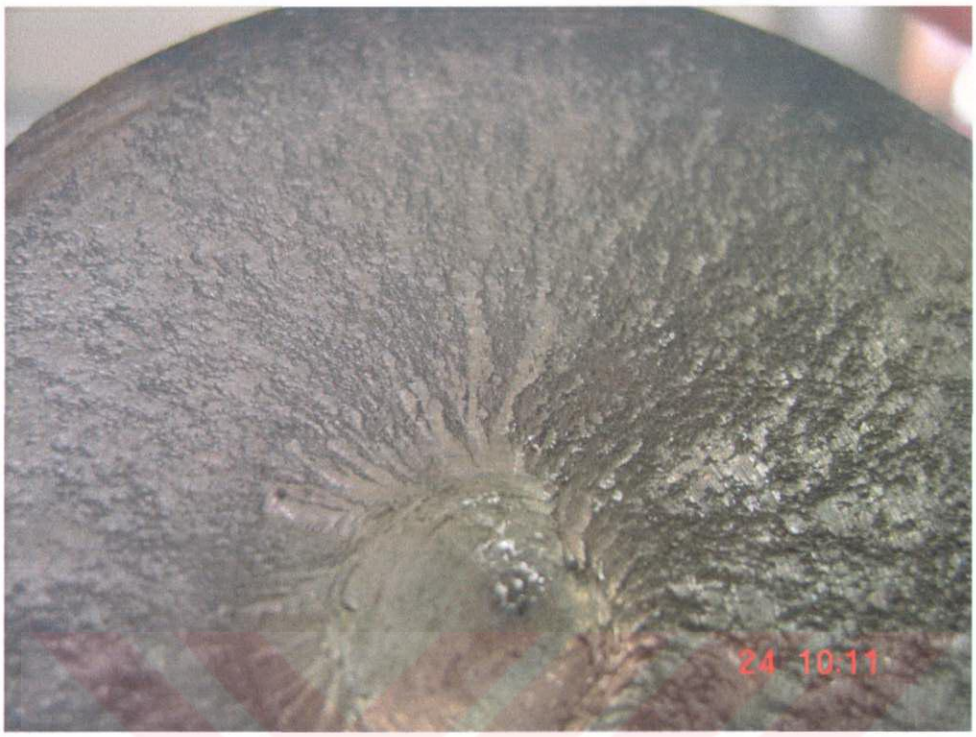

Figure A5 Radial zones and final fracture zone

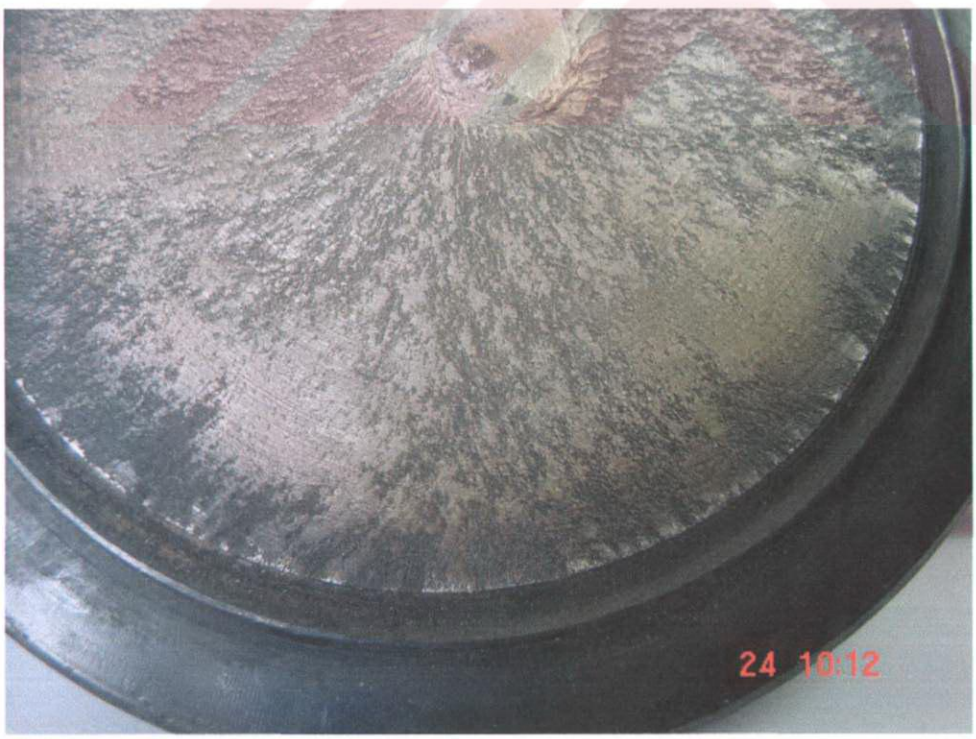

Figure A6 Fibrous zones and radial zones

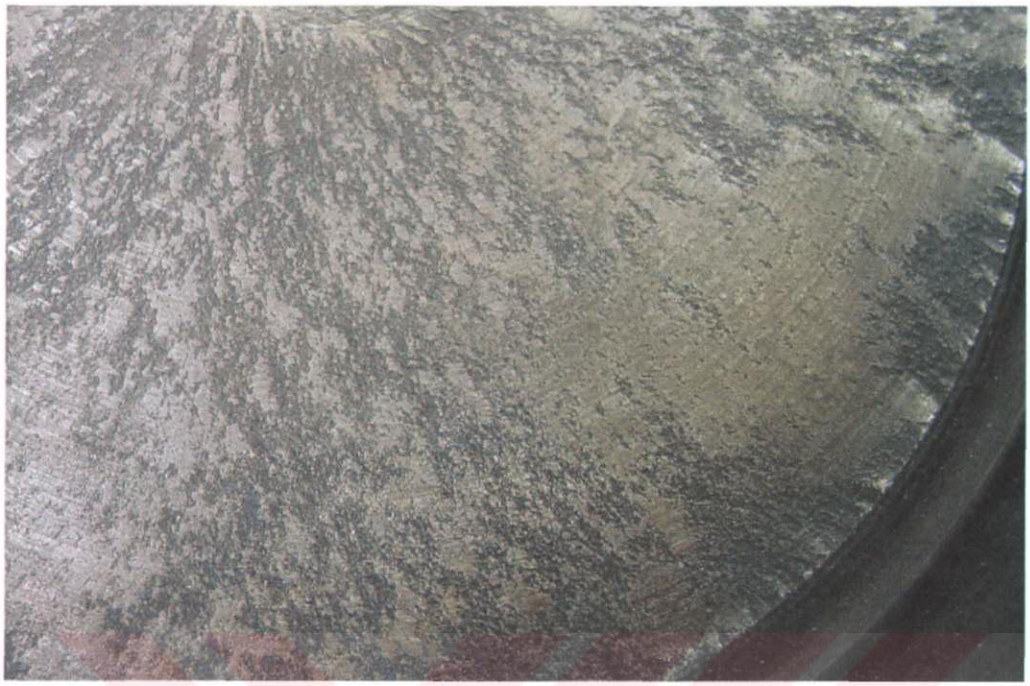

Figure A7 Radial zones showing crack advance direction

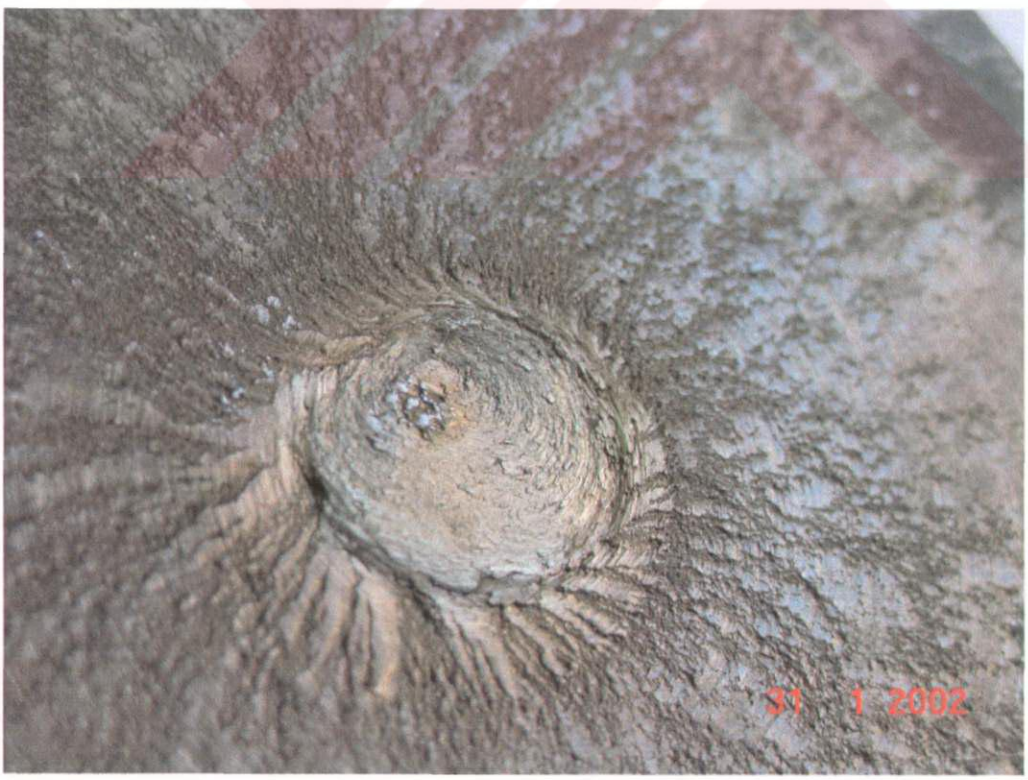

Figure A8 Final fracture zone

Figure A9 Final fracture zone with shear lips

Figure A10 Beachmarks

APPENDIX B

NOTCH TIP ELEMENTS AND MESH GENERATION

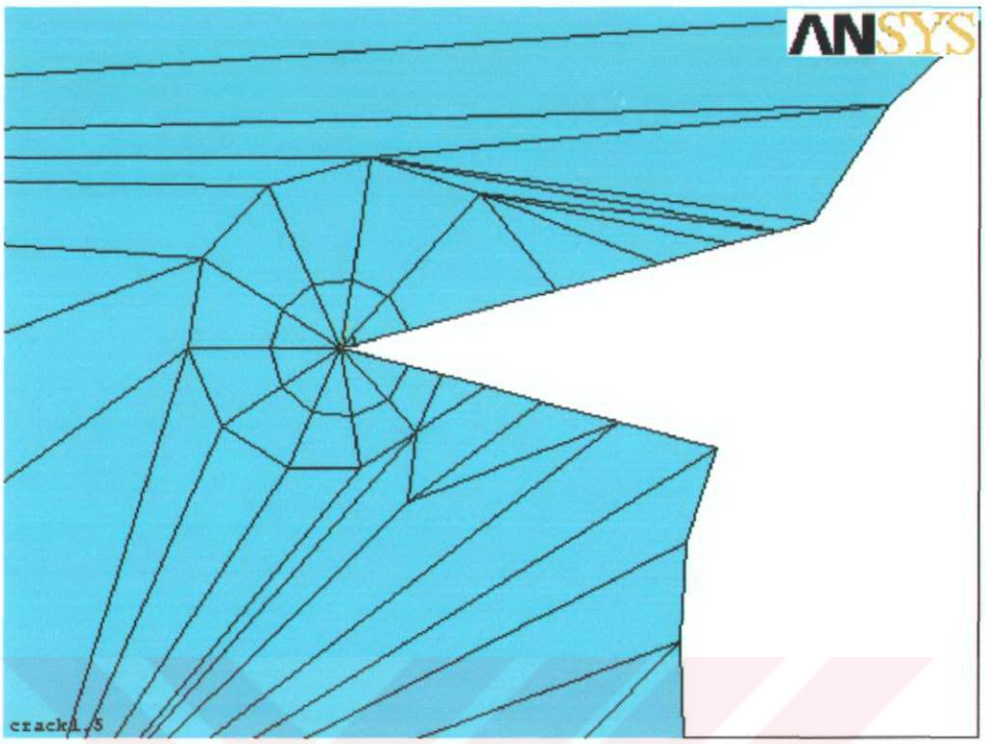

Figure B1 Notch (crack) with length of 1.5 mm.

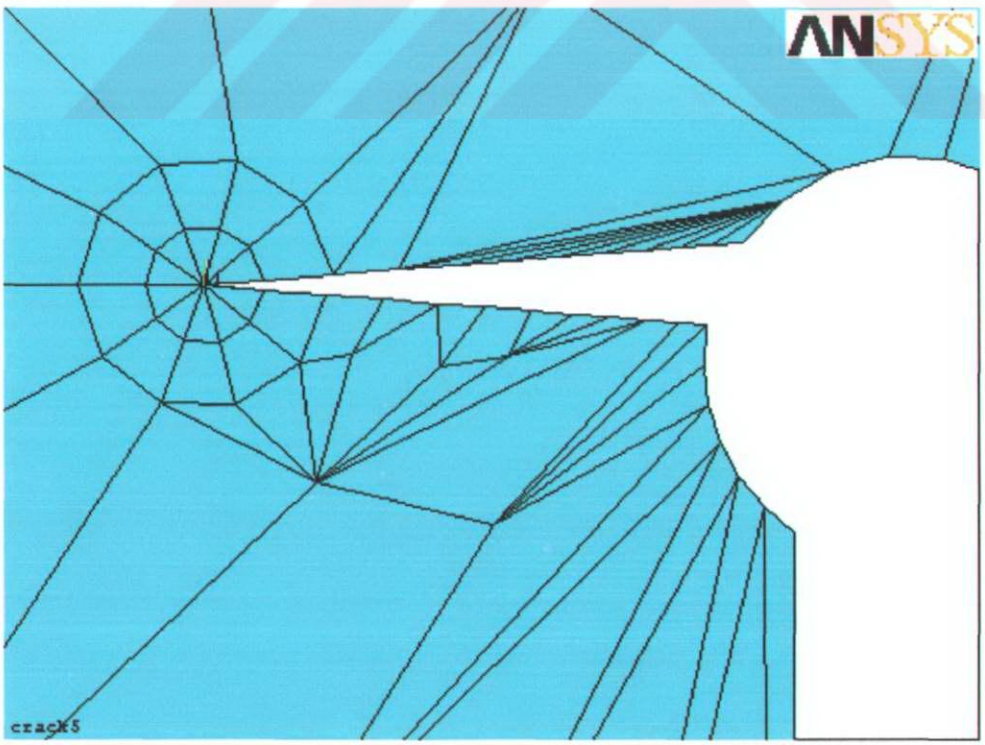

Figure B2 Crack with length of 5 mm.

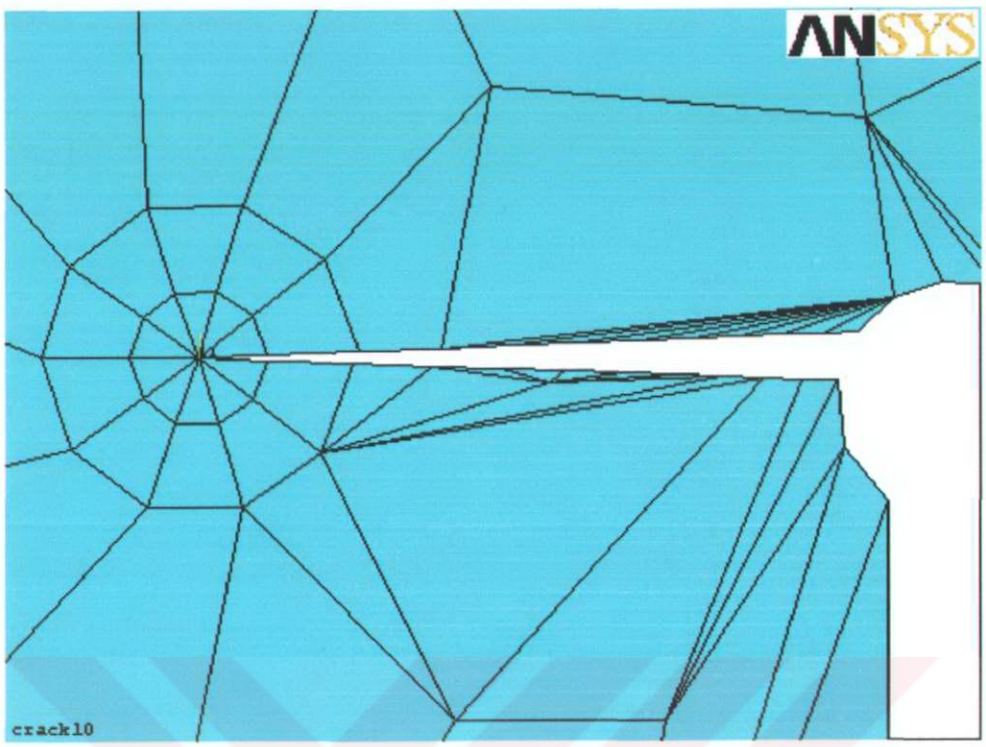

Figure B3 Crack with length of 10 mm.

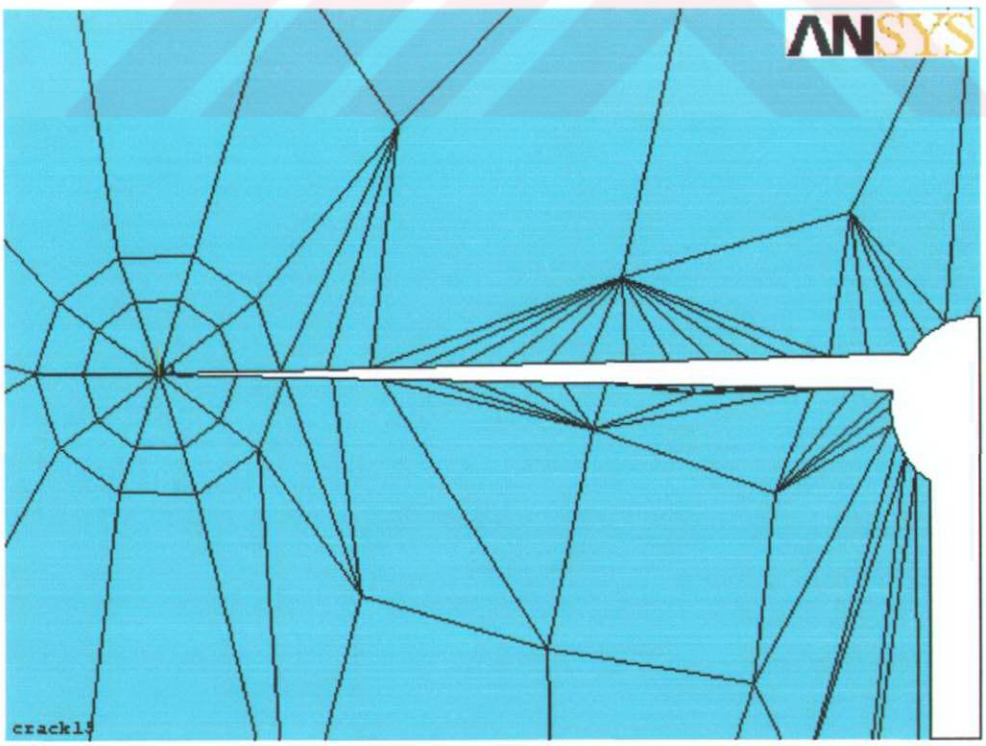

Figure B4 Crack with length of 15 mm.

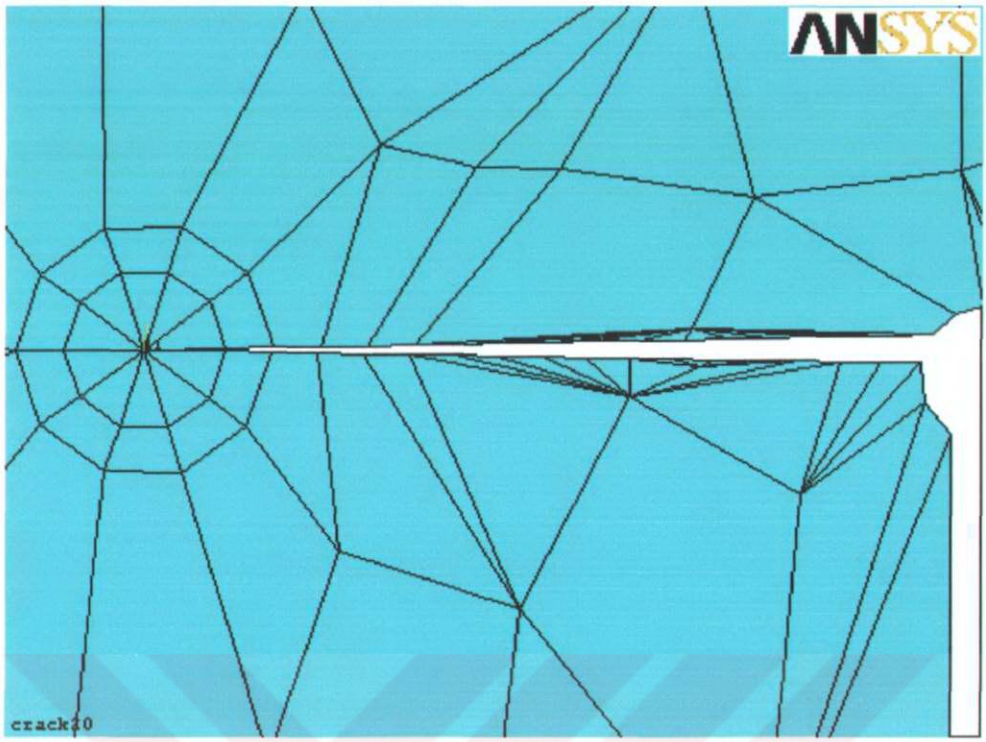

Figure B5 Crack with length of 20 mm.

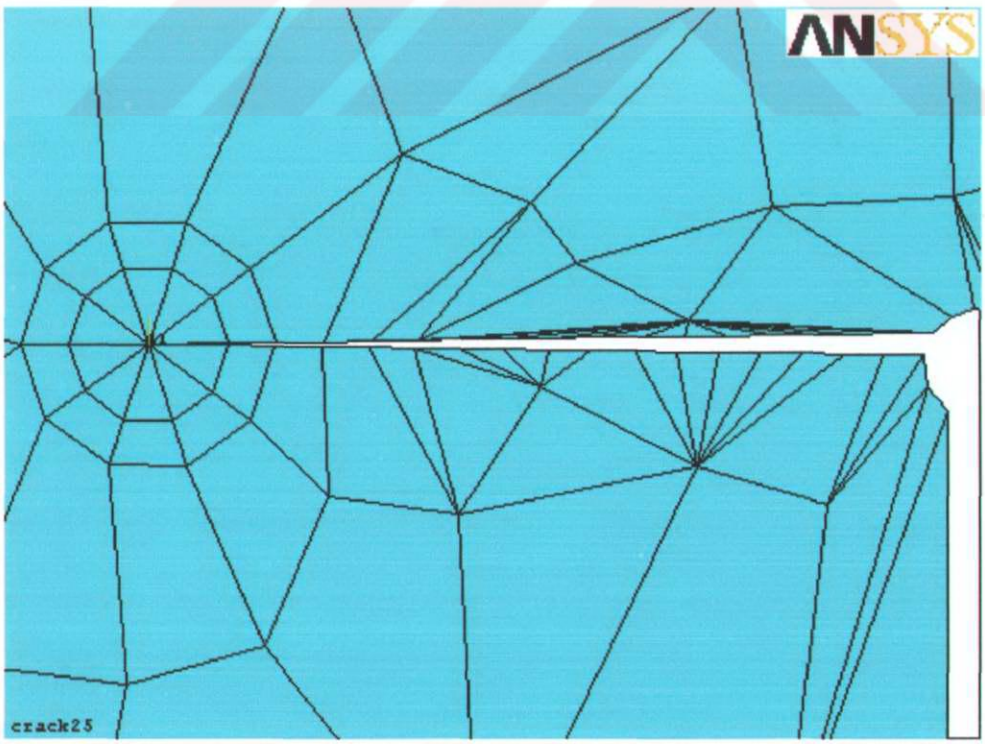

Figure B6 Crack with length of 25 mm.

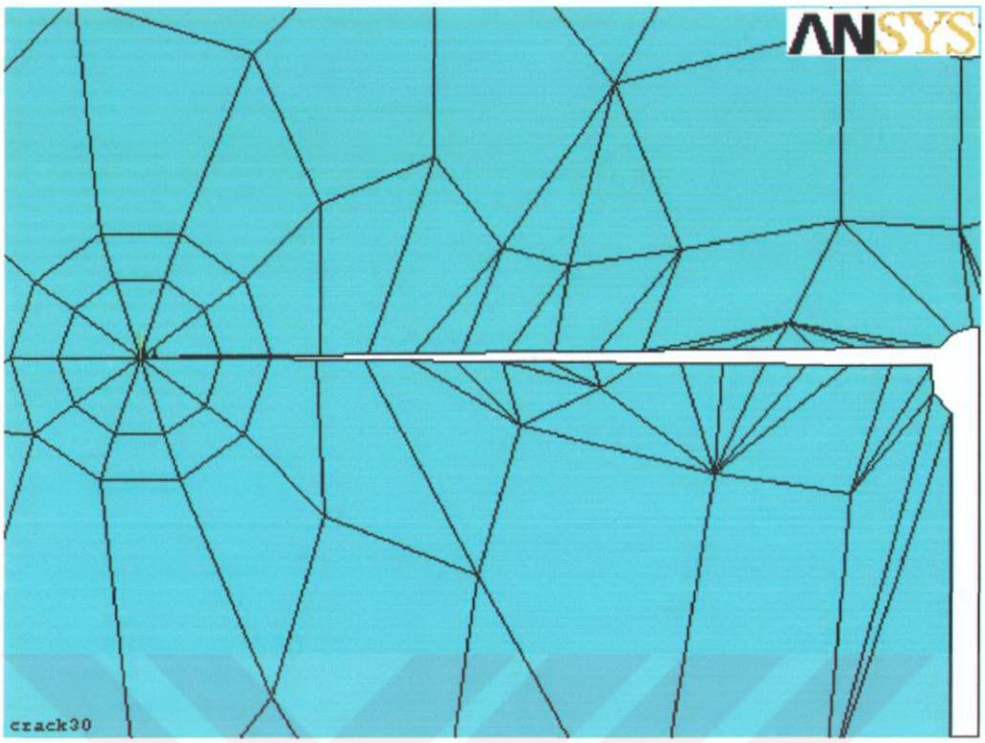

Figure B7 Crack with length of 30 mm.

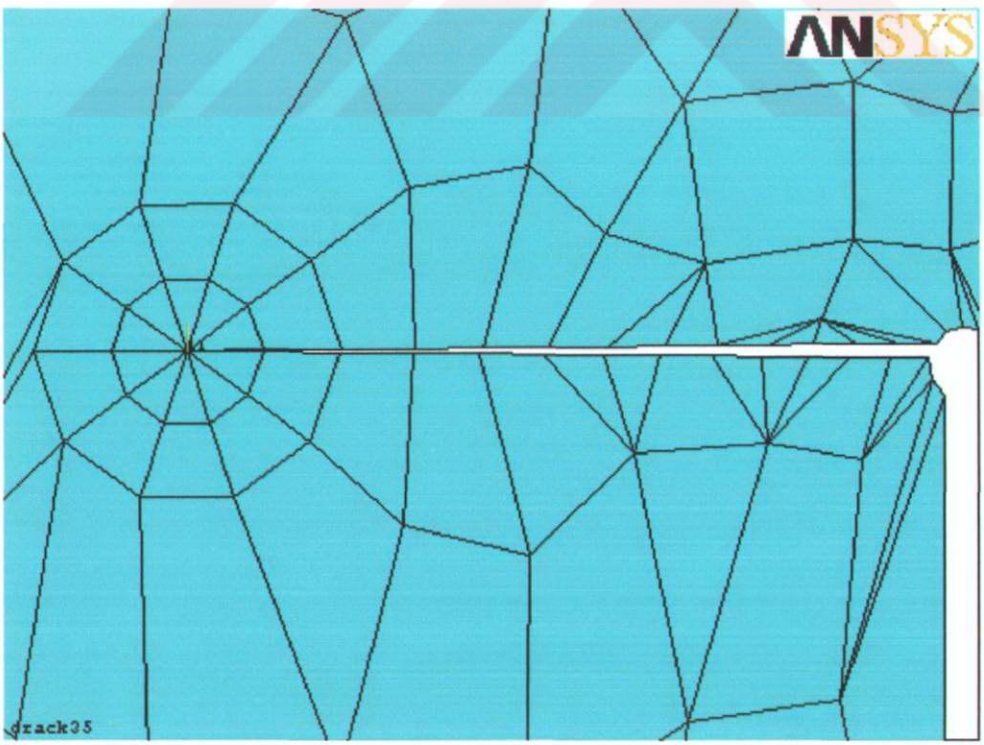

Figure B8 Crack with length of 35 mm.

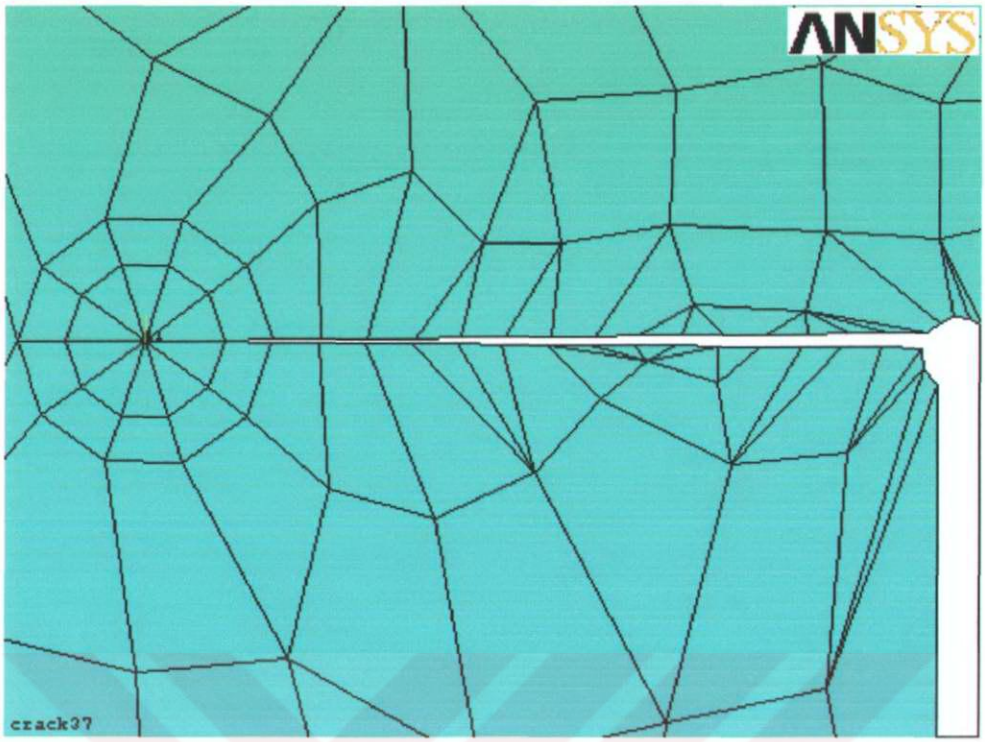

Figure B9 Crack with length of 37 mm.

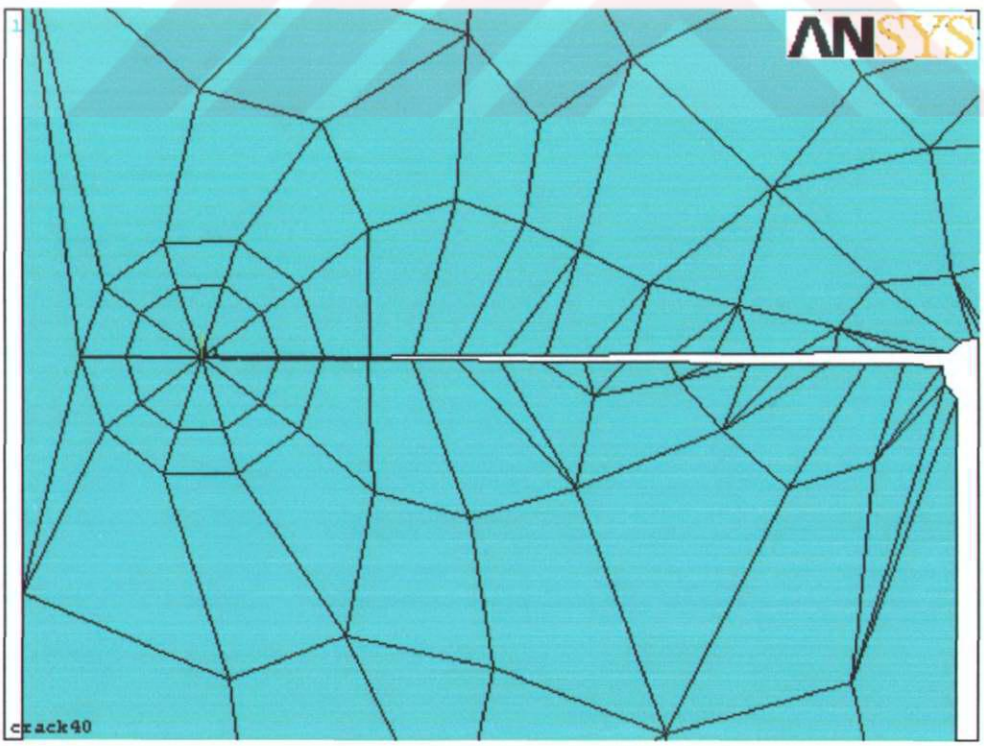

Figure B10 Crack with length of 40 mm.

APPENDIX C

CRACK TIP STRESS DISTRIBUTIONS

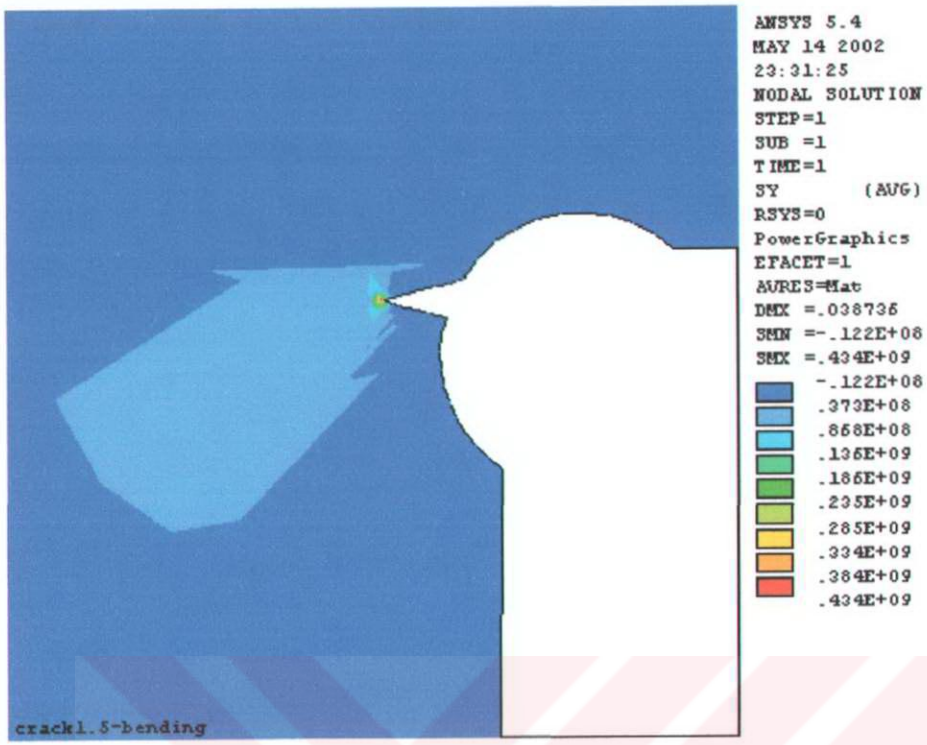

Figure C1 Stress distribution due to bending at the tip of notch (crack) of a = 1.5 mm.

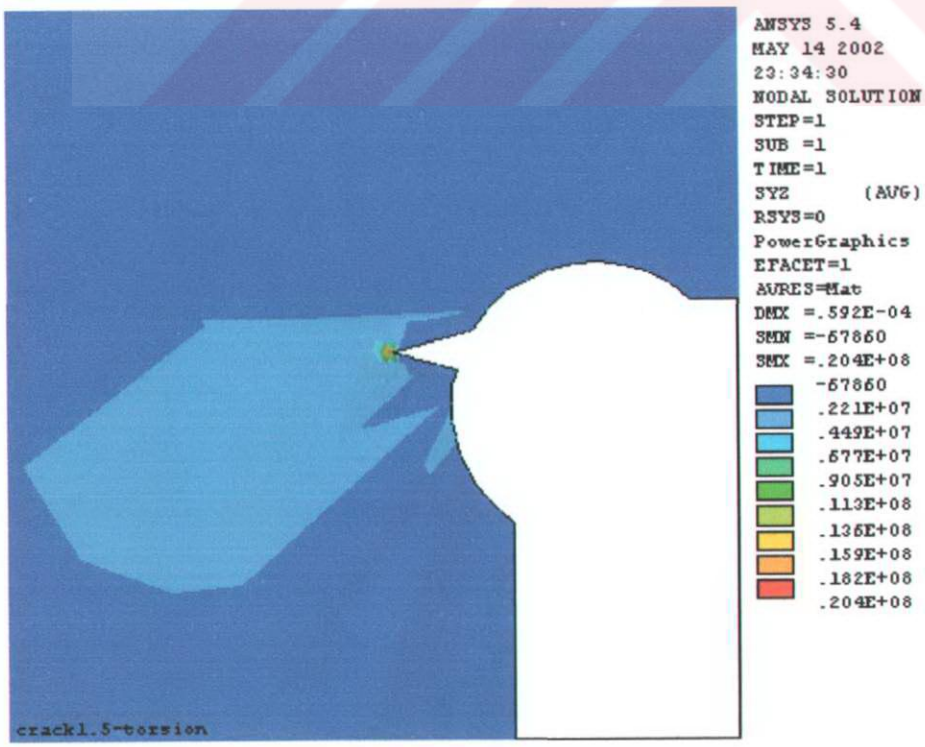

Figure C2 Stress distribution due to torsion at the tip of notch (crack) of a = 1.5 mm.

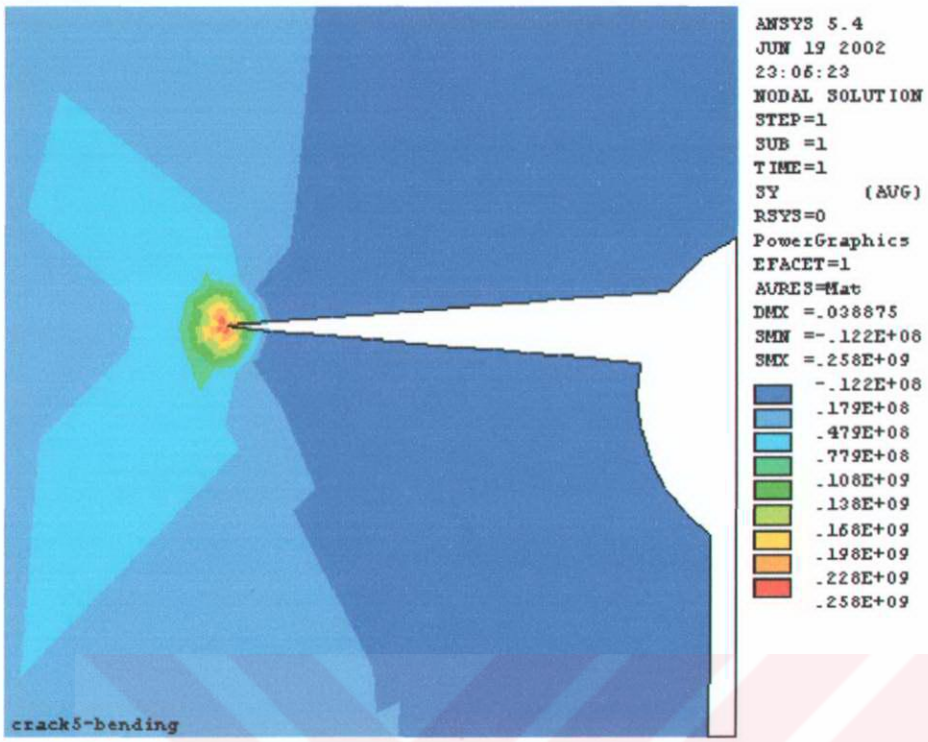

Figure C3 Stress distribution due to bending at the tip of crack of $a = 5$ mm.

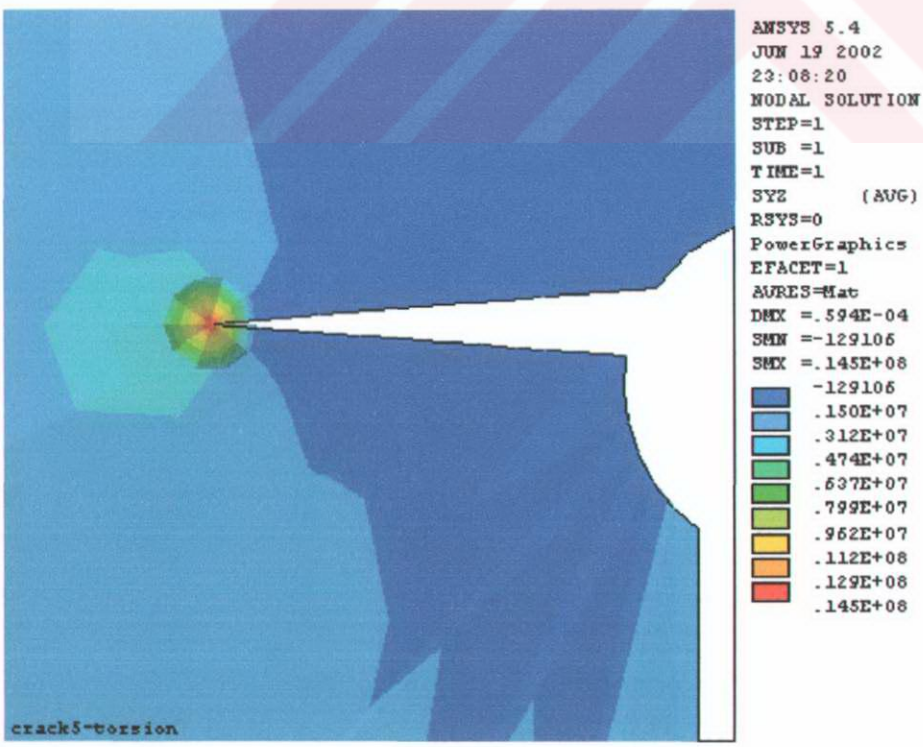

Figure C4 Stress distribution due to torsion at the tip of crack of $a = 5$ mm.

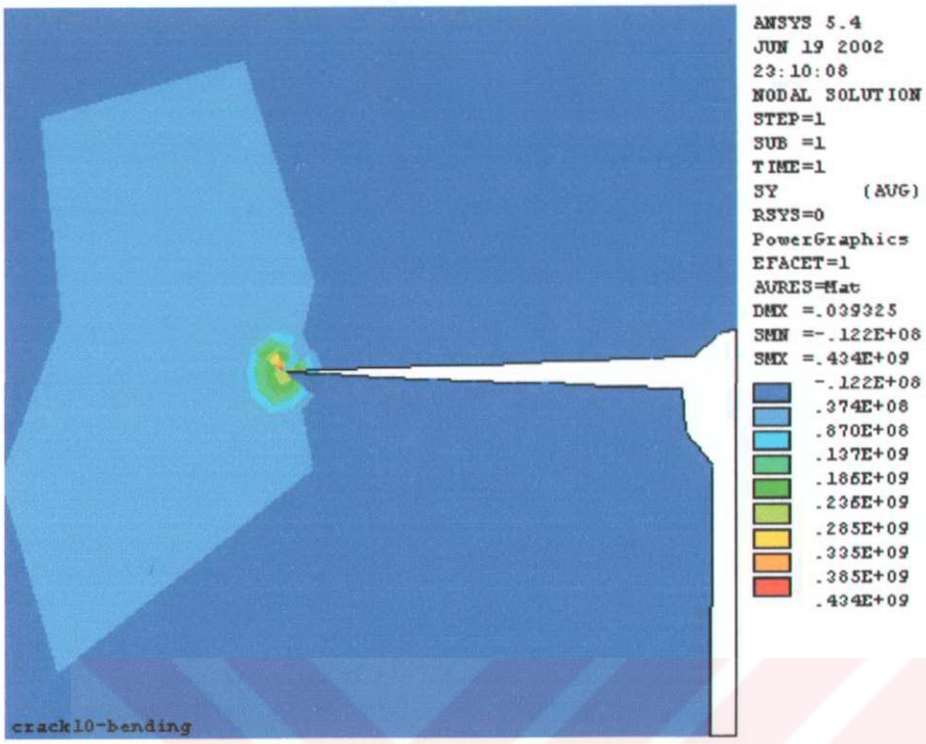

Figure C5 Stress distribution due to bending at the tip of crack of a = 10 mm.

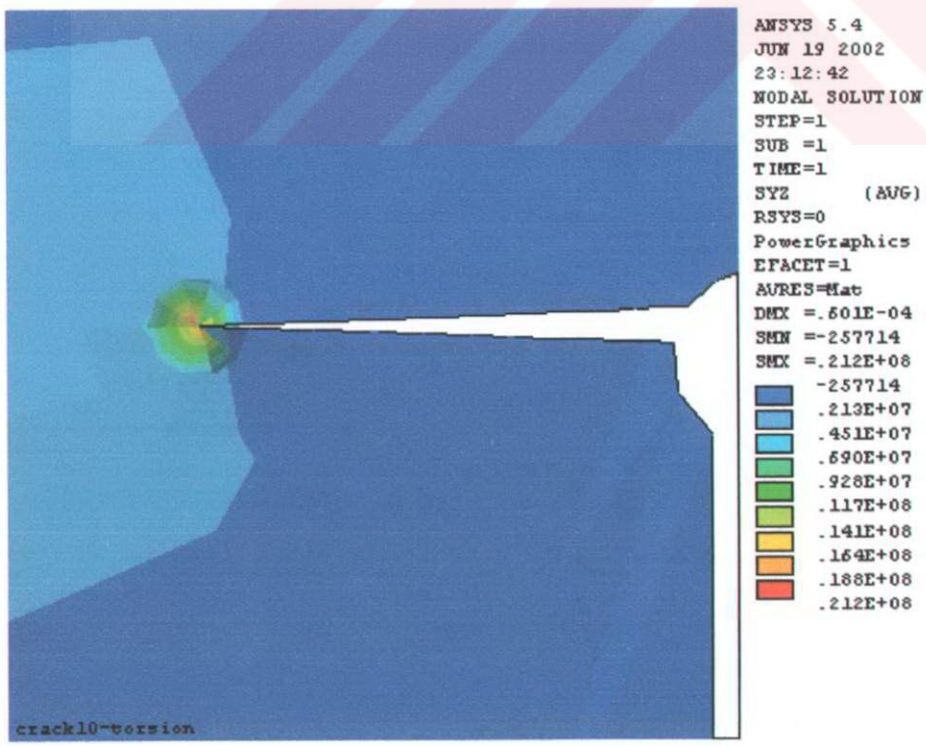

Figure C6 Stress distribution due to torsion at the tip of crack of a = 10 mm.

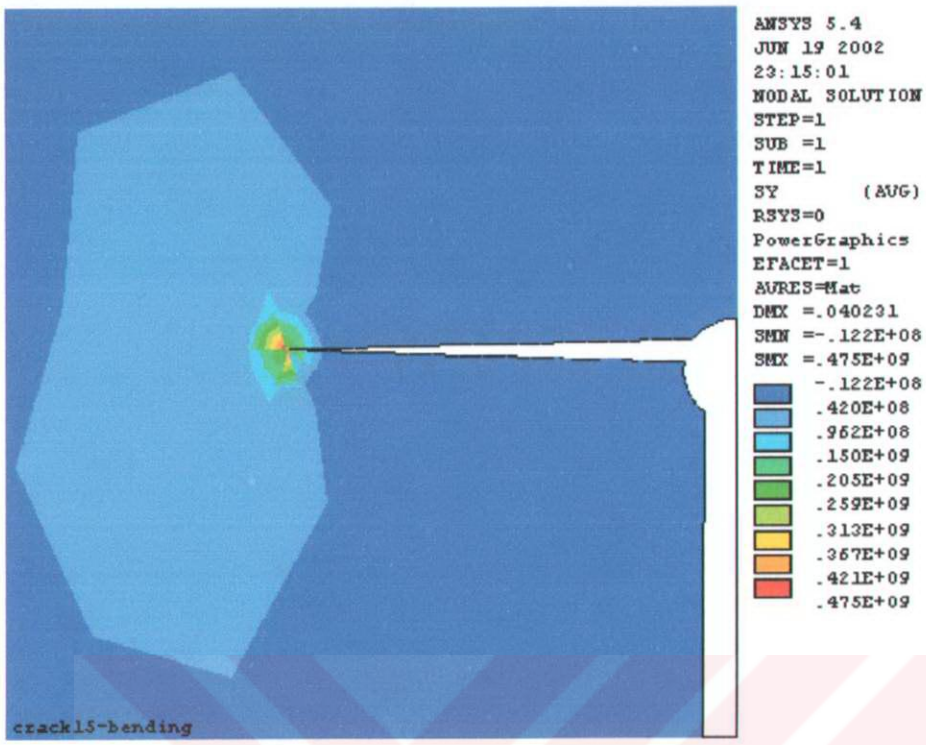

Figure C7 Stress distribution due to bending at the tip of crack of a = 15 mm.

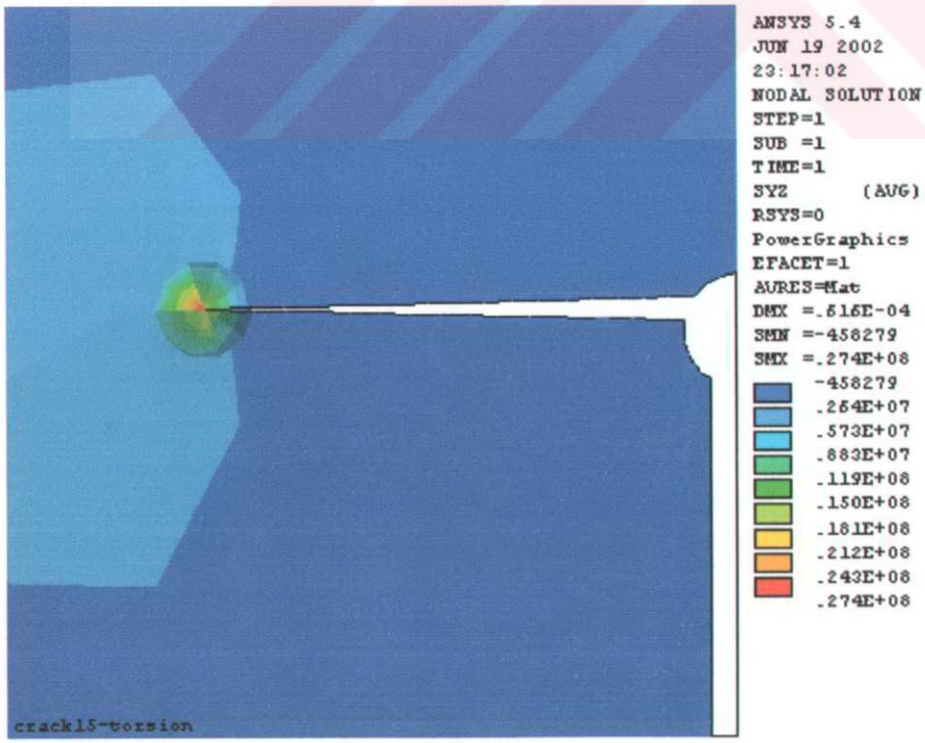

Figure C8 Stress distribution due to torsion at the tip of crack of a = 15 mm.

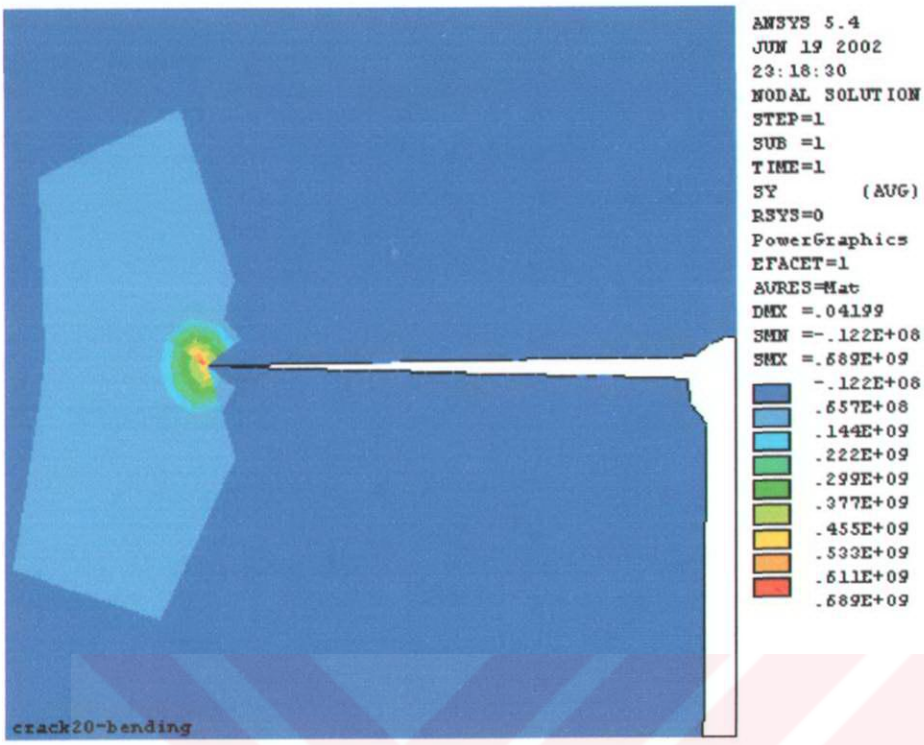

Figure C9 Stress distribution due to bending at the tip of crack of a = 20 mm.

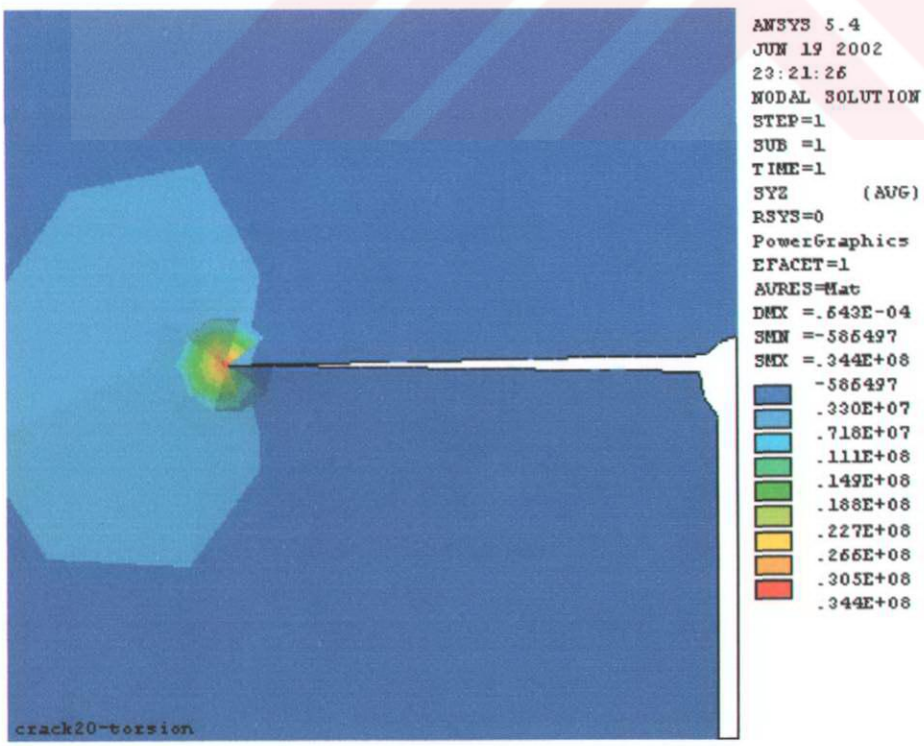

Figure C10 Stress distribution due to torsion at the tip of crack of a = 20 mm.

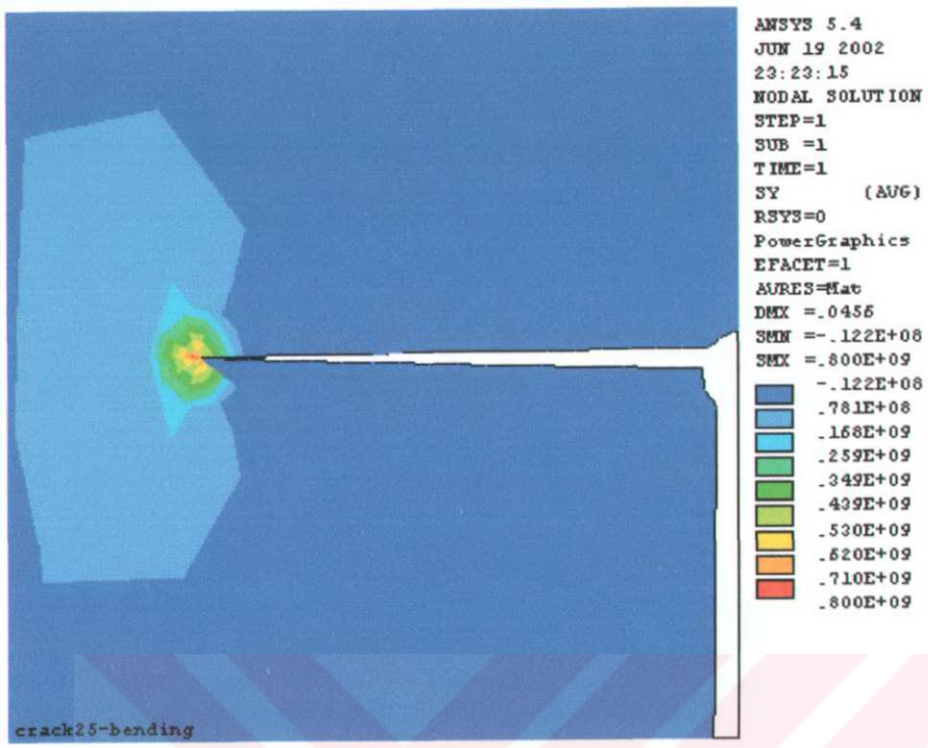

Figure C11 Stress distribution due to bending at the tip of crack of a = 25 mm.

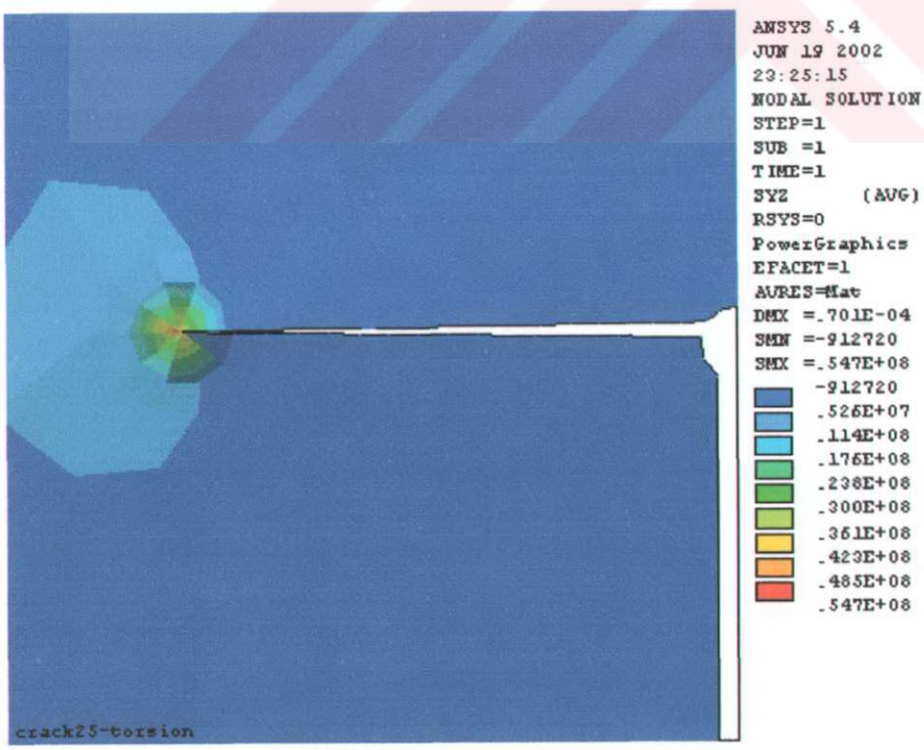

Figure C12 Stress distribution due to torsion at the tip of crack of a = 25 mm.

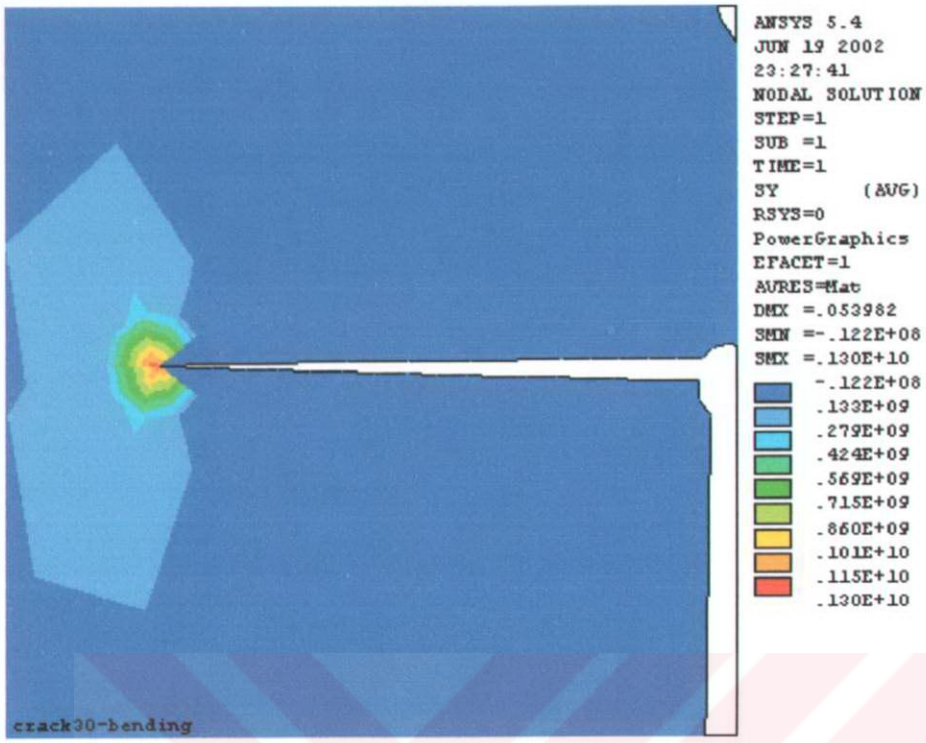

Figure C13 Stress distribution due to bending at the tip of crack of a = 30 mm.

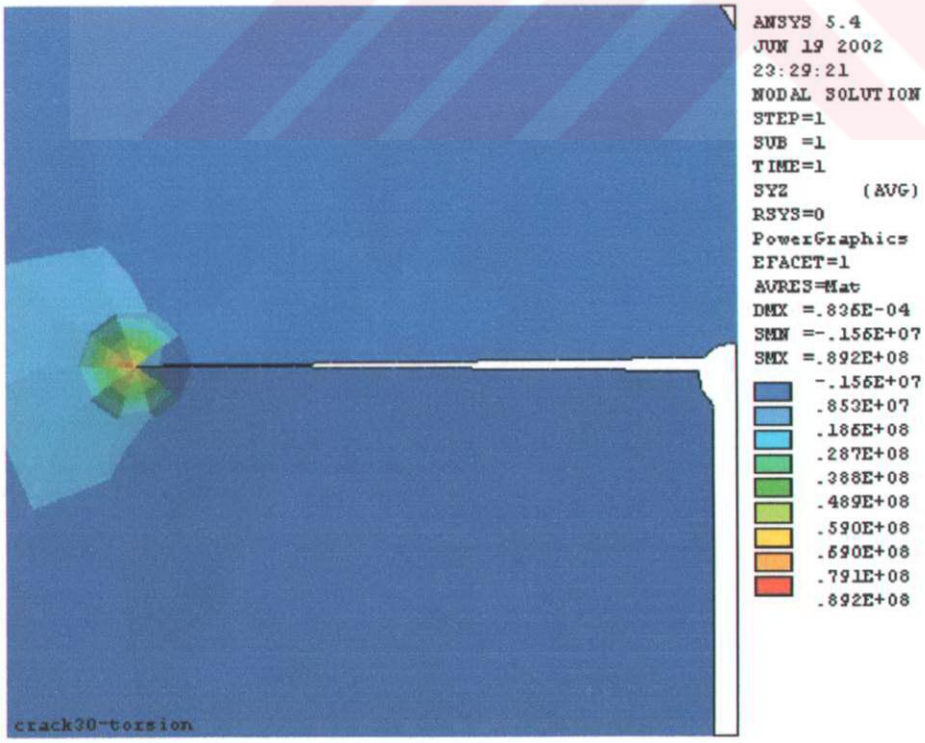

Figure C14 Stress distribution due to torsion at the tip of crack of a = 30 mm.

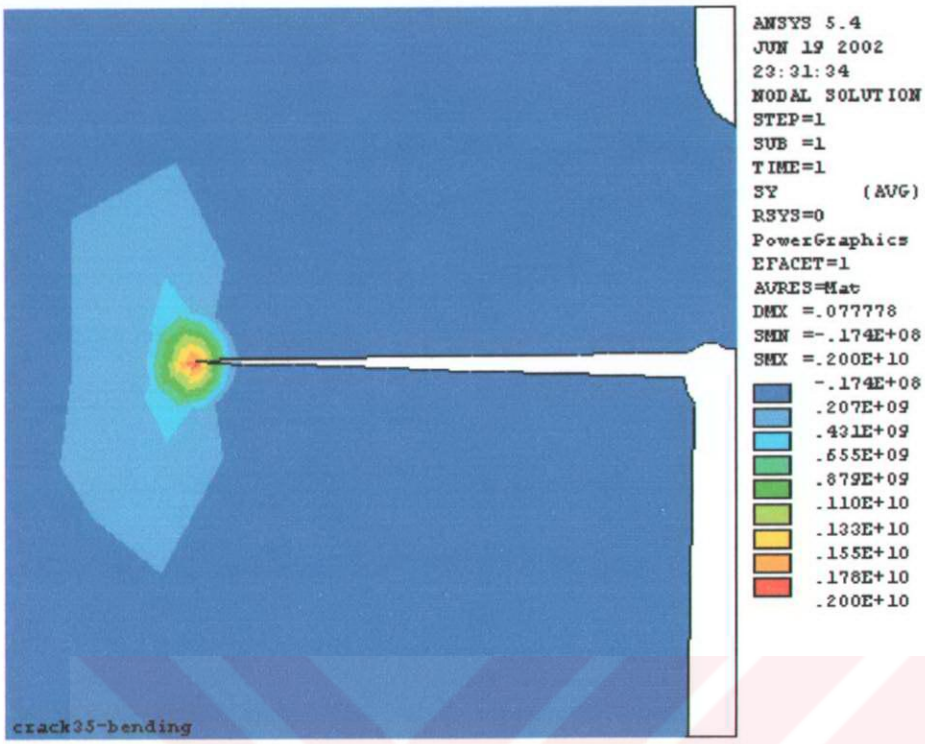

Figure C15 Stress distribution due to bending at the tip of crack of a = 35 mm.

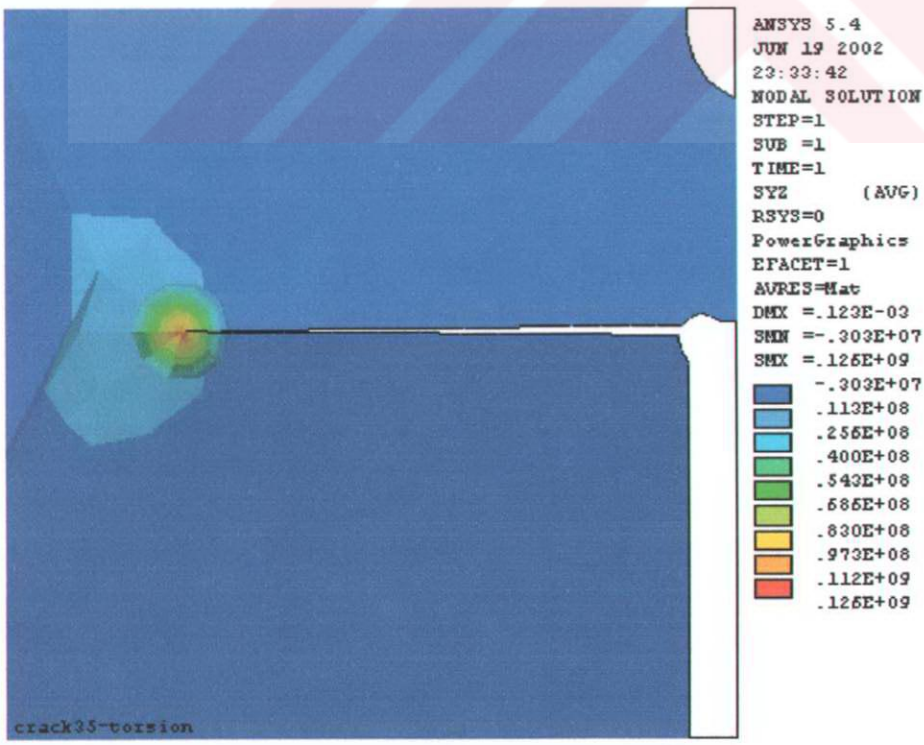

Figure C16 Stress distribution due to torsion at the tip of crack of a = 35 mm.

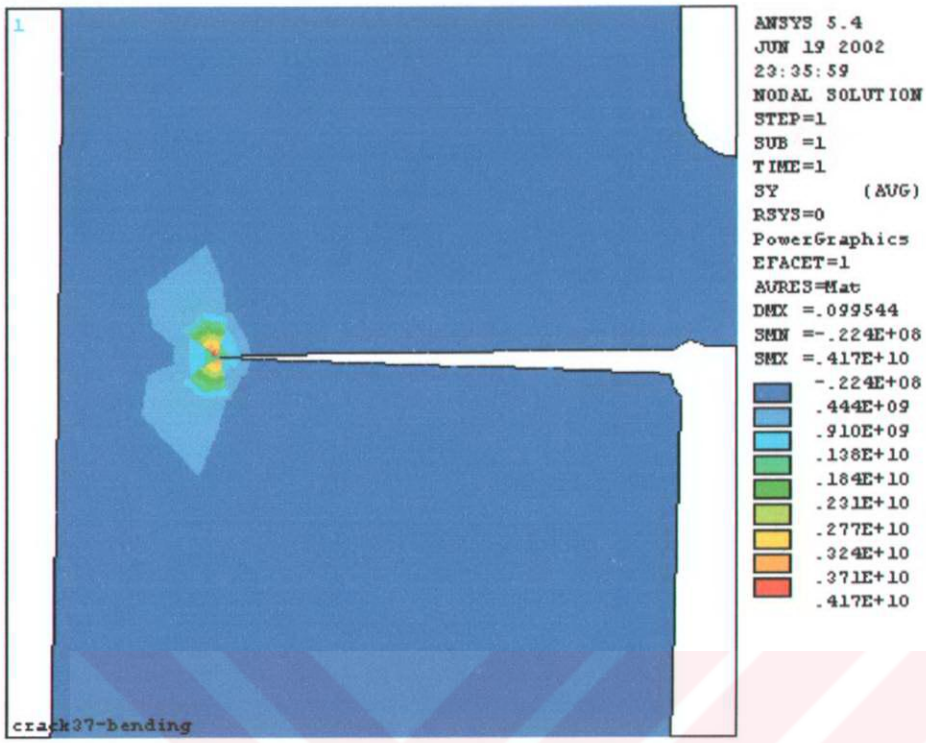

Figure C17 Stress distribution due to bending at the tip of crack of a = 37 mm.

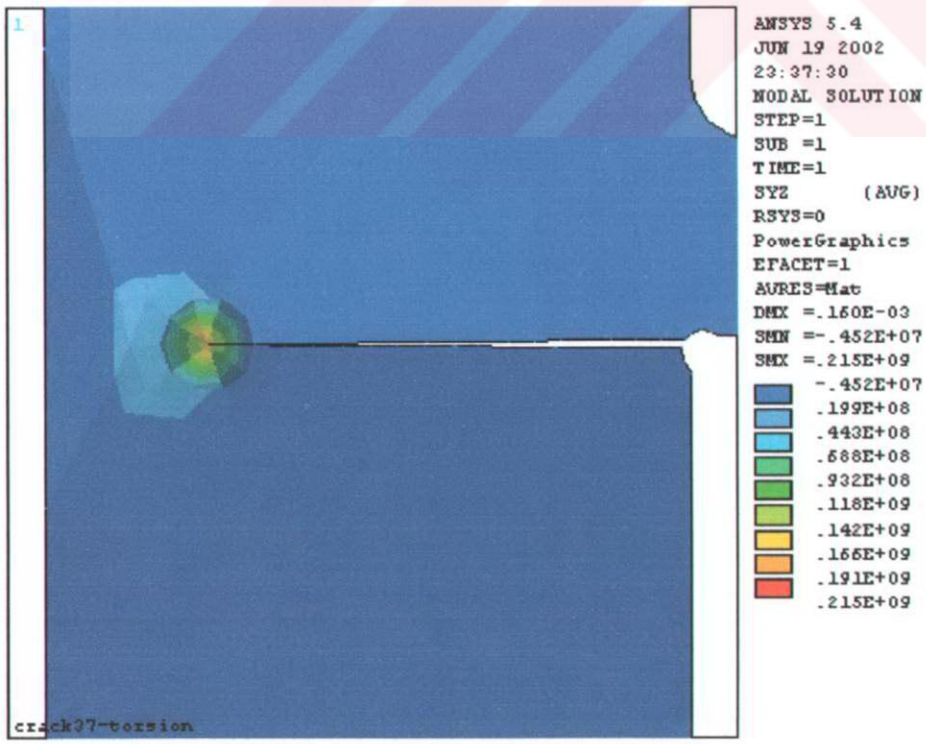

Figure C18 Stress distribution due to torsion at the tip of crack of a = 37 mm.

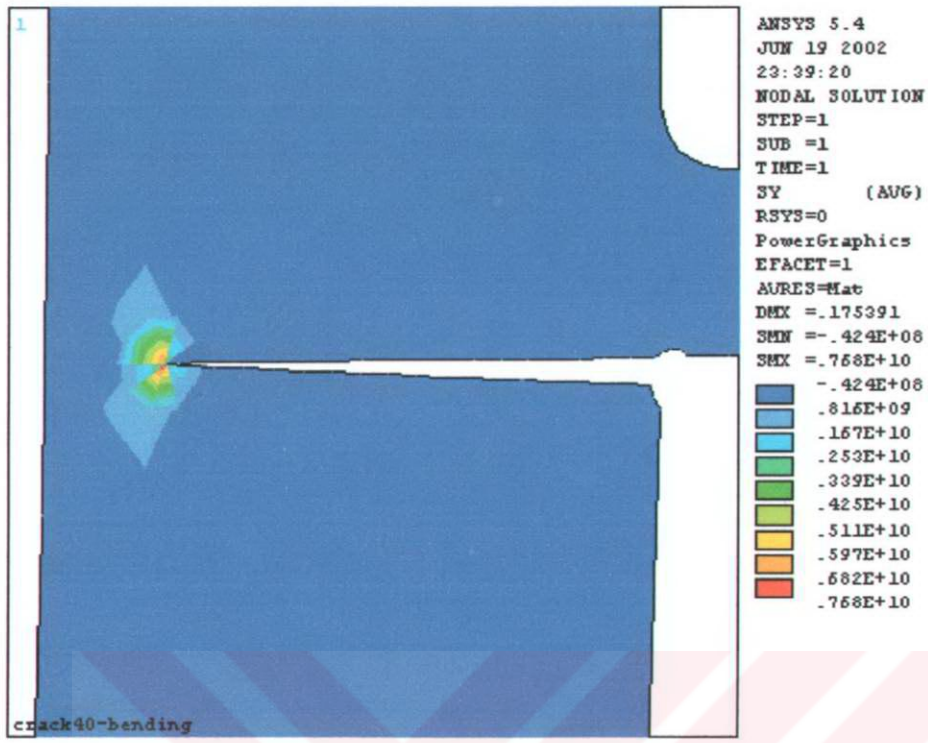

Figure C19 Stress distribution due to bending at the tip of crack of a = 40 mm.

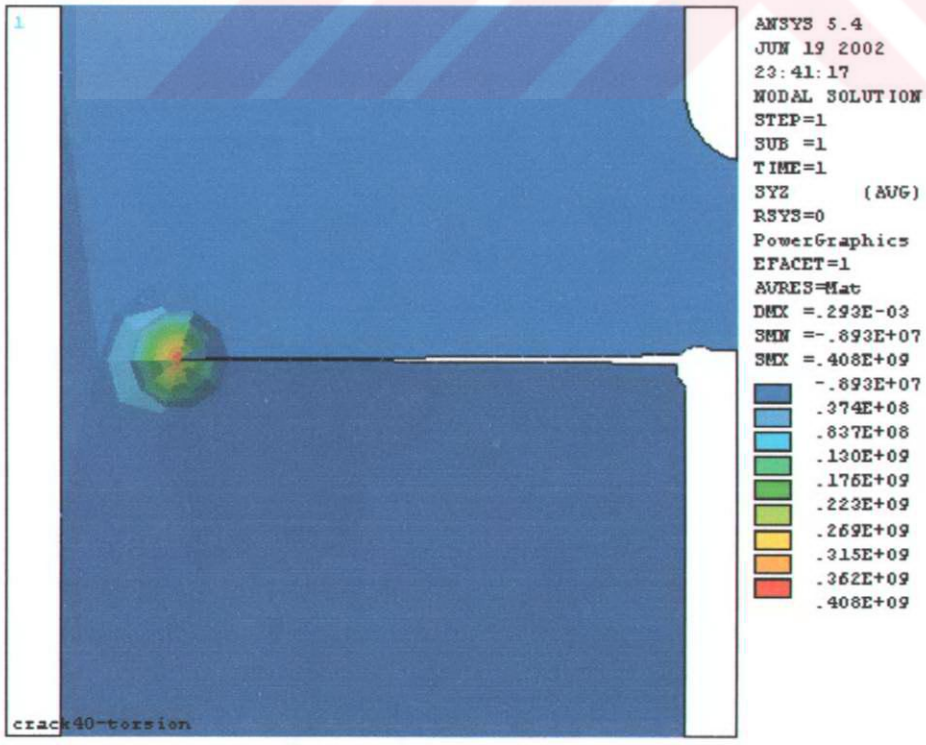

Figure C20 Stress distribution due to torsion at the tip of crack of a = 40 mm.

T.C. YÜKSEKÖĞRETİM KURULU
DOKÜMANTASYON MERKEZİ